universität wien

DISSERTATION

Titel der Dissertation

"Neutron capture measurements on ^{62}Ni, ^{63}Ni and ^{197}Au and their relevance for stellar nucleosynthesis"

Verfasserin

Mag. rer. nat. Claudia Lederer, Bakk. rer. nat.

angestrebter akademischer Grad

Doktorin der Naturwissenschaften (Dr. rer. nat.)

Wien, 2012

Studienkennzahl lt. Studienblatt:	A 091 411
Dissertationsgebiet lt. Studienblatt:	Physik
Betreuer:	Univ.-Prof. Dipl. Ing. Dr. Robin Golser

Abstract

Neutron capture reactions in stars are responsible for forming about 99% of the elemental abundances heavier than Fe. Two processes contribute about equally to the overall abundance pattern: the slow neutron capture process (*s* process) where neutron densities are small and therefore radioactive decay is generally faster than subsequent neutron capture on radionuclides, and the rapid neutron capture process (*r* process) which takes place in environments of high neutron densities, driving the reaction path towards the neutron rich side. The key nuclear physics input for *s* process studies are stellar neutron capture cross sections, called MACS (Maxwellian-averaged cross section). In the course of this work, different reactions relevant to *s* process nucleosynthesis have been studied. To improve and check existing information, neutron capture cross sections of most stable Fe and Ni isotopes were measured via the time-of-flight technique at the n_TOF facility at CERN. This campaign was triggered by a work of Sneden *et al.* (Ap. J. 533 (2000) L139-L142), who found that observed abundances in Ultra Metal Poor stars do not agree with calculated values, using existing experimental (n,γ) cross sections as input. First results on the cross section of ^{62}Ni(n,γ) are presented in this work. Of special interest for studying stellar conditions in *s* process environments are branching points, i.e. where half lives are long enough so that neutron capture competes with radioactive decay. ^{63}Ni with a half life of 101.1 years represents such a branching and its (n,γ) cross section has a crucial influence on the production of Cu. The ^{63}Ni(n,γ) reaction, of which no cross section data are available above thermal neutron energies, was measured at n_TOF and first results are reported here.
For (n,γ) reaction measurements, accurate normalization standards play an important role. Two experiments were performed to resolve a discrepancy of the ^{197}Au(n,γ) cross section in the lower keV region between the reference cross section used for MACS measurements (Ratynski and Käppeler, Phys. Rev. C 37 (1988) 595-604) and the ENDF/B-VII.1 evaluation. The ^{197}Au(n,γ) cross section, measured at n_TOF, has been determined from 5 to 400 keV neutron energy. The results are in agreement with the ENDF/B-VII.1 evaluation. The MACS at $k_BT = 30$ keV is in very good agreement with the MACS calculated from the ENDF evaluation. Within quoted uncertainties it is compatible with the MACS result of Ratynski and Käppeler which was obtained by the activation technique. We re-measured the neutron spectrum produced by the ^{7}Li$(p,n)^{7}$Be reaction (that was used for activation measurements) with improved resolution and accuracy at Physikalisch-Technische-Bundesanstalt Braunschweig. The results confirm the spectrum measured by Ratynski and Käppeler. The ^{197}Au(n,γ) cross section averaged over the neutron spectrum obtained in this work agrees with the result using the Ratynski and Käppeler spectrum, providing increased confidence in the use of this reaction as a standard.

Zusammenfassung

Etwa 99% der Häufigkeiten von schwereren Elementen als Fe werden durch Neutroneneinfangreaktionen in Sternen erzeugt. Zwei Prozesse tragen zu gleichen Teilen bei: der langsame Neutroneneinfangprozess (*s* Prozess), der durch niedrige Neutronendichten charakterisiert ist, weswegen radioaktiver Zerfall eines erzeugten Radionuklids im Allgemeinen schneller stattfindet als ein darauf folgender Neutroneneinfang, und der schnelle Neutroneneinfangprozess (*r* Prozess), der in Umgebungen hoher Neutronendichten stattfindet und daher den Reaktionspfad zu neutronenreichen Kernen hin verlagert. Neutroneneinfangquerschnitte unter stellaren Bedingungen, kurz MACS (Maxwellian-averaged cross section), stellen eine der wichtigsten Eingangsgrößen zur Untersuchung von *s* Prozess Modellen dar. Verschiedene für den *s* Prozess relevante Kernreaktionen wurden im Zuge dieser Arbeit untersucht. Die (n,γ)-Wirkungsquerschnitte fast aller stabilen Isotope von Fe und Ni wurden mit der Flugzeitmethode an der n_TOF (neutron time-of-flight) Anlage am CERN gemessen. Der Grund für diese Kampagne waren Beobachtungen von Sneden *et al.* (Ap. J. 533 (2000) L139-L142), die Diskrepanzen zwischen beobachteten und berechneten Elementhäufigkeiten in ultra-metallarmen Sternen zum Vorschein brachten, wobei (n,γ)-Wirkungsquerschnitte als Input für diese Berechnungen dienten. Über erste Resultate für den Wirkungsquerschnitt von ^{62}Ni(n,γ) wird in dieser Arbeit berichtet. Verzweigungspunkte im *s* Prozess, also langlebige Radioisotope, deren Zerfall mit Neutroneneinfang konkurriert, sind von speziellem Interesse, da sie das Studium physikalischer Bedingungen in *s* Prozess Umgebungen erlauben. Ein Beispiel für eine *s* Verzweigung ist ^{63}Ni mit einer Halbwertszeit von 101.1 Jahren, dessen Wirkungsquerschnitt einen hohen Einfluss auf die Entstehung von Cu im *s* Prozess hat. Der ^{63}Ni(n,γ) Querschnitt wurde bei n_TOF gemessen und erste Resultate werden in dieser Arbeit präsentiert.
Für die Messung von (n,γ) Querschnitten spielen Standards zur Normierung der Daten eine wichtige Rolle. Es wurden zwei Experimente durchgeführt, um eine Diskrepanz von ^{197}Au(n,γ) zwischen dem Referenzwirkungsquerschnitt für die Messung von MACSs (Ratynski und Käppeler, Phys. Rev. C 37 (1988) 595-604) einerseits, und der ENDF/B-VII.1 Evaluation andererseits, zu klären. Der ^{197}Au(n,γ) Wirkungsquerschnitt wurde bei n_TOF gemessen und für Neutronenenergien zwischen 5 keV und 400 keV bestimmt. Die Resultate stimmen mit der ENDF-Evaluation über den gesamten Energiebereich überein. Der MACS bei $k_BT = 30$ keV ist in sehr guter Übereinstimmung mit ENDF. Innerhalb der Unsicherheiten ist das Resultat mit dem MACS von Ratynski und Käppeler kompatibel, der mit der Aktivierungsmethode bestimmt wurde. Das Neutronenspektrum der ^{7}Li$(p,n)^{7}$Be Reaktion (das für die Aktivierungsmessungsmessungen verwendet wurde), wurde mit verbesserter Auflösung und Genauigkeit gemessen. Die Resultate in dieser Arbeit bestätigen die Messung von Ratynski und Käppeler. Der über das gemessene Neutronenspektrum gemittelte ^{197}Au(n,γ) Querschnitt stimmt mit dem Wert unter Verwendung des Spektrums von Ratynski und Käppeler überein. Dieses Ergebnis bestätigt die Verwendung der ^{197}Au(n,γ) Reaktion als Normierungsstandard.

Contents

Outline and Statement of Authorship

The neutron capture cross sections of the reactions ^{62}Ni(n,γ), ^{63}Ni(n,γ) and ^{197}Au(n,γ) have been measured over a wide energy range via the time-of-flight technique at the n_TOF facility located at CERN. Since ^{197}Au(n,γ) serves also as a reference for measuring stellar cross sections via activation, the neutron spectrum of the reaction ^{7}Li$(p,n)^{7}$Be which is used as neutron source in such experiments has been measured at Physikalisch Technische Bundesanstalt Braunschweig (PTB).
Chapter 1 gives an introduction about stellar evolution and nucleosynthesis processes in general. A large part of this chapter is dedicated to the slow neutron capture process (*s* process).
Chapter 2 addresses the theoretical background of neutron capture reactions.
Chapter 3 describes the time-of-flight technique and basic properties of the n_TOF facility. In that context I describe how to derive (n,γ) cross sections from time-of-flight data.
Chapter 4 deals with the neutron capture cross section measurement of ^{62}Ni and ^{63}Ni. The data analysis and first results are described.
Chapter 5 presents the cross section measurement of ^{197}Au(n,γ). This chapter consists to a great extent of the article "^{197}Au(n,γ) cross section in the unresolved resonance region" [I1]. As indicated by first-authorship, the majority of work in [I1] has been done by C. Lederer. The simulations of the γ-attenuation factor, of the γ-background scaling factor (both in Sec. 5.3.3), of the correction due to inhomogeneous γ emission in the saturated resonance (in Sec. 5.3.4), as well as the simulation of Au resonances and calculations of the Au cross section using the simulated data (Sec. 5.4.2) were done by co-authors of this paper. The respective parts are indicated additionally by footnotes in the text.
Chapter 6 describes the measurement of the neutron spectral distribution generated from the ^{7}Li$(p,n)^{7}$Be reaction. This chapter is reproduced from the article "Definition of a standard neutron field with the ^{7}Li$(p,n)^{7}$Be reaction", submitted to Phys. Rev. C (30 January 2012) [I2]. Except for the simulation of the detector efficiency (in Sec. 6.3) and the calculation of the angular neutron spectra with the code n17 (in Sec. 6.4) the majority of work was done by C. Lederer. The respective parts are indicated additionally by footnotes in the text.

1 Formation of elements in our universe

1.1 Introduction

The first experimental evidence that nucleosynthesis is still ongoing in our universe, was found by Merrill in 1952 [1], who observed spectroscopic lines of unstable Tc in stellar spectra of Red Giants (the longest lived Tc isotope has a half life of $t_{1/2} = 4 \times 10^6$ y, much shorter than the evolution time of a star). Only 5 years later, Burbidge, Burbidge, Fowler and Hoyle published a review proposing 8 nuclear processes responsible for forming all known elements [2]. This work laid the foundation for subsequent nucleosynthesis studies and the majority of ideas therein are still in use today.

Besides all isotopes of H, He and to a minor extent Li which were already formed during the first minutes after the Big Bang, all elements in our universe are synthesized in the interior of stars. An exception are the lightly bound nuclei Li, Be and B which are predominantly produced by spallation reactions of cosmic rays since they are easily destroyed in the hot stellar interiors.
Figure 1.1 shows the abundances of elements up to Pb in our solar system as a function of atomic number Z. They vary over many orders of magnitude, where H is by far most abundant with a 70.7% mass fraction, followed by He with 27.4%. All the other elements, in the astronomical nomenclature called ”metals”, account for about 1.9% [3, 4]. Since elements are synthesized by nuclear reactions, their abundances also reflect nuclear properties: in general even-even nuclei are more abundant than nuclei with odd neutron and/or proton numbers, magic shell configurations such as ^{16}O and ^{40}Ca are also enhanced. This holds especially for elements around the Fe region, where the binding energy per nucleon is highest. Accordingly, the lightly bound Li, Be and B are very rare. To understand the different nucleosynthesis processes in stars better, the next section will summarize what is known today about the life of stars of different masses. Subsequently, the nucleosynthesis processes will be described with a focus on the slow neutron capture process, which is the motivation of this work.

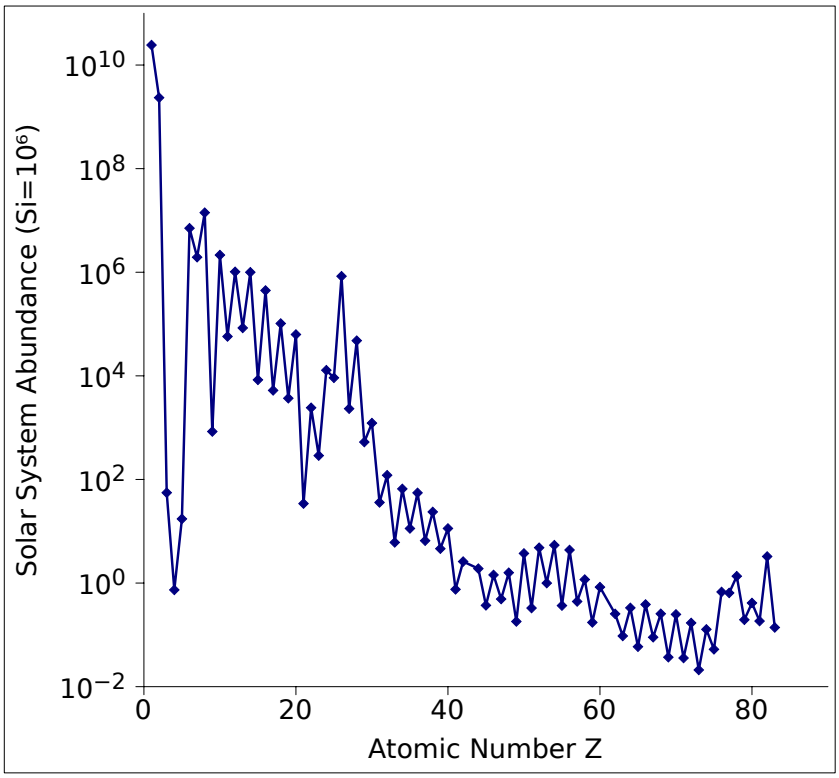

Figure 1.1: Solar system abundances for different elements. Data are from K. Lodders [4].

1.2 Stellar evolution

In order to maintain stability, a star needs to balance gravitational pressure by providing the same amount of thermal pressure ("hydrostatic equilibrium"). Since stars radiate away energy, they account for this energy loss either through contraction, where half of the gained gravitational energy is transformed into thermal energy (Virial theorem), or through nuclear fusion reactions. Fusion is only efficient at certain plasma temperatures, thus, as a first step, the star needs to contract and heat until the temperature is high enough to ignite the first fusion reaction. If this fuel is used up, the star contracts again until the next possible fusion reaction ignites, and so on. Generally, burning stages proceed via reactions with the lowest Coulomb barrier. A star spends a dominant part of its life burning hydrogen, which releases most energy per unit mass and is most abundant. Hence, to maintain stability successive burning stages having decreasing energy gain per mass proceed more rapidly to achieve a constant energy generation rate, e.g. a 25 $M_\odot$ star burns around 10^7 years hydrogen, but silicon, which is the last burning stage before the star collapses, lasts only 1 day. How a star evolves depends on its initial mass. In the following, a short summary will be given, focusing on stars relevant for *s* process nucleosynthesis, which will be described in detail in Section 1.4.1. More in-

formation on stellar evolution can be found for example in References [5, 6].
All stars with > 0.4 solar masses ($M_\odot$) start hydrogen burning in the core. After the hydrogen fuel is exhausted, burning continues in the shell, while the core contracts and becomes increasingly dense. The surface expands and cools, making it appear redder, accompanied by increasing luminosity. The star becomes a Red Giant. At a temperature of 0.1 GK (1 GK= 10^9 K) He burning ignites in the core.
Stars of intermediate masses, between 0.4 $M_\odot$ and 8 $M_\odot$ continue He burning in the shell when the core He fuel is consumed. He shell and H shell burning alternate as the main contributor to the nuclear energy generation due to thermal instabilities: He burning continues on the bottom of a He shell around the core consisting of the He burning ashes C and O, while H burning in a shell on the bottom of a H convective envelope adds more and more burning ashes (He) to the He shell. This triggers a thermal pulse in the He burning zone, which expands outwards. As a result, the H shell is pushed out and ceases to burn. For some hundreds of years He burning is the only source of nuclear energy. Eventually, He burning ceases in the outer parts and the star contracts. The H burning shell ignites again and burns for about 5×10^4 years until the next pulse occurs. Thermal pulses repeat several times in the life of a star and the radius may vary by a factor as large as 4. A significant amount of mass is lost through stellar winds and material of different shells is mixed, since the convective envelope reaches below the H-shell and brings burning products like He and C to the stellar surface. This phase is called TP-AGB phase, where TP refers to ”thermal pulse” and AGB to the evolutionary stage of the star on the asymptotic giant branch in the Hertzsprung Russel diagram [7]. During this phase the slow neutron capture process (see Section 1.4.1) takes place. When the thermal pulses stop, the star has only a fraction of its initial mass left. Outer hydrogen rich material is ejected into the Interstellar Medium (Planetary Nebula), the star becomes a White Dwarf, stabilized by its degenerate core and cools slowly.
For more massive stars, carbon core burning ignites and if the mass exceeds around 11 $M_\odot$ this is followed by neon, oxygen and silicon burning. After carbon burning, the further burning stages happen so fast, that the star cannot adjust to structural changes. The star ends up with an onion like structure and an Fe core, having high luminosity and high mass loss. The core is degenerate and the outer shell adds ashes to it. If the mass of the core exceeds the Chandasekhar limit (approx. 1.4 $M_\odot$), it collapses in free fall until the core reaches nuclear densities (10^{14} g/cm^3). This causes the mass inflow to rebound, creating an outward supernova shock wave which compresses and heats the overlying material. During this time explosive burning is believed to happen (e.g. the *r* process, described in Section 1.4.2). The remaining star ends up as neutron star or black hole.

1.3 Nuclear burning stages

1.3.1 H burning

For stars with primordial elemental abundances, hydrogen burning entirely takes place via the pp chains. There are 3 different pp chains (called ppI, ppII and ppIII) with different energy generation rates depending on the stellar temperature. All of them create one ^{4}He out of 4 protons, ppII and ppIII use ^{4}He as a catalyst. The only possible reaction channel of two protons, not producing an unstable nucleus is the fusion of two hydrogen nuclei to a deuteron: $p + p \rightarrow d + e^+ + \nu$. This reaction proceeds via the weak nuclear force, has therefore a very low cross section and determines the duration of the H burning stage. The deuteron is almost instantly destroyed by capturing another proton via the reaction $d + p \rightarrow^3$ He + γ. The following consumption of ^{3}He via ^{3}He +^{3} He $\rightarrow^4$ He + $2p$ closes the ppI chain.
If already heavier nuclides are present, hydrogen can also be burnt via the CNO-cycle (also called after their discoverers the "Bethe-Weizsäcker cycle"), where carbon, nitrogen and oxygen act as catalysts for fusion of 4 protons to ^{4}He. It is characterized by (p, γ) reactions competing with the (p, α) channel and its energy generation rate "ϵ" shows a strong temperature dependence of $\epsilon \propto T^{15}$ (for the pp chain $\epsilon \propto T^4$).

1.3.2 He burning

He burning in stars takes place through the triple-α process and becomes efficient at temperatures around 0.2 GK, producing ^{12}C out of 3 α particles. The reaction ^{4}He+^{4}He$\leftrightarrow^8$Be is in equilibrium, providing a small amount of ^{8}Be. In 1952, Fred Hoyle explained the high abundance of ^{12}C in the universe by predicting a resonance of the reaction ^{8}Be$(\alpha, \gamma)^{12}$C in the energy region corresponding to the α energies in the stellar plasma [8]. This resonance with E_R = 287.6 keV was discovered a few years later by Cook *et al.* [9]. The triple α process shows a very strong temperature dependence of $\epsilon \propto T^{41}$. Apart from ^{12}C, also ^{16}O and to a small extent ^{20}Ne are produced by α captures.

1.3.3 Advanced burning stages

The ashes of He burning consist mainly of ^{12}C and ^{16}O. The core contracts until it reaches temperatures between 0.6 and 1 GK and the fusion of ^{12}C+^{12}C ignites, comprising mainly the reactions ^{12}C(^{12}C, p)^{23}Na, ^{12}C(^{12}C, α)^{20}Ne and ^{12}C(^{12}C, n)^{23}Mg. Carbon burning is followed by neon and oxygen burning. The last burning stage is silicon burning at around 3.5 GK. The most abundant nuclei ^{28}Si and ^{30}Si undergo photodisintegration reactions, which proceed to ^{24}Mg. The protons, α-particles and neutrons produced in this way cause secondary reactions resulting in a reaction flow up to the

Fe/Ni mass region. Abundances are rearranged according to the highest nuclear stability, generating the pronounced abundance peak in the Fe/Ni region, where the binding energy per nucleon is highest (around $Z = 26$ in Figure 1.1). This phase is called "nuclear statistical equilibrium".

1.4 Nucleosynthesis above Fe

Elements with $A > 56$ are dominantly produced via neutron capture processes, since charged particle reactions are suppressed due to the increasing Coulomb barriers. Two distinct neutron capture processes with different characteristics can explain ≈99% of the elemental abundances heavier than Fe, the slow neutron capture process (*s* process) and the rapid neutron capture process (*r* process). The *s* process is characterized by reaction rates slower than radioactive decay, which means neutron capture to an unstable nucleus is followed by β-decay rather than by a subsequent neutron capture. Hence, the production path takes place close to the stability valley on the nuclear chart. In contrast, the *r* process takes place in explosive environments of high neutron densities. The reaction path is driven towards the neutron drip line since β-decays are much slower than neutron captures. Figure 1.2 illustrates schematically the reaction path of these two processes. In the top left corner the abundance distribution as a function of mass number is shown. Abundances above Fe show several peaks, which can be assigned to those different neutron capture processes. The pronounced peaks, indicated with "s" are due to bottlenecks in the *s* process, where magic neutron shell configurations are reached and thus, the capture cross sections are small. The broader peaks at lower masses are produced by *r* process nucleosynthesis. They correspond to magic shell configurations on the neutron rich side, which are "waiting points" in the *r* process and populated via subsequent β-decays to the valley of stability. Proton rich nuclides, which are bypassed by the *s* and *r* process, are produced by photo-disintegration reactions in the *p* process and are on average a factor of 100 less abundant than *s* and *r* nuclides. In the following sections, the different process will be described in more detail.

1.4.1 s process

Classical s process model

The *s* process starts in the Fe peak region, where ^{56}Fe, and to a lesser extent ^{54}Fe and ^{58}Ni, act as seed nuclei. β-decays are assumed to proceed much faster than neutron captures, therefore they do not affect the reaction flow from mass A to $A + 1$. Neutrons are rapidly thermalized inside a star, thus their velocities follow a Maxwell-Boltzmann distribution with the most probable energy $E_n = k_B T$, where k_B is the Boltzmann constant and T is the temperature (see Section 2.4). For constant temperature T, the production

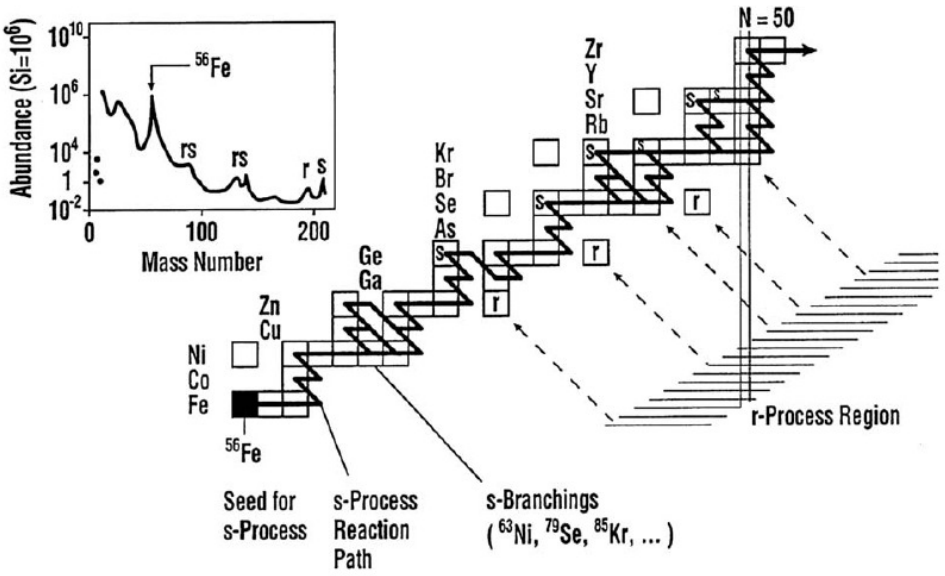

Figure 1.2: Illustration of nucleosynthesis processes for heavy elements on the chart of nuclides. The *s* process proceeds along the valley of stability, while the *r* process happens close to the neutron drip line. Picture is taken from Reference [10].

and destruction of a nuclide with mass A via neutron capture can be described as

$$\frac{dN(A)}{dt} = N_n(t)v_T[N(A-1) < \sigma >_{A-1} - N(A) < \sigma >_A] \tag{1.1}$$

where N is the number density of the respective s nuclide, $N_n(t)$ the time dependent neutron density and v_T the most probable velocity in a Maxwell-Boltzmann distribution. $< \sigma >$ is called Maxwellian-averaged cross section (MACS) and is the reaction rate averaged over the stellar neutron spectrum divided by v_T ($< \sigma >$ and v_T are defined in Section 2.4). The first term accounts for the production of the nuclide with mass A via neutron capture, the second term for its destruction. For equilibrium with $\frac{dN(A)}{dt} = 0$ one finds immediately $\sigma N = \text{const.}$, which means that the abundance of a nuclide only depends on its capture cross section. This relation is called local equilibrium approximation since it is valid for certain abundance ranges for s only isotopes as will be outlined later. For a more general solution of equation 1.1 one can define a neutron exposure τ as

$$\tau = v_T \int N_n(t)dt \tag{1.2}$$

with the dimension of an inverse area (mb^{-1}). It was found that experimental abundance data could be best reproduced by assuming an exponentially decreasing probability

distribution of neutron exposures [11, 12] of the form

$$p(\tau) = \frac{fN_s^{\text{seed}}(56)}{\tau_0} \exp(-\tau/\tau_0) \quad \text{with} \quad \int_0^\infty p(\tau)d\tau = fN_s^{\text{seed}}(56) \tag{1.3}$$

where τ_0 is the mean neutron exposure and $fN_s^{\text{seed}}(56)$ is the fraction of ^{56}Fe seed nuclei that experienced exposure. The solution of equation 1.1 is then

$$< \sigma >_A \overline{N(A, \tau_0)} = \frac{fN_s^{\text{seed}}(56)}{\tau_0} \prod_{i=56}^{A} \frac{1}{1 + 1/(\tau_0 < \sigma >_i)} \tag{1.4}$$

and for adjacent mass numbers

$$< \sigma >_A \overline{N(A, \tau_0)} = \frac{< \sigma >_{A-1} \overline{N(A-1, \tau_0)}}{1 + 1/(\tau_0 < \sigma >_A)} \tag{1.5}$$

where $\overline{N(A, \tau_0)}$ is the final abundance. More information can be found in [5, 13].
For large cross sections $< \sigma >_A$ and sufficiently large neutron exposures the denominator becomes unity, corresponding to the local equilibrium approximation. Plotting experimental values for $< \sigma > \overline{N}$ for nuclides which are dominantly or only produced in the *s* process as in Figure 1.3, one sees that this approximation is valid for $90 < A < 205$ between neutron shell closures. At magic neutron numbers the capture cross section becomes very small and a step is introduced in the curve, e.g. around $A \approx 90$ with $N = 50$ and $A \approx 140$ with $N = 82$. Looking at elemental abundances, those steps correspond to the pronounced peaks indicated in the upper left corner of Figure 1.2. The component responsible for the abundances between $90 < A < 205$ is called the main component. For masses $A < 90$ the local equilibrium approximation is not valid and the abundance pattern can be described by introducing a weak *s* process component. By fitting the experimental $< \sigma > \overline{N}$ curve with equation 1.4 one can extract τ_0 and the fraction f of the Fe seed nuclei which undergo neutron exposure. This model, which is called "classical *s* process model" describes very well experimental data, except for the Pb/Bi mass region. A strong component has been suggested to resolve these discrepancies [14].

Branching points

As written in the beginning of this chapter, the concept of the *s* process is, that as soon as a radioactive nuclide is produced, it decays before a subsequent neutron is captured. For long half lives however, this is not the case and the *s* process path reaches a branching point, where one fraction of the radioactive nuclide undergoes radioactive decay and the other fraction undergoes neutron capture. The fraction of nuclei that decays can be

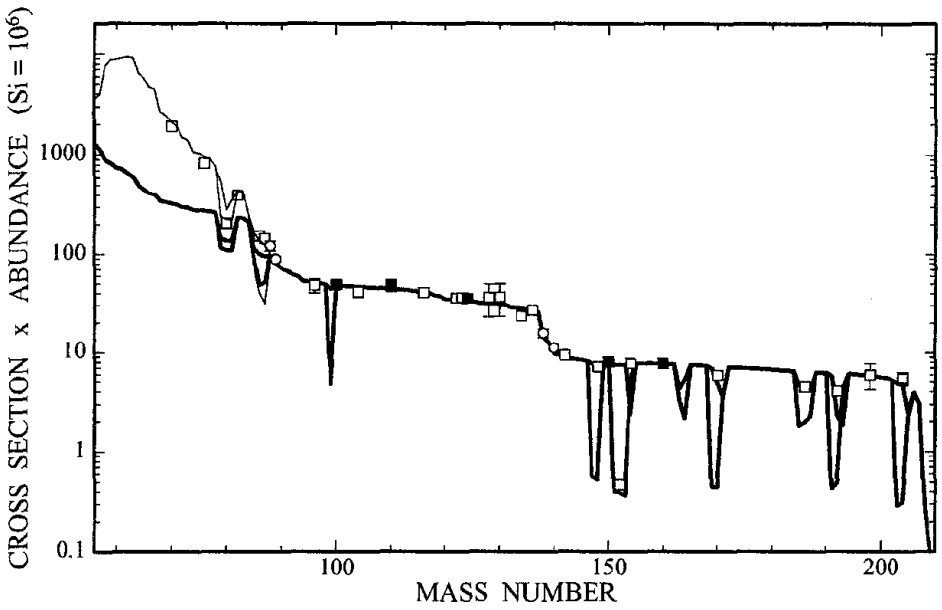

Figure 1.3: Values of $< \sigma > \overline{N}$ for *s* only isotopes as a function of mass number *A*. Experimental data (points) are fitted to the classical *s* process model approach (lines). Squares represent *s* only nuclides, circles represent nuclides with a very small *r* and *p* contribution. The solid squares have a very well known abundance and can be used for normalizing the curve. The thick line represents the contribution of the main component, the thin the sum of main and weak component. The picture is taken from Ref. [15].

described using the branching ratio

$$f_{\mathrm{B}} = \frac{\lambda_\beta(A)}{\lambda_\beta(A) + \lambda_{n\gamma}(A)} \tag{1.6}$$

where $\lambda_\beta(A)$ is the decay constant $\ln(2)/t_{1/2}$ and $\lambda_{n\gamma}(A) = N_n < \sigma >_A v_T$ is the reaction rate for neutron capture. Analysis of branchings provides crucial information about physical conditions in *s* process environments, like neutron density N_n, temperature T, and density ρ.

Stellar sites

While the classical *s* process represents a purely phenomenological approach, the development of stellar models provides an increasingly realistic picture of the *s* process at various sites. The basic features are summarized in Table 1.1.

- **Main component**
  The main *s* process takes place in thermally pulsing AGB stars with masses of

1.5 $M_\odot < M < 3\ M_\odot$. During each thermal pulse, two different neutron sources are activated, resulting in two different neutron exposures.
At the end of a thermal pulse strong convection between the He shell, the H shell and the envelope occurs and protons are mixed downward to the top layers of the He shell, which consists $\approx 75\%$ by mass of ^{4}He and $\approx 25\%$ by mass of ^{12}C. These protons induce the reaction sequence

$$^{12}\mathrm{C}(p,\gamma)^{13}\mathrm{N}(\beta^+\nu)^{13}\mathrm{C}(p,\gamma)^{14}\mathrm{N} \tag{1.7}$$

which results in two regions rich in ^{13}C (^{13}C-pocket) and ^{14}N (^{14}N-pocket), respectively. When temperatures around 0.09 GK are reached - corresponding to a thermal energy of $k_BT \approx 8$ keV, the reaction $^{13}\mathrm{C}(\alpha,n)^{16}\mathrm{O}$ becomes relevant and neutrons are released in the ^{13}C-pocket which are captured by pre-existing seed nuclei. Neutron densities are rather low with $N_n \approx 10^7$ cm^{-3}, but since the neutron irradiation lasts for about 5×10^4 years the neutron exposure is high (see values in Table 1.1). Due to the low neutron density only few branching points exist, and ^{13}C is completely consumed in the ^{13}C-pocket. During the subsequent thermal pulse ^{22}Ne is produced via

$$^{14}\mathrm{N}(\alpha,\gamma)^{18}\mathrm{F}(\beta^+\nu)^{18}\mathrm{O}(\alpha,\gamma)^{22}\mathrm{Ne} \tag{1.8}$$

activating the $^{22}\mathrm{Ne}(\alpha,n)^{25}\mathrm{Mg}$ source at ≈ 0.3 GK or $k_BT \approx 25$ keV. Neutron densities can reach $N_n \approx 10^{10}$ cm^{-3}, but the time scale is of the order of few hundred years, so neutron exposure is about ten times less compared to the $^{13}\mathrm{C}(\alpha,n)^{16}\mathrm{O}$ irradiation.

- **Weak component**
  The weak *s* process takes place in massive stars with $M > 8M_\odot$ in two steps. During core He burning the ^{14}N produced via the CNO cycle is transformed to ^{22}Ne via reaction sequence (1.8). Near He exhaustion in the core, the temperature becomes high enough to ignite the $^{22}\mathrm{Ne}(\alpha,n)^{25}\mathrm{Mg}$ neutron source ($k_BT \geq 22$ keV) which becomes more efficient with increasing temperature. Also some lighter elements from $35 < A < 45$ are synthesized in massive stars, since a network of (n,γ), (n,α) and (n,p) reactions builds up from Al to the Fe peak group [16], while from $60 < A < 90$ isotopes are efficiently produced via neutron captures and subsequent β^--decays. Above $A = 90$ there is no significant contribution from the weak component. If the mass of the star is smaller than $M < 30\ M_\odot$ some ^{22}Ne survives He burning and the $^{22}\mathrm{Ne}(\alpha,n)^{25}\mathrm{Mg}$ source is reactivated during carbon-shell burning, since α particles are produced via $^{12}\mathrm{C}(^{12}\mathrm{C},\alpha)^{20}\mathrm{Ne}$. During this stage thermal energies around 90 keV and high neutron densities of $N_n = 10^{11}$ cm^{-3} are reached. For carbon burning in the core the *s* process does not have any effect on the abundances in the universe since the core matter is destroyed during a supernova or via photo-disintegration during oxygen burning.

Table 1.1: Different *s* process features

	Main component		Weak component	
Stellar site	TP-AGB stars ($1.5M_\odot - 3M_\odot$)		Massive stars ($> 8M_\odot$)	
	H-He shell		He-Core	C-shell
Neutron source	$^{13}C(\alpha,n)^{16}O$	$^{22}Ne(\alpha,n)^{25}Mg$	$^{22}Ne(\alpha,n)^{25}Mg$	
Temperature (GK)	0.09	0.3-0.35	0.3-0.35	1
Temp. (k_BT-value)	8 keV	25 keV	25 keV	90 keV
Peak neutron density (N_n)	$10^7 - 10^8$ cm^{-3}	10^{10} cm^{-3}	10^7 cm^{-3}	10^{11} cm^{-3}
Mean exposure (τ_0)[a]	0.3 mb^{-1}		0.07 mb^{-1}	
Neutron captures per seed nuclei ^{56}Fe[b]	15.1		2.8	
Fraction of exposed seed nuclei ^{56}Fe[b]	0.043%		1.6%	

[a] Values at $k_BT = 30$ keV from Reference [13]

[b] from Reference [13]

Nuclear data needs

As underlined in the previous sections, neutron capture cross sections are the basic nuclear physics input for *s* process studies. Additionally, the accurate knowledge of *s* process abundances is essential for studying for example the *r* process since *r* abundances are calculated by subtracting the *s* component from the solar system abundances (see Section 1.4.2, Eq. 1.9). Figure 1.4 shows uncertainties of MACS as listed in a compilation by Bao *et al.*, published in 2000 [17]. According to References [10, 17], uncertainties of <5% in the stellar cross sections are required as input for calculations. For some mass regions this is already the case, but Figure 1.4 clearly indicates that further improvements are urgently needed, specifically in the mass regions $A < 120$ and $A > 180$. For a better study of *s* process environments *s* only and *s* process branching cross sections should be known with an accuracy of $< 1\%$. The same accuracy is needed for isotopes which exhibit anomalous abundances in meteoritic inclusions, since those are believed to show signatures of specific nucleosynthesis processes. Nuclei with magic neutron numbers, which represent bottlenecks in the reaction flow need to be determined with at least 3% accuracy. Of major importance are also neutron poisons, which are nuclides removing the available *s* process neutrons by (n,γ), (n,p) or (n,α) reactions, for example $^{14}N(n,p)$, $^{25}Mg(n,\gamma)$ and $^{22}Ne(n,\gamma)$. Even though their stellar cross section might be small, they may have a significant impact due to their high abundances. Apart from neutron cross sections, neutron scattering experiments are of importance to study nuclear levels which allow the calculation of stellar enhancement factors (see Section 2.4).

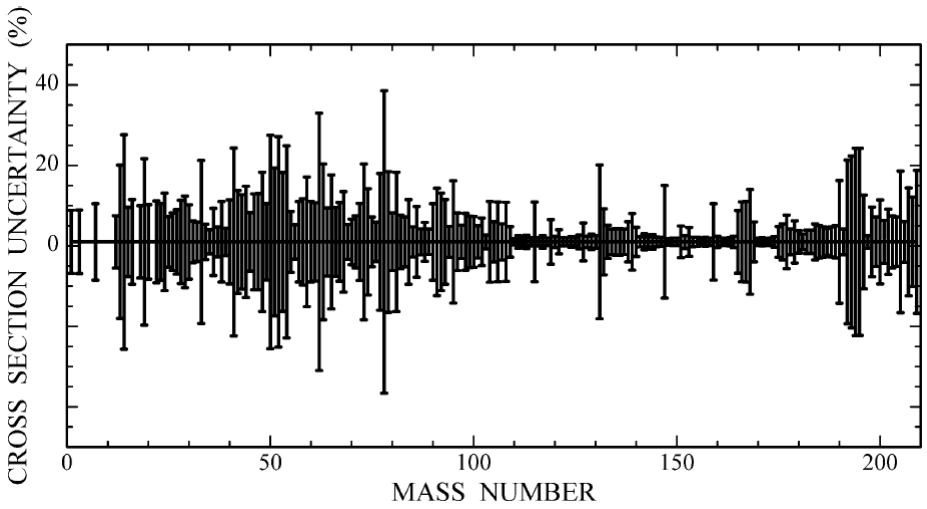

Figure 1.4: Uncertainties of experimental MACS at 30 keV neutron energy (as quoted in Reference [17]). The picture is taken from Reference [10].

1.4.2 r process

The rapid neutron capture process produces the remaining half of elemental abundances heavier than Fe neglecting the 1% p nuclei. For calculating r process abundances one usually subtracts the s process contribution from observed solar-system abundances:

$$N_r(A,Z) = N_\odot(A,Z) - N_s(A,Z) \tag{1.9}$$

In r process scenarios neutron densities are much higher ($T \geq 1$ GK, $N_n \geq 10^{21}$ cm^{-3}), driving the reaction flow close to the neutron drip-line, since (n,γ) and (γ,n) reactions are much faster than β^--decays. If temperatures and neutron densities are sufficiently large, the isotopic $(n,\gamma) \leftrightarrow (\gamma,n)$ chain is in thermal equilibrium, which means the abundance ratio $N(Z,A+1)/N(Z,A)$ depends only on the Q-value of the reaction ($Q_{n\gamma}$), temperature and neutron density. The r process reaction path runs along nuclides with constant neutron separation energy. Higher temperatures shift the path more towards the valley of stability, while higher neutron densities cause the opposite.
Light isotopes are rapidly destroyed and the abundance distribution peaks around nuclides with low $Q_{n\gamma}$-values. In the r process chain there are branchings via β^--decay to the $Z+1$ chain when nuclides with particularly low $Q_{n\gamma}$-values are encountered. Those "waiting points" are for example even-even nuclei or nuclei with a magic number of neutrons. The latter represents a special case where the r process path continues via β^--decay. After one neutron capture a magic shell configuration is reached again. This causes the reaction path to move vertically upwards along a magic neutron number approaching the valley of stability. The closer a nucleus is to stability, the longer are the

β half lives which delay the abundance flow and cause a built up of higher abundances for these isotones. At some point the chain is close enough to stability so that the $Q_{n\gamma}$-value is high enough and the *r* reaction path breaks out and proceeds again towards the neutron rich side.
When the neutron exposure stops, the *r* process products decay towards the valley of stability producing the broad peaks in the abundance distribution corresponding to decay products of the *r* waiting points at neutron magic shell configurations. These peaks are shifted to lower masses compared to the *s* process abundance peaks (see upper left corner in Figure 1.2). The final *r* process abundances depend on temperature, neutron density and nuclear properties, like $Q_{n\gamma}$-values (hence nuclear masses), β-decay half-lives, fission probabilities, etc.
The specific astrophysical sites of the *r* process are still unclear, but the high neutron densities, high temperatures and duration of the order of seconds needed suggest explosive scenarios, such as neutrino driven winds from a neutron star of a type II Supernova explosion (Core collapse supernova with hydrogen lines in its spectrum) [18, 19].

1.4.3 p process

The *p* process is responsible for production of stable nuclei on the proton rich side. Most probably the *p* process takes place in hot scenarios with temperatures of $T = 2 - 3$ GK. *p* nuclei are produced via (γ, n) reactions where nuclei with an even number of neutrons may act as waiting points. For neutron deficient nuclei and nuclei with a favorable neutron shell configuration, the competing reactions (γ, p) and (γ, α) become important, establishing branching points in the reaction path.
The seed nuclei for the *p* process are *s*/*r* products. This seed distribution is eroded by the photon-induced reactions, resulting in a reaction flow in the direction to lower masses. β^+-decays don't play a significant role since γ-induced reactions are much faster.

2 Radiative neutron capture

2.1 Introduction

The following chapter gives a brief overview on the theoretical background of neutron induced reactions, in particular neutron capture reactions. Later in this chapter the focus will be on nuclear reactions in stellar environments. More information can be found in References [5, 6, 20, 21, 22].
The probability for a nuclear reaction to occur can be expressed in terms of the cross section, which has the dimension of an area and can be written as:

$$\sigma \approx \pi \lambda\!\!\!^{-2} |H_{\mathrm{if}}|^2 \tag{2.1}$$

where $\lambda\!\!\!^{-}$ for a neutron induced reaction is given by

$$\lambda\!\!\!^{-} = \sqrt{\frac{m_n + m_t}{m_t}} \frac{\hbar}{(2 m_n E_n)^{1/2}} \tag{2.2}$$

with m_n and m_t being the masses of neutron and target, respectively. E_n is the kinetic neutron energy in the laboratory system and H_{if} is the probability matrix element to transform from the initial state to the final state and includes the remaining nuclear information.
If the reaction proceeds via a single step, it is called a direct reaction. These reactions are non resonant reactions, since their cross section varies smoothly with incident kinetic energy E_n. Direct reactions occur at all neutron energies and take place very fast with timescales of the order of $t \approx 10^{-20}$ s.
Compound nuclear reactions proceed through two stages and were proposed by Niels Bohr to explain the resonant behaviour of cross sections. First, projectile and target form a compound state with excitation energy $E_c = Q + E_{n,\mathrm{cm}}$, where Q is the Q-value of the reaction. The excitation energy E_c is shared amongst all nucleons. Then this compound state decays to its final state. Since E_c has to match an excited state in the compound system, large variations of orders of magnitude in the cross section are possible. The decay into the final state is independent of its formation and depends only on E_c, spin J and parity π of the compound and final state. The matrix element H_{if} represents a probability and thus, can be expressed in the form of a width Γ. As an example, the neutron capture cross section of a compound nucleus reaction can be described via

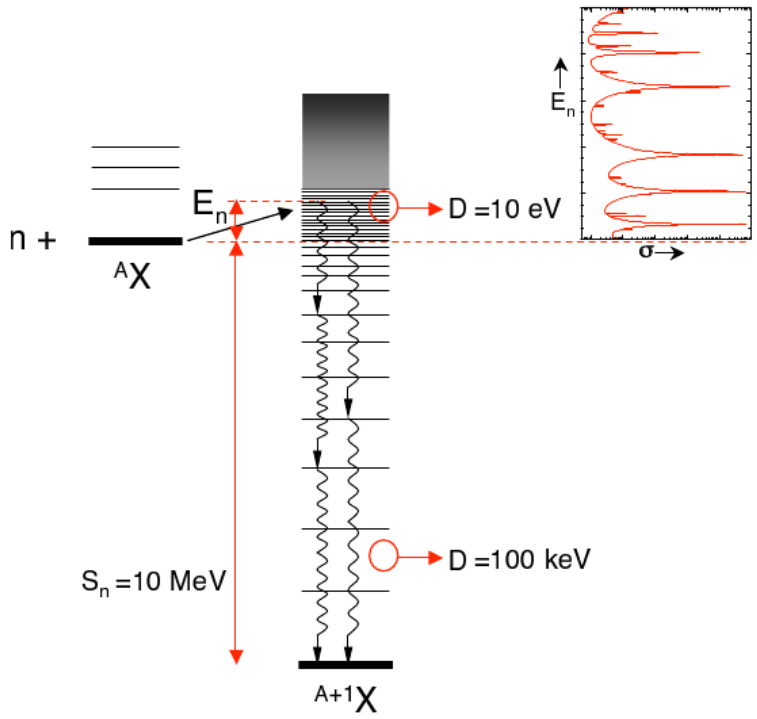

Figure 2.1: Scheme of a neutron capture reaction: the neutron and target nucleus ${}^{A}X$ form a compound nucleus ${}^{A+1}X^{*}$ with excitation energy $E_{n,\mathrm{cm}} + S_n$. The compound nucleus decays by a γ-ray cascade to the ground state of ${}^{A+1}X$. Picture taken from [20].

two partial widths:

$$\sigma \approx \pi \lambda^2 \Gamma_n(E_n)\Gamma_\gamma(E_c) \tag{2.3}$$

Γ_n is the partial width for forming the compound system, Γ_γ is the partial width for decay of the compound system via γ emission. The Q-value for a neutron capture reaction corresponds to the neutron separation energy S_n of the compound nucleus and is typically of the order of several MeV. The de-excitation of the compound nucleus proceeds via a cascade of γ rays with $E_c = \sum E_\gamma$. A sketch of such a compound reaction for neutron capture is shown in Figure 2.1. The wave function for describing such highly excited states is extremely complex. Level spacings D in heavy nuclei are of the order of eV and small changes in the neutron energy can excite completely different eigenstates of the system. Therefore, these states can only be described statistically, their specific position and properties have to be accessed in experiments.
The observed energy dependent cross section is a superposition of direct and compound reactions, which means that interference effects between the resonant and non resonant components may occur.

2.2 Resonances

As mentioned above compound nucleus reactions show a resonant behaviour. The neutron capture cross section shows a maximum for energies corresponding to eigenstates of the compound system. The cross section in the vicinity of a single, isolated s-wave resonance (orbital angular momentum $\ell = 0$) exhibits a Breit-Wigner shape of the form

$$\sigma(E_n) = \pi \lambda\!\!\!^{-2} g \frac{\Gamma_n \Gamma_\gamma}{(E_n - E_\mathrm{R})^2 + (\Gamma_\mathrm{tot}/2)^2} \tag{2.4}$$

This means, that the reaction cross section can be reproduced by knowing its resonance energy E_R, the partial widths Γ_γ and Γ_n, the total width Γ_tot, which is the sum of all partial widths and the spin-weighting factor g which accounts for the different combinations of target spin I, compound nucleus spin J and neutron spin s:

$$g = \frac{2J + 1}{(2I + 1)(2s + 1)} \tag{2.5}$$

where $J = I \pm 1/2$ since $s = 1/2$ and $\ell = 0$.
For $\ell = 0, \Gamma_n(E_n)$ is proportional to the velocity v_n of the incident particle. $\Gamma_\gamma(E_c)$ can be approximated as being constant. This leads to a cross section behaviour $\sigma(E_n) \propto 1/v$ at low neutron energies, since s-wave capture dominates as there is no centrifugal barrier (see e.g. Ref. [6]).
To remove the energy dependence from the neutron width one can define a reduced width using the penetrability P_ℓ of the centrifugal barrier:

$$\Gamma_n^\ell = \Gamma_n \frac{P_{\ell=0}}{P_\ell} \sqrt{\frac{1\ \mathrm{eV}}{E_n}} \tag{2.6}$$

As a consequence of the random nature of a compound system, resonance data show statistical behaviour. It was found that the level spacing D of resonances of the same spin J follow a Wigner probability distribution [23]

$$\mathcal{P}(D/\overline{D}) = \frac{\pi}{2} \frac{D}{\overline{D}} \exp(-D^2/(4\overline{D}^2)) \tag{2.7}$$

with $\overline{D}$ being the mean level spacing.
The reduced neutron widths for $\ell = 0$ resonances follow a Porter Thomas distribution [24, 25]:

$$\mathcal{P}(\Gamma_n^0/\overline{\Gamma_n^0}) = \frac{1}{\sqrt{2\pi}} \frac{1}{\sqrt{\Gamma_n^0/\overline{\Gamma_n^0}}} \exp(-\Gamma_n^0/(2\overline{\Gamma_n^0})) \tag{2.8}$$

In general, the resonance widths are increasing with neutron energy, while the level density decreases. The energy region where the widths of the resonances Γ_tot are smaller

than the level spacing D is called the Resonance Region (RR). This region can be further divided in the Resolved and the Unresolved Resonance Regions (RRR and URR, respectively), the latter denoting the energy region where the experimental resolution is not sufficient to separate resonances. If Γ_{tot} becomes comparable to D, resonances start to overlap. This region in the excitation function is called the Continuum Region.

2.3 R-Matrix Theory

Cross sections can be most accurately parametrized by the R-Matrix formalism if binary systems are involved only. The R-Matrix formalism uses the channel representation of nuclear reactions. Each channel c consisting of two particles is defined by their internal excitation, the channel spin $\vec{j}$, which is the vector sum of the spins of the two individual particles, total angular momentum $\vec{J} = \vec{j} + \vec{l}$ and its component in a specified direction m_j. Conservation of total angular momentum and parity is required for all stages of the reaction, e.g. when a compound nucleus is formed. The R-Matrix formalism distinguishes between an internal and an external region.
In the external region there is no nuclear potential, hence the potential for neutral particles is zero and charged particles only experience a Coulomb potential. The solution of the Schrödinger equation is a linear combination of incoming and outgoing waves

$$\psi = \sum_c y_c \psi_{\text{in}} + \sum_{c'} x_{c'} \psi_{\text{out}} \tag{2.9}$$

The coefficients x and y are connected by the collision matrix $\mathbf{U}$ with $x_{c'} \equiv -\sum_c U_{c'c} y_c$ containing information on the nuclear physics of the reaction. It is related to the reaction cross section through

$$\sigma_{cc'} = \pi \lambda_c^2 |\delta_{cc'} - U_{cc'}|^2 \tag{2.10}$$

In the internal region, which is confined inside the channel radius a_c which is commonly referred to as being $a_c \approx 0.8 + 1.23A^{1/3}$ fm [22], nuclear forces are involved and the corresponding wave function is very complicated. The internal wave function can be expanded in its eigenfunctions with eigenvalues E_λ. At the boundary $r = a_c$ the values and derivatives of the internal wave function have to match the external wave function. After several more steps (see e.g. Reference [26]) the collision matrix $\mathbf{U}$ can be expressed using the channel matrix $\mathbf{R}$:

$$\mathbf{U} = \boldsymbol{\Omega}\mathbf{P}^{1/2}[\mathbf{1} - \mathbf{R}(\mathbf{L} - \mathbf{B})]^{-1}[\mathbf{1} - \mathbf{R}(\mathbf{L}^* - \mathbf{B})]\mathbf{P}^{-1/2}\boldsymbol{\Omega} \tag{2.11}$$

$\mathbf{R}$ is the R-Matrix containing properties of the eigenstates

$$R_{cc'} = \sum_\lambda \frac{\gamma_{\lambda c}\gamma_{\lambda c'}}{E_\lambda - E} \tag{2.12}$$

where the eigenvalues E_λ are the level energies for a given state λ and $\gamma_{\lambda c}$ are the probability amplitudes which are connected to the partial width via the penetrability P_c

$$\Gamma_{\lambda c} = 2\gamma_{\lambda c}^2 P_c \tag{2.13}$$

L is a complex matrix containing a shift factor and the penetrability factor **P**; **Ω** is the quotient of the in- and the outgoing wave function at $r = a_c$ and **B** contains the boundary condition for matching the internal and the external wave function. All matrices except **R** and **U** are diagonal and directly related to the solution of the Schrödinger equation in the external region. The parameters of the R-Matrix describe the process of the reaction and can only be accessed by experiments.
Since the inverse of the R-Matrix is required to obtain a cross section, several approximations can be made to facilitate the calculations. The most simple approximation is the Single-Level-Breit-Wigner approximation, which takes into account only one level. The cross section for $\ell = 0$ then reduces to

$$\sigma_{cc'} = 4\pi\lambda\!\!\!^{-2}_c g_c \frac{\Gamma_{\lambda c}\Gamma_{\lambda c'}}{(E - E_\lambda - \Delta_\lambda)^2 + \Gamma_\lambda^2/4} \tag{2.14}$$

with a shift Δ_λ (cf. Eq. 2.4). Often the boundary condition is chosen such that the shift Δ_λ disappears.
A bit more extensive is the Multi-Level-Breit-Wigner approach. In this case only the off-diagonal elements in the level matrix are neglected, which means that interferences between different channels are not taken into account. The most accurate approximation is the Reich-Moore approximation, which neglects the off-diagonal matrix elements for the photon channel.

2.4 Nuclear reactions in stellar environments

In a stellar interior the plasma is considered to be in thermodynamic equilibrium which means that particle velocities follow a Maxwell-Boltzmann distribution

$$\phi(v)dv = 4\pi v^2 \left(\frac{m}{2\pi k_B T}\right)^{3/2} \exp\left(-\frac{mv^2}{2k_B T}\right)dv \tag{2.15}$$

$\phi(v)dv$ is the probability to find a particle with a velocity between v and $v + dv$. T is the stellar temperature and k_B the Boltzmann constant. Thus, the reaction rate per particle pair $< \sigma v >$, where v denotes now the relative velocity between the two particles, can be written as

$$< \sigma v >= \int_0^\infty \phi(v)\sigma(v)v dv \tag{2.16}$$

which becomes (transforming v to energy E):

$$< \sigma v >= (\frac{8}{\pi\mu})^{1/2} \frac{1}{(k_B T)^{3/2}} \int_0^\infty \sigma(E) E \exp(-\frac{E}{k_B T}) dE \tag{2.17}$$

with the reduced mass $\mu = m_1 m_2/(m_1 + m_2)$. As noted in the previous section, the neutron capture cross section at low neutron energies is proportional to $1/v$. Hence, the reaction rate per particle pair $< \sigma v > \approx$ const. The most probable energy for a neutron capture to occur is near $E = k_B T$ corresponding to a relative speed of $v_T = \sqrt{2 k_B T/\mu}$. The stellar or Maxwellian-averaged cross section is then defined as:r

$$< \sigma >= \frac{< \sigma v >}{v_T} = \frac{2}{\sqrt{\pi}} \frac{1}{(k_B T)^2} \int_0^\infty \sigma(E) E \exp(-\frac{E}{k_B T}) dE \tag{2.18}$$

Due to the high temperatures in stars, nuclei in the plasma may be present not only in their ground states but also in excited states. These excited states have different reaction cross sections which consequently, modify the overall reaction rates. The reaction rate in stellar environments divided by the reaction rate obtained in laboratory measurements of ground state nuclei is called Stellar Enhancement Factor (SEF). In general, reaction cross sections of excited states cannot be measured directly, therefore the SEF for a reaction has to be calculated by statistical models (see e.g. [27, 28]). Radioactive decay-rates may also be affected by stellar conditions. The population of excited states can lead to different effective half lives due to different properties of the excited state compared to the ground state. In stellar interiors the matter is ionized, which influences electron capture rates as well as β^--decay rates. The latter is caused by the possibility of decay into a bound state (which means that the emitted electron becomes a shell electron). Stellar decay rates have been calculated for example by Takahashi and Yokoi [29].

3 The time-of-flight technique

3.1 Introduction

The time-of-flight technique enables the measurement of energy dependent reaction cross sections. It is based on detecting the prompt reaction product (e.g. the γ cascade after radiative capture) at a well-known time which provides information on the neutron time-of-flight t_f, defined as the time difference between the generation of the neutron and detection of the reaction product. The neutron energy is then determined via its time-of-flight through the relation:

$$E_n = m_n c^2(\gamma - 1) \tag{3.1}$$

where m_n is the neutron mass, L is the length of the flight path and c is the speed of light. γ is defined as:

$$\gamma = \frac{1}{\sqrt{1 - (L/t_f)^2/c^2}} \tag{3.2}$$

For the classical case equation 3.1 becomes

$$E_n = \frac{1}{2} m_n \left(\frac{L}{t_f}\right)^2 \tag{3.3}$$

The time-of-flight technique requires a pulsed neutron beam, which is usually produced by nuclear reactions triggered by a charged particle beam impinging on a target. Depending on the physical motivation of the experiment, different types of neutron spectra may be of interest.
"White" neutron spectra, in which the neutron energy extends over several orders of magnitude, are generated via spallation (e.g. n_TOF (CERN) [30] and LANSCE (*Los Alamos National Laboratory*) [31]) or photo-disintegration reactions (e.g. GELINA (*Institute for Reference Materials and Measurements*) [32] and ORELA (*Oak Ridge National Laboratory*) [33]). At spallation sources, a proton beam of energies in the GeV region impinges on a target, typically made of heavy material, e.g. Pb. Spallation reactions are the most efficient way for producing neutrons since many neutrons are produced for each incident primary particle. In the case of n_TOF one proton produces on average about 300 neutrons. To produce neutrons via photo-disintegration an electron beam, 40-200 MeV in energy is used. The electrons produce Bremsstrahlung by

traversing the target of preferably high atomic number Z materials, like U and Ta. Neutrons are generated via (γ, n), $(\gamma, 2n)$ or (γ, f) reactions. To obtain higher neutron fluxes at low neutron energies, a neutron moderator is placed around the target, generating an almost $1/E_n$ behaviour of the neutron flux at energies below 1 MeV.
If a limited neutron energy range is of interest, neutrons can be produced by nuclear reactions such as fusion reactions like $d + d$ or $d + t$ producing quasi monoenergetic neutrons in the MeV range - the details of the spectrum depend on the incident particle energy and angle with respect to the incident beam. For astrophysical studies, neutron cross sections in the keV region are of interest. Neutron spectra suited for measuring Maxwellian-averaged cross sections can be produced by some (p, n) reactions. The reaction ^{7}Li$(p, n)^{7}$Be which approximates a quasi stellar neutron spectrum at $k_BT = 25$ keV is most commonly used [34]. This reaction will be further discussed in Chapter 6. Furthermore, spectra with $k_BT = 5$ keV and $k_BT = 52$ keV can be generated via the ^{18}O$(p, n)^{18}$F and ^{3}H$(p, n)^{3}$He reactions, respectively [35, 36].
Important properties of a time-of-flight spectrometer are neutron energy resolution and neutron flux. Both features are related to length of the neutron flight path. A longer flight path typically results in a better neutron energy resolution, while the neutron flux ϕ decreases quadratically with flight path. Therefore, a compromise between resolution and neutron intensity needs to be found. Other limiting factors for the energy resolution are the pulse width of the charged particle beam and the properties of neutron target and moderator (if present). Furthermore, time-of-flight experiments require detectors with a small charge collection time (≈ns) and fast electronics to allow high time resolution.

3.2 The n_TOF/CERN facility

The time-of-flight facility n_TOF is located at CERN and started operation in 2001. A detailed description of the facility is available in References [37] and [38]. At n_TOF, neutrons are produced by spallation reactions of a proton beam delivered by the Proton Synchrotron (PS), 20 GeV/c in momentum, impinging on a massive Pb block. A nominal proton pulse with a width of 7 ns RMS (Root Mean Square) has an intensity of 7×10^{12} protons producing approximately 2×10^{15} neutrons at the target location. These pulses are referred to as ”dedicated” pulses. n_TOF receives also another pulse type with about half of the nominal intensity (”parasitic” pulses). The repetition rate is approximately 0.4 Hz. This low rate allows measuring down to small neutron energies and avoids background from neutrons originating from previous pulses (the so-called ”wrap around neutrons”). The Pb target is surrounded by a water layer for cooling purposes which acts also as moderator of the high-energy neutrons produced in the spallation target. This results in a white neutron spectrum ranging from thermal energies to several GeV.
Neutrons travel from the spallation target through an evacuated beam pipe approximately 185 m to the experimental area (EA). The beam pipe is installed at an angle

of 10° with respect to the proton beam to reduce background from highly energetic charged particles and γ rays. Additionally, a 1.5 Tesla magnet is placed at a flight path of approximately 150 m to remove charged particles from the beam. The experimental area is protected from background due to secondary reaction products by massive iron and concrete shielding along the flight path. Two collimators, at 140 m and at 176 m from the spallation target, respectively, are used to shape the size of the neutron beam. For capture measurements, the latter has a diameter of 1.8 cm, resulting in a beam size of about 4 cm diameter at the position of the capture setup. In total, about 1.2×10^6 neutrons per pulse ($E_n < 100$ MeV) reach the experimental area. A layout of the n_TOF facility is shown in Figure 3.1.

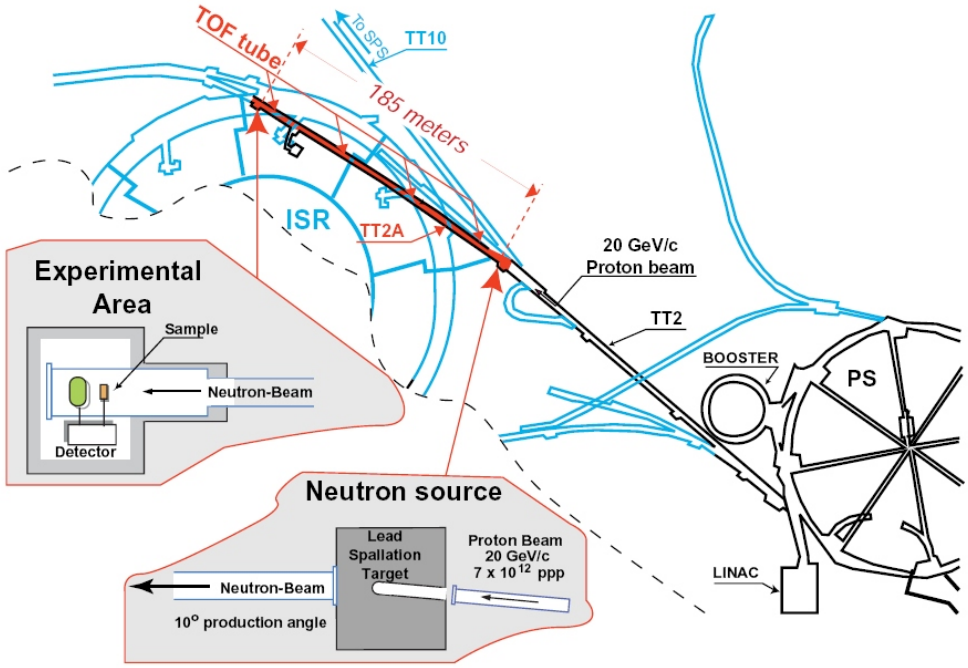

Figure 3.1: Layout of the n_TOF facility at CERN. Figure from Ref. [37]

For capture measurements two complementary detection setups are used; a 4π BaF_2 array called TAC (Total Absorption Calorimeter) [39] for detection of the full prompt γ cascade and a pair of C_6D_6 liquid scintillators [40]. In this work, all data were taken with the C_6D_6 detection setup, which will be described in more detail in the following section.

The full pulse shape of the detector signals is recorded with Flash ADCs at a sampling rate of 500 MHz. This corresponds to a time resolution of 2 ns. To minimize the data to be stored, zero suppression is performed on-line, which means that only signals are recorded which exceed a certain threshold. The PS accelerator sends a trigger signal to

the n_TOF data acquisition for each proton pulse. Such a signal is used to start the data acquisition. Data are recorded on a buffer memory, which is typically 8 MBytes. For the 500 MHz sampling rate the time window is therefore 16 ms long, corresponding to a minimum neutron energy of 0.7 eV. In some cases, a smaller sampling rate or a larger buffer memory allows to extend the time-of-flight window. In 2010 the data acquisition was adapted to measure for 80 ms. This allows to measure down to ≈0.027 eV, which is very close to the thermal neutron energy of 0.0253 eV.

At n_TOF, measurements were performed during two periods, called Phase I and Phase II. In Phase I, from the years 2001-2004, a Pb spallation target with the dimensions of 80×80×60 cm^3 [37] was used. In 2004, problems with increasing radioactivity in the cooling water stopped operation. In the following years a new Pb target was designed and installed in place of the old target. It has a cylindrical shape with a diameter of 60 cm and a length of 40 cm [41]. n_TOF received the first neutron beam of Phase II in autumn 2008 and cross section measurements have been performed again since spring 2009.

3.2.1 C_6D_6 detection setup

The C_6D_6 detection setup consists of two liquid scintillation detectors filled with deuterated benzene. The detectors are placed symmetrically around the beam pipe, 90° in angle with respect to the neutron beam. They are mounted 9.5 cm upstream of the sample, which results in detecting γ rays at an effective angle of about 125° relative to the neutron beam direction. This avoids angular distribution effects of resonances with $\ell > 0$ and reduces the background due to sample-scattered γ rays which are emitted preferentially in forward directions (in-beam γ rays, see section 3.3.3 for more detail). The samples are mounted on a ladder made of carbon fibre comprising five sample positions. The material carbon fibre was chosen since carbon has a very small neutron capture cross section and therefore introduces only a small additional background for capture measurements. The remotely controllable ladder can be moved vertically to place different samples in the neutron beam. Each sample is glued onto a 75 μm thick Kapton foil, fixed on a Carbon fibre frame. Figure 3.2 shows a sketch of the experimental setup.

Scattered neutrons which are captured in the detector can introduce a sizable background component for capture experiments. Therefore, the detectors are optimized for low neutron background by reducing structural material and using material with small neutron cross sections. This provides an advantage with respect to the TAC detection system for measuring samples with a high scattering to capture cross section ratio. The neutron sensitivity, which is the efficiency ratio for detecting a neutron vs. detecting a γ ray for these detectors is $\varepsilon_n/\varepsilon_\gamma \approx 3 \times 10^{-5}$, which is a factor of $\approx 3 - 10$ lower compared to commercial detectors [40]. Due to their faster recovery time after the prompt γ

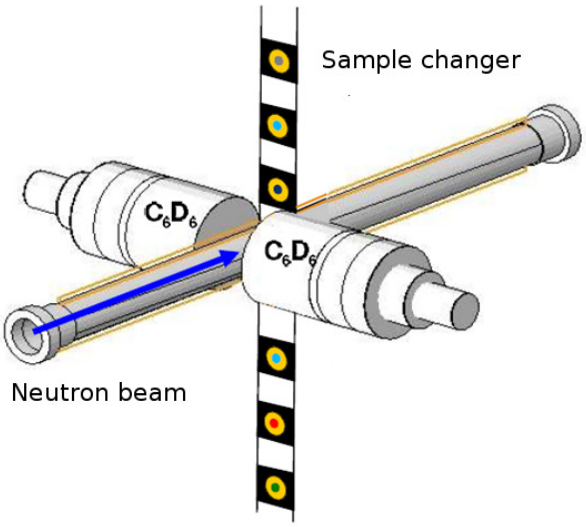

Figure 3.2: Sketch of the two C_6D_6 detectors and the sample exchanger mounted in the experimental area. Picture from Ref. [I1].

flash (prompt signal due to photons and ultra-relativistic particles produced in the target station, see section 3.3.1), the C_6D_6 detectors allow to measure cross sections up to the MeV region, whereas the maximum neutron energy currently accessible by the TAC is limited to around 20 keV. On the other hand, the TAC has higher detection efficiency and allows a large suppression of some background components such as the one related to the natural radioactivity of the sample and to competing reactions (e.g. fission). The rejection of the background in the TAC is made by applying a suitable threshold on the total energy of the detected event.

3.2.2 Neutron beam characteristics

The neutron flux as a function of energy has an isolethargic behaviour, with an energy dependence close to $\approx 1/E_n$. As mentioned in Section 3.1, this shape is typical for moderated spallation sources. At n_TOF, several detectors are installed to measure and monitor the neutron flux. The neutron flux ϕ denotes the neutrons per nominal proton pulse and energy reaching the experimental area. At n_TOF, the flux is expressed as neutrons/7×10^{12}protons/ln(E_n[eV]) due to its isolethargic behaviour. The neutron fluence Φ is the time integrated number of neutrons in the EA.

A Silicon detection system, SiMon, is in permanent operation and acts as in-beam monitor. It consists of a thin Li foil (200 μg/cm^2) positioned within the neutron beam. The products of t and α of the reaction ^{6}Li$(n,t)\alpha$ are detected in four Si detectors placed

outside of the neutron beam. The cross section of the ^{6}Li(n,t) reaction is considered as standard cross section by the International Atomic Energy Agency IAEA from thermal to 1 MeV neutron energy [42]. From neutron energies around 1 keV the data of SiMon need to be corrected for angular distribution effects. Additionally, SiMon is used for checking the stability of the proton reading provided by the pick-up signal of the PS accelerator which is commonly used for normalizing the individual runs for their total neutron fluence.
The flux is measured in dedicated runs with a reference fission chamber loaded with ^{235}U. The cross section of the reaction ^{235}U(n,f) is also used as standard cross section for thermal neutron energies and from 0.15 MeV to 200 MeV [43]. The information of both detectors was combined to evaluate a neutron flux with a final uncertainty of 2% for n_TOF phase I [44].
In Phase II, a MicroMegas (MGAS) detector was added for measuring the neutron flux, as well as the neutron beam profile, since its anode can be segmented [45]. The neutron converters used were ^{10}B and ^{235}U, producing charged particles via the reactions ^{10}B(n,α) and ^{235}U(n,f).

In 2010, boron was added to the water moderator circuit of the spallation target to reduce background from γ rays contaminating the neutron beam in the keV neutron energy region. The largest component of this contamination is originating from 2.2 MeV γ rays coming from radiative neutron capture on hydrogen (see section 3.3.3). The addition of boron in the moderator circuit modifies the neutron flux at thermal neutron energies due to the high thermal capture cross section of ^{10}B [41].
The neutron flux of Phase II was evaluated using SiMon, MGAS and the PTB fission chamber [46]. A comparison of the neutron flux at n_TOF flux in Phase I and Phase II (with and without boron in the water), is shown in Figure 3.3. The uncertainties of the evaluated flux for the years 2009-2011 are listed in Table 3.1.

Table 3.1: Uncertainties for different neutron energy regions for the Phase II neutron flux.

Energy range	Systematic	Statistical
0.025 eV - 1 keV	< 2%	2%
1 keV - 8 keV	2.5%	2%
8 keV - 80 keV	5%	2-3%
80 keV - 10 MeV	3-4%	2-4%

The neutron beam profile was determined experimentally in Phase I with a MGAS detector. Additionally, Monte Carlo (MC) simulations have been performed which were in excellent agreement with the measurement [47]. In Phase II, the beam profile was measured with the MGAS detector and also with a MEDIPIX detector [48], which is a

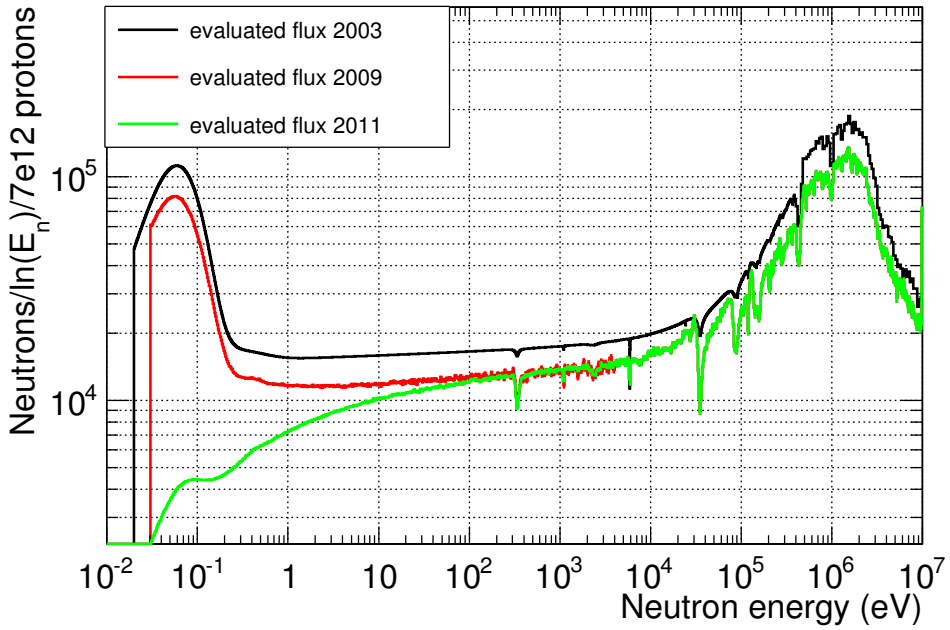

Figure 3.3: Evaluated neutron flux at n_TOF of the year 2003 (Phase I) compared to the year 2009 and 2011 (Phase II). The effect of the borated water moderator is visible an intensity loss in thermal neutrons for the 2011 flux due to the high neutron capture cross section of ^{10}B.

segmented Si detector. The neutron converters for the MEDIPIX detector were LiF for energies below 1 keV, using the ^{6}Li(n,t) reaction and Polyethylene for energies above 1 keV, detecting recoil protons. The MEDIPIX electronics allowed only to measure the beam profile over large neutron energy ranges, and it turned out that the data had too low statistics in the range from 1 eV to 80 keV. At thermal neutron energies ($<$ 1 eV) the beam profile was in fairly good agreement with simulations, as well as at the higher energies, from 80 keV to 200 MeV [49]. The analysis of the MEDIPIX data was not pursued further due to problems with the intermediate energy region and poor neutron energy resolution. Figure 3.4 shows the measured beam profile of neutrons with $E_n <$ 1 eV. The data are fitted with a function which is the convolution of a 2-dimensional Gaussian with a step function, the latter simulating the effect of a Gaussian distribution going through a collimator [47].
For the MGAS detector a ^{10}B converter exploiting the ^{10}B(n,α) reaction was used. The analysis of these data is still underway [50]. Some preliminary results will be used in Chapter 4 for discussing the data analysis.

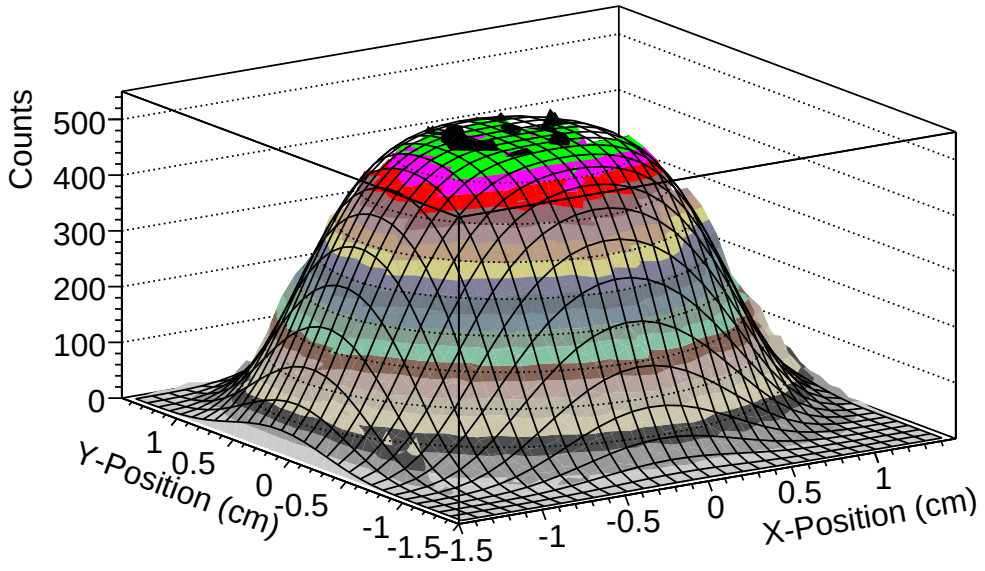

Figure 3.4: Measurement of the beam profile of neutrons with $E_n < 1$ eV with the MEDIPIX detector in 2009 placed at a flight path of 183 m. The x and y position is given in cm from the geometrical centre of the detector. For a better illustration the data are fitted to a Gaussian convoluted with a step function.

3.3 Data analysis

The quantity measured in a time-of-flight experiment is the reaction yield, which is the number of reactions per initial projectile and takes values of $0 < Y < 1$:

$$Y_{n\gamma} = \frac{C - B}{\epsilon\phi} \tag{3.4}$$

C are the counts, B the background, ϵ is the detection efficiency and ϕ is the neutron flux on the sample area. The cross section for the first interaction of a projectile with the sample can then be extracted using the following relation, which takes into account self shielding effects of the projectile crossing the sample volume:

$$Y_{n\gamma} = (1 - e^{-n\sigma_{tot}})\frac{\sigma_{n\gamma}}{\sigma_{tot}} \tag{3.5}$$

$\sigma_{n\gamma/tot}$ is the capture/total cross section and n is the sample thickness in atoms per area. Additionally, the capture yield needs to be corrected for multiple scattering effects, i.e. a subsequent neutron capture reaction after one or more elastic scattering events in

the sample (see also Section 3.3.5). The following sections describe the data analysis that was applied for the n_TOF data. Details about the individual measurements are presented in Chapters 4 and 5.

3.3.1 Determination of neutron energy and resolution

The neutron energy E_n is obtained by measuring its time-of-flight (equation 3.3) and the flight path. The time-of-flight t_f is determined by the difference of the time t, when the reaction occurs, and the time the neutron is created t_0:

$$t_f = t - t_0 \tag{3.6}$$

For radiative capture, t can be approximated by the time when the γ ray is detected. When the charged particle beam impinges on the spallation target, prompt γ rays and ultra-relativistic particles are generated. They produce a pronounced signal in the detectors at the time t_γ. Such a signal, called γ-flash, can be used to extract t_0 with

$$t_0 = t_\gamma - L/c \tag{3.7}$$

The variables L and t_f for extracting the neutron energy suffer from uncertainties. Using the classical time-energy relation of equation 3.3 one finds for the relative uncertainty in neutron energy:

$$\frac{\Delta E_n}{E_n} = 2\sqrt{\frac{\Delta t_f^2}{t_f^2} + \frac{\Delta L^2}{L^2}} \tag{3.8}$$

The neutron energy resolution achievable is essentially determined by five effects:

- Doppler broadening due to the thermal motion of target atoms in the sample. The Doppler width of the neutron energy according to the Free Gas Model is given by

  $$\sigma = \sqrt{2k_B T_{eff} E_n / A} \tag{3.9}$$

  (from reference [21], p. 160, eq. (13)), where A is the mass number and T_{eff} is the effective temperature $T_{eff} \approx 3/8 \times \theta \coth(3/8 \times \theta/T)$. θ and T are the Debye temperature and the temperature, respectively.

- the proton beam width, which is 7 ns RMS at n_TOF.

- the neutron moderator around the target: the neutrons travel some distance through the spallation target and the target moderator (moderation distance). This broadens the time-of-flight distribution and increases the measured time-of-flight, which accordingly results in a shift towards lower neutron energies. The moderation distance is increasing with neutron energy. This variation can be expressed as a time

equivalent δt_f, which is (68 ± 13) ns at n_TOF [51] and was extracted by comparing measurements of well known resonances to nominal values. A similar value of 73 ns was obtained from MC simulations. The moderator affects the shape of a measured resonance. A resolution broadened resonance has an asymmetric shape with a tail towards lower energies. The simulated resolution can be parametrized with an analytic function, called RPI function[1] which consists of a chi-squared distribution and two exponential functions describing the tail of the resonance. This resolution function (RF) was determined from simulations and verified by analyzing well known resonances in Fe between 10 and 200 keV [37, 52]. For neutron energies up to ≈ 100 keV the RF of Phase I can be used also for Phase II data.

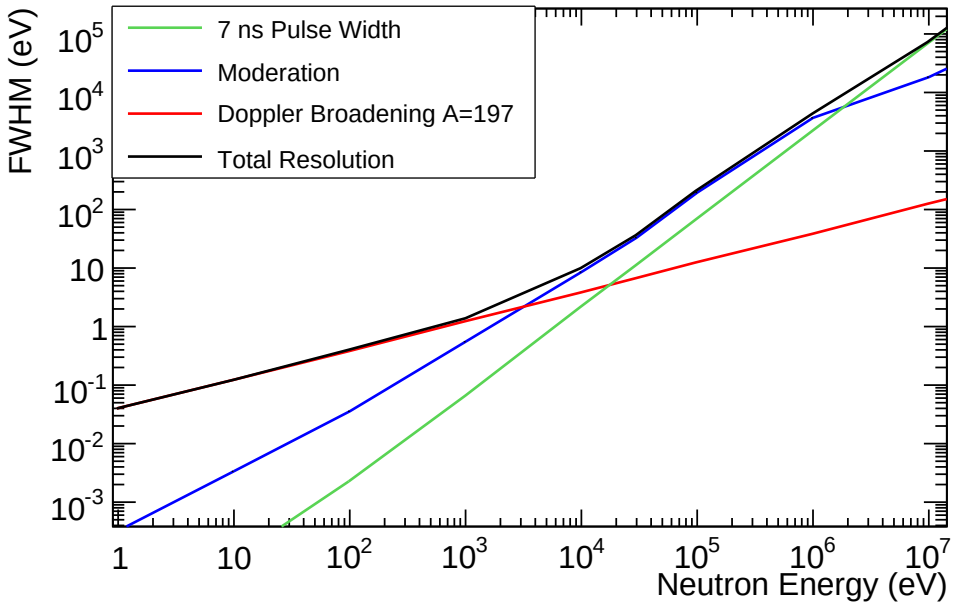

Figure 3.5: Energy resolution (FWHM) as a function of neutron energy at a flight path of 187.5 m. The contribution caused by Doppler broadening calculated for a Au sample is indicated in red and dominates at low neutron energies. From about 1 keV the moderator becomes the limiting factor of the resolution (blue). For very high energies from 1 MeV, the 7 ns pulse width of the PS accelerator becomes the highest contribution (green). The black line indicates the total resolution.

- the flight path L, consisting of the geometrical flight path plus the moderation distance. It is most convenient to determine the flight path by measuring well

[1] RPI stands for Rensselaer Polytechnic Institute (USA), where this function was first used.

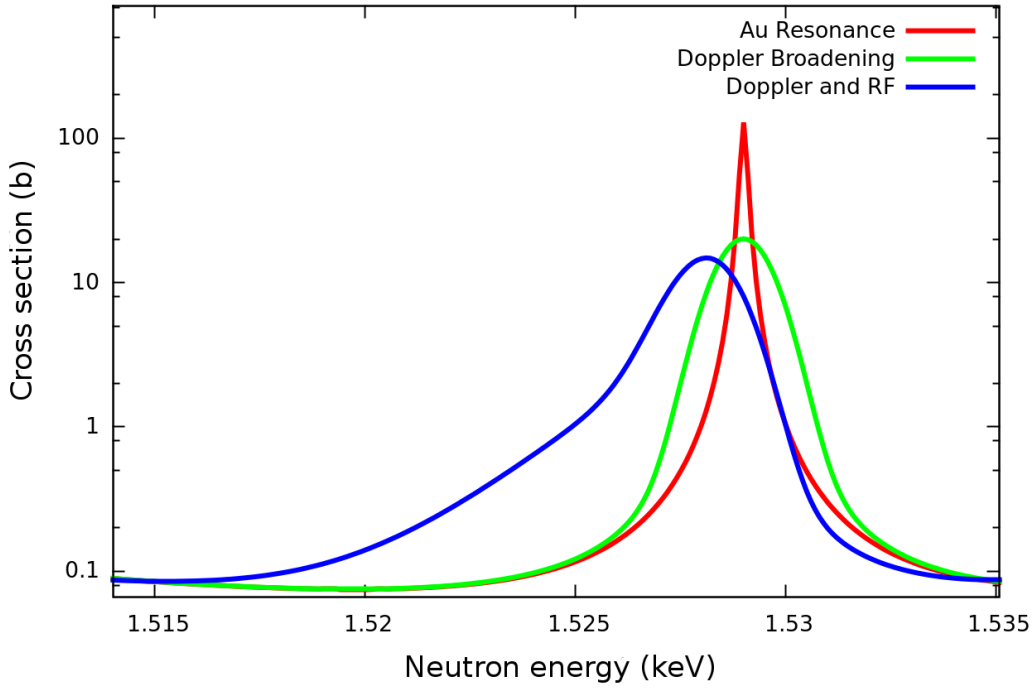

Figure 3.6: The cross section of a resonance in Au at 1.529 keV is calculated without broadening effects (red), with Doppler broadening (green) and with Doppler and Moderator broadening by implementing the n_TOF RF (blue). The calculation was done using the code SAMMY [53] for a Au sample with a thickness of 5.838×10^{-4} atoms per barn.

known resonances and matching the flight path to obtain the correct resonance energy E_R. This allows to determine the flight path up to a precision of a few cm which corresponds to a relative uncertainty of less than 0.1%. Contrary to the effects listed above this uncertainty introduces only an offset in neutron energy but has no broadening effect.

- the time response of the detectors, which can be neglected in the present case.

Figure 3.5 shows the resolution as a function of energy for the n_TOF facility. The resolution at low energies is clearly dominated by Doppler broadening, here calculated for a Au sample, whereas at higher energies moderation effects become more important. From around 1 MeV also the pulse width of the proton beam makes a significant contribution. The Doppler broadening was calculated according to Eq. 3.9, the values for the moderator resolution were taken from Reference [37] (Appendix, p. 145). All values are for a flight path of 187.5 m. The effect of thermal and moderation broadening for the calculated resonance at $E_R = 1.529$ keV in Au is plotted in Fig. 3.6.

3.3.2 Pulse height weighting technique

The efficiency of C_6D_6 scintillators for detecting the prompt γ-ray cascade produced in neutron capture reactions depends in a complex way on the de-excitation path of the compound nucleus. If the efficiency is low, i. e. at most one γ-ray of the cascade is detected, which is the case for the C_6D_6 detection setup, it is possible to apply the Pulse Height Weighting Technique (PHWT) [54]. More information on the use of the PHWT in neutron capture measurements can be found in References [55, 56].
Assuming that the efficiency to detect a single γ ray of the cascade is a linear function of γ energy E_γ,

$$\epsilon_{\gamma,i} = kE_{\gamma,i} \tag{3.10}$$

the efficiency to detect a capture event then can be written as 1 minus the efficiency not to detect any of the m emitted γ rays in the cascade:

$$\epsilon_c = 1 - \prod_{i=1}^{m}(1 - \epsilon_{\gamma,i}) \tag{3.11}$$

For low efficiency systems the detection efficiency for one capture can be approximated as a linear function of the excitation energy:

$$\epsilon_c \approx \sum_{i=1}^{m}(\epsilon_{\gamma,i}) = \sum_{i=1}^{m} kE_{\gamma,i} = kE_c \tag{3.12}$$

Detectors commonly don't exhibit a detection efficiency which increases linearly with γ energy. The PHWT is an *a posteriori* software manipulation of the detector response to achieve this linearity. A pulse height dependent weight is applied to each detected signal. These weights can be parametrized by weighting functions (WF).
WFs are determined by simulating the response of the detection setup, taking into account the details of the experimental geometry. The detector response is a function $R(E_{\mathrm{dep}}; E_\gamma)$ with E_{dep} being the deposited energy in the detector and E_γ being the incident γ energy, where E_{dep} can range up to E_γ. The efficiency to detect a γ ray is a sum over all corresponding response functions for deposited energies from $E_{\mathrm{dep},i} > 0$ to $E_{dep,i} = E_\gamma$:

$$\sum_j R(E_{\mathrm{dep},j}; E_\gamma) = \epsilon_\gamma \tag{3.13}$$

The weighting function has to fulfill the condition

$$\sum_j W(E_{\mathrm{dep},j}) R(E_{\mathrm{dep},j}; E_\gamma) = kE_c \tag{3.14}$$

for all γ energies up to $E_\gamma = E_c$. $W(E_{\mathrm{dep},j})$ is the weight that needs to be applied for the deposited energy $E_{\mathrm{dep},j}$. Often, a polynomial WF is used to express the weights

$W(E_{\mathrm{dep}}) = \sum_n a_n E_{\mathrm{dep}}^n$. The coefficients are then fitted by minimizing the expression:

$$\min\left[\sum_i\left(\sum_j\sum_n a_n E^n R_{j,i} - kE_{\gamma,i}\right)^2\right] \tag{3.15}$$

Usually, k is chosen as 1 MeV^{-1}.

3.3.3 Background

There are several background components at n_TOF which need to be taken into account:

- **ambient background:** This background is present also without a neutron beam (e.g. cosmic rays). It becomes especially important for measurements of radioactive samples emitting γ rays. The ambient background is measured in runs without beam in calibration mode. That means that an artificial trigger is used to start the acquisition for the usual 16 ms (resp. 80 ms for 2011 runs). The ambient background can be calculated by scaling the beam-off runs to the number of proton bunches of the beam-on runs.

- **sample-independent background:** This is a background generated by the neutron beam without the presence of a sample. It is mostly due to interaction of the neutron beam with material (e.g. vacuum windows) in the experimental area. It is determined by recording runs with an empty sample frame in the sample holder.

- **neutron induced background:** The neutron induced background which comes from neutrons scattered from the sample can be further divided in two components. One component, here also called "delayed neutron background" is caused by neutrons, which are producing γ signals corresponding to a time-of-flight which is not strongly correlated to their initial energy. Therefore, this background is smooth in neutron energy and its shape can be estimated by measuring the yield of a suitable sample. A reference sample should have a scattering cross section which is much higher than the capture cross section and no resonance in the investigated energy range, e.g. carbon. The second component, here called "prompt neutron background" affects the resonance analysis. Since for some resonances the scattering width can be orders of magnitude higher than the capture width, a large amount of neutrons is scattered from the sample. This may produce additional events at the resonance energy due to capture of those sample-scattered neutrons in the close structure material (e.g. the detector walls) and cannot be distinguished from real neutron capture. Due to the very small neutron sensitivity of the C_6D_6 detectors, this background is kept considerably small.

- **in-beam γ rays:** This background component consists of γ rays in the neutron beam which appear at time-of-flights corresponding to 200 eV-500 keV neutron energy. These γ rays can be scattered from the sample into one of the detectors. They are produced by radiative capture of neutrons in the target area. The largest part of this background comes from 2.2 MeV γ rays, which are emitted following neutron capture on hydrogen in the water moderator. The in-beam γ-ray background was significantly reduced when using borated water in the moderator. Neutrons are then preferably captured in ^{10}B, causing a γ ray of 0.48 MeV, which can be suppressed with much higher efficiency by the threshold set in the detectors and by applying weighting functions. The shape of the γ-ray background resembles a bump, with the highest contribution in the keV region (see Chapter 5). Its shape and magnitude can be measured with a high Z material, like a Pb sample.

- **inelastic background:** Inelastic neutron scattering is another source of background. γ rays are emitted if the kinetic neutron energy is high enough to populate excited states in the target nucleus. Therefore, this background strongly depends on the isotope which is measured since it appears at neutron energies corresponding to energies of the first excited states. Up to $\approx$ 200 keV this background is rejected due to the energy threshold in the detectors. For higher neutron energies the inelastic channels introduce a background that cannot be corrected and limits the maximum accessible neutron energy.

To normalize the smooth, sample dependent background to the sample of interest, neutron filters are placed into the beam. These neutron filters are thick enough to exhibit black resonances, which means that no neutron is transmitted at certain resonance energies. The background is then scaled to the resonance dips. This procedure was applied for analyzing the Au cross section and more details can be found in Chapter 5. Table 3.2 lists the filters with their black resonance energy $E_{\mathrm{R,black}}$ and thickness used for the measurements reported here. Figure 3.7 shows the calculated transmission of neutrons through the most commonly used filters Al, Co, Mo and W.

Table 3.2: Black resonance filters used in this work.

Material	Al	Co	W
Thickness (mm)	29.4	0.25	0.8
$E_{\mathrm{R,black}}$	34.8 keV	132 eV	4.2 eV, 18.8 eV

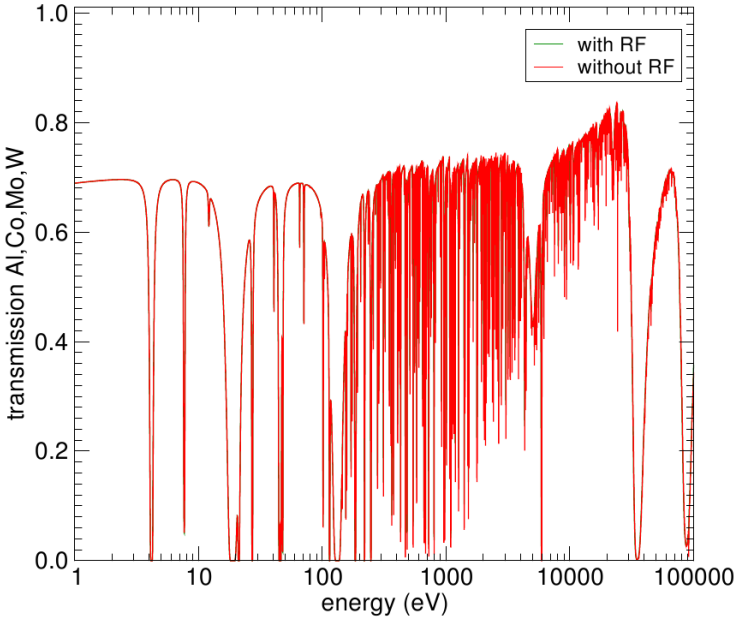

Figure 3.7: Calculated total transmission of neutrons for the Al, Co, Mo and W filters in the neutron beam. The green line takes into account the Resolution Function (RF) of the n_TOF spectrometer and is hidden behind the red line. Courtesy of F. Gunsing.

3.3.4 Yield normalization

The measured capture yield depends on the fraction of the neutron beam impinging on the sample. Therefore, it is convenient to normalize the measured yield to the yield of an isotope with a well known cross section. In this work, the saturated resonance technique was used. It implies the measurement of e.g. a Au sample, having the same size as the sample of interest. The Au cross section has a resonance at E_R=4.9 eV with a very high capture cross-section value while the elastic scattering cross section is much smaller (Γ_γ = 121.4 eV and Γ_n = 14.96 eV [57]). From a sample thickness of a few μm all neutrons with or close to the resonance energy are absorbed in the sample (the resonance is saturated). The capture yield is close to 1, since even if a neutron is scattered, it is captured afterwards before escaping the sample. The normalization is determined by fitting the plateau of the saturated resonance with fixed resonance parameters, while leaving the normalization free. This technique is very robust since the fit does not strongly depend on the resonance parameters.

3.3.5 From capture yield to cross section

In the following, all inelastic channels will be neglected, since they are not relevant for the analysis in this work. In the resolved resonance region, the resonant behaviour of

the cross section can be parametrized using the resonance energy E_R, the partial widths Γ_γ and Γ_n, the total width Γ_{tot} and the resonance spin J.
If the neutron energy resolution of the experimental setup is sufficiently good, all resonance parameters can be determined by combining capture and transmission experiments, the latter measuring the total cross section. For most resonances however, the experimental resolution is larger than the natural width of the resonance. This means that only the area of the resonance can be extracted. The area of a capture resonance is

$$A_\gamma = 2\pi^2 n \lambda_0^2 g \frac{\Gamma_n \Gamma_\gamma}{\Gamma} \tag{3.16}$$

Therefore, from one single capture experiment only the capture kernel $k_\gamma = g\frac{\Gamma_n\Gamma_\gamma}{\Gamma}$ can be extracted. If $\Gamma_n >> \Gamma_\gamma$ or vice versa, $g\Gamma_\gamma$ and $g\Gamma_n$ respectively can be determined and if the spin of the resonance is already known, also the respective partial width. If $\Gamma_\gamma << \Gamma_n$ all resonance parameters can be extracted in combination with transmission measurements of a thin ($n\sigma_{E=E_R} << 1$) and a thick ($n\sigma_{E=E_R} >> 1$) sample.
Experimental effects which need to be considered are multiple scattering and self-shielding. Multiple scattering only concerns capture data. The experimental yield is therefore enhanced and can be written as a sum $Y_{tot} = Y_0 + Y_1 + ...$, where Y_0 denotes the yield where the capture is the first interaction in the sample, Y_1 is the yield after one scatter and so on. Multiple scattering enhances the capture yield in the high energy tail of the resonance, since neutrons lose energy by the scattering process to a value that matches the resonance energy. Self shielding is the loss of neutrons in the sample due to all other reactions. Since the number of neutrons crossing the sample decreases, the measured capture yield is reduced as a consequence of the self shielding.
In this work, the resolved resonance region was analyzed using the code SAMMY [53], which is based on the R-Matrix parametrization. For extracting resonance parameters the Reich-Moore approximation was applied. SAMMY implements multiple scattering and self shielding corrections, as well as resolution effects when fitting the resonance parameters. In the unresolved resonance region the Monte Carlo code SESH [58], based on the statistical properties of resonances, was used to calculate multiple scattering and self-shielding corrections. After such a correction the cross section can be determined via

$$\sigma_{n\gamma} = Y_{n\gamma}/n \tag{3.17}$$

3.4 Complementary techniques: activation

The activation technique provides a complementary tool to measure reaction cross sections. The sample of element X, with a mass A is irradiated with neutrons, afterwards the reaction product ^{A+1}X is counted. This technique can be only applied to radioactive products, which are quantified e.g. by decay counting or, if the reaction product is long

lived, by direct atom counting techniques, e.g. Accelerator Mass Spectrometry (AMS). Since there is no information on the count rate as function of neutron energy, the cross section obtained is averaged over the neutron spectrum. This requires a monoenergetic neutron beam or a neutron spectrum which is already suited for the respective application. For measuring stellar cross sections, several nuclear reactions with such properties have been identified, particularly the $^{7}\mathrm{Li}(p,n)^{7}\mathrm{Be}$ reaction. When choosing a proton energy of 1912 keV, which is slightly above the reaction threshold of 1881 keV, the neutron spectrum emitted shows an energy behaviour similar to

$$\phi(E_n) \propto E_n \times e^{-E_n/k_BT} \tag{3.18}$$

around $k_BT = 25$ keV, perfectly suited for measuring MACSs (see equation 2.18). Such a spectrum will be discussed in detail in Chapter 6. The fact that the proton energy is

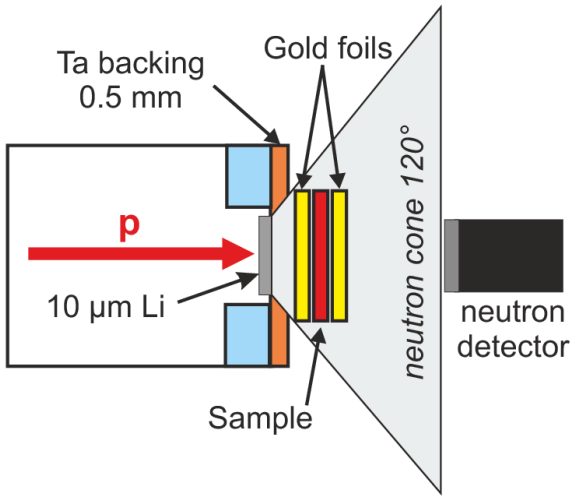

Figure 3.8: Sketch of the experimental setup used in activation experiments. The sample of interest is sandwiched between two Au foils which serve as neutron fluence monitor. A neutron detector monitors the time dependence of the neutron flux. Courtesy of I. Dillmann.

chosen only 31 keV above the threshold of the reaction results in a neutron spectrum which is emitted in a forward peaked cone with an opening angle of 120°. This means that it is possible to expose the sample to the full quasi-stellar spectrum by placing it directly in front of the neutron producing Li-target. A number of MACS measurements have been performed in this way [17, 59]. The neutron fluence was determined by normalizing to the $^{197}\mathrm{Au}(n,\gamma)$ cross section measured with an uncertainty of 1.5% [34]. A sketch of the experimental setup used for such experiments is shown in Fig. 3.8.
Besides some limitations mentioned above, there are several advantages compared to time-of-flight measurements. Samples can be put close to the neutron source, which enhances the flux and allows measurement of small sample masses and small cross

sections. There is no background from impurities, therefore samples with natural composition can be used. The use of smaller sample masses also makes corrections for multiple scattering and self-shielding effects less crucial. Contrary to resonance analysis of time-of-flight data, the direct capture component is included in those measurements. On the other hand, the energy dependence of the cross section needs to be known, since the spectrum averaged cross section needs to be corrected for differences between the laboratory spectrum and the spectrum of Eq. 3.18. This information can only be gained from time-of-flight experiments.

4 Measurement of the ^{62,63}Ni(n, γ) cross section at n_TOF

4.1 Introduction

The measurement of the ^{62}Ni(n, γ) cross section at n_TOF was performed in the framework of a measurement campaign [60], which aims at measuring the neutron capture cross sections of all stable Fe and Ni isotopes over a wide energy range from eV to several hundred keV. The measurement was motivated by observations of Sneden *et al.*, who investigated the abundances of Ultra-metal poor stars (UMPs) [61, 62, 63]. Sneden *et al.* found that the abundances scale very well with expected *r* process abundances for elements heavier than Ba, which was interpreted as indication for a primary, robust *r* process. For lower masses however, a systematic offset was observed (see fig. 4.1).

In order to compare observed elemental abundances to predicted *r* abundances, the *r* process component is calculated by subtracting the *s* component from the solar abundance distribution. Therefore, the accuracy of the *r* abundance distribution depends strongly on the accuracy of the calculated *s* component. As already described in Section 1.4.1, elements between masses $60 < A < 90$ are dominantly produced by the weak *s* component, where neutron exposures are too low to reach reaction flow equilibrium. Accordingly, single erroneous cross sections also affect the abundances of a number of successive isotopes in the reaction chain. This was first noted by Rauscher *et al.* [64] followed by (n, γ) measurements of Nassar *et al.* for the case of ^{62}Ni(n, γ) [65]. In Figure 4.2 the calculated elemental abundances for MACS values at $k_BT = 30$ keV of 26.1 mb [65] and 35 mb [66] relative to 12.5 mb [17] is shown, demonstrating that changes as large as 40% in the abundances up to mass 90 are to be expected.

In Table 4.1 some experimental and theoretical values of the ^{62}Ni(n, γ) MACS at $k_BT = 30$ keV are listed. For all of those values which range from 9.7 mb to 37 mb, the quoted uncertainties are at least 10%. The currently recommended value by the most recent compilation KADoNis [67, 68] is 22.3 ± 1.6 mb and corresponds to a weighted average based on results of [65, 69, 70, 71], where for [65] a different energy dependence of the cross section was assumed for extrapolating from the measured MACS at 25 keV to the MACS at 30 keV. This situation underlines the need for new experimental data to reduce the present uncertainties in the MACSs, as well as the need to get more information on the energy dependence of the cross section on which previous extrapo-

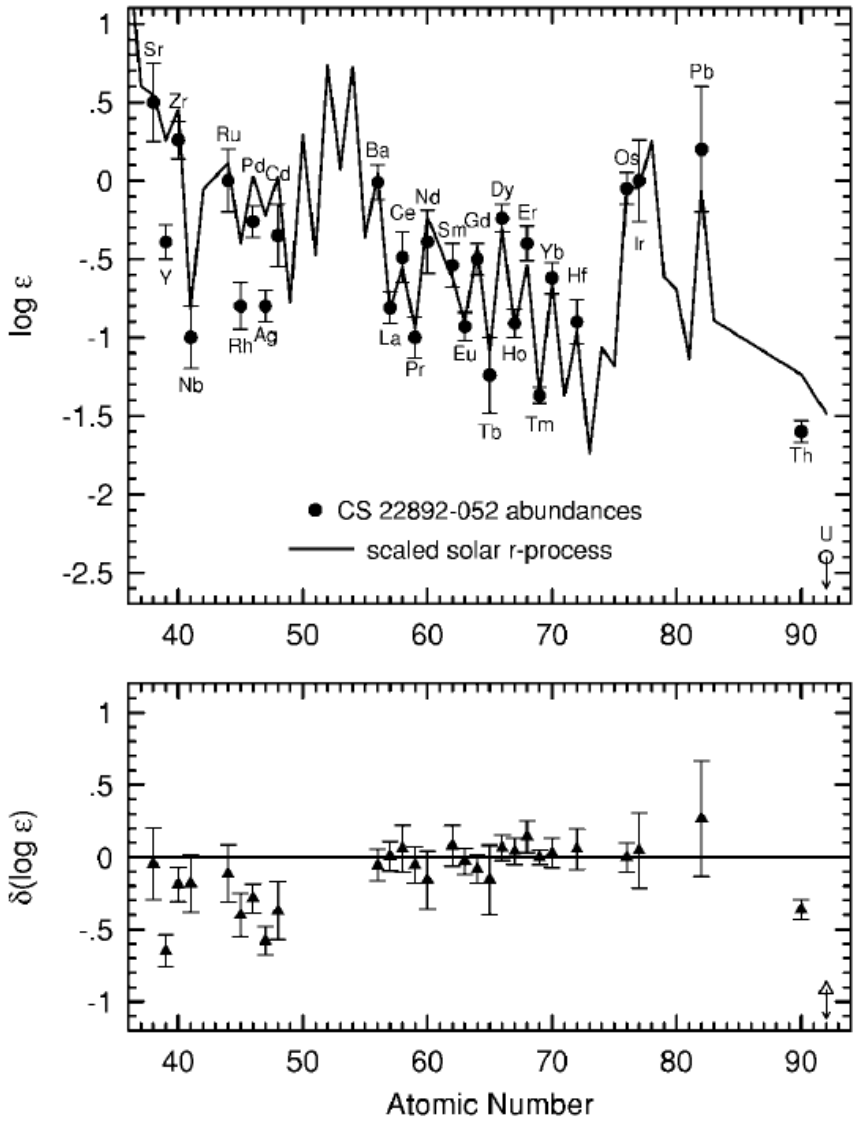

Figure 4.1: Measured elemental abundances of the ultra metal poor star CS 22892-052 scaled to expected solar system *r* abundances investigated by Sneden *et al.* [62]. The bottom figure shows the deviations of the solar system curve compared to the measured abundance. Figure 2 in Reference [62].

lations of MACS rely.

The production of the *s* process isotope ^{63}Ni with a terrestrial half life of $t_{1/2}$ = 101.1 ± 1.4 y [75], is attributed to the weak component and represents the first branching point in the *s* process path. The weak component takes place during two stages

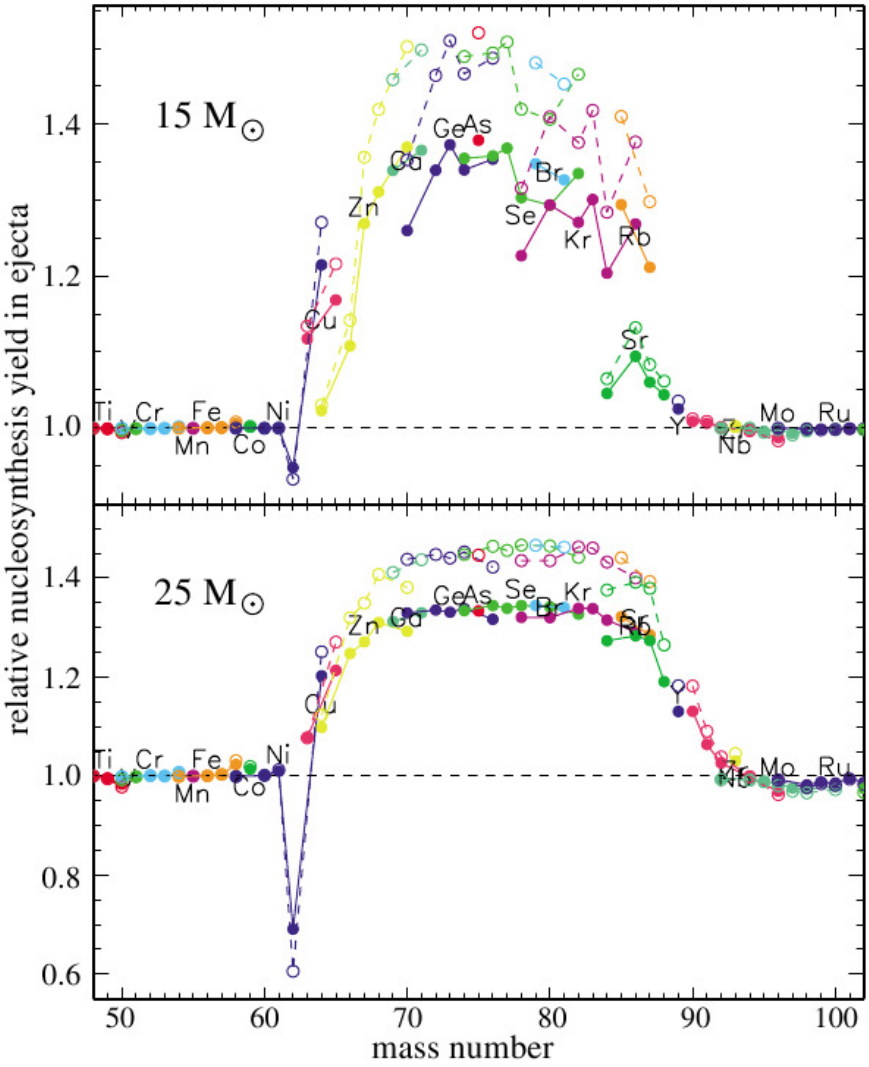

Figure 4.2: Predicted elemental abundances for two different values of the ^{62}Ni(n,γ) MACSs at k_BT = 30 keV (filled circles 26.1 mb, and empty circles 35 mb, respectively) relative to a MACS of 12.5 mb. Figure taken from Reference [65].

of massive star evolution: first at the end of He core burning at temperatures corresponding to k_BT = 25 keV and subsequently during C shell burning at k_BT = 90 keV. Neutrons are produced via the ^{22}Ne(α,n) reaction, where ^{22}Ne is produced by subsequent α captures on the CNO isotope ^{14}N according to reaction sequence 1.8 in Section 1.4.1. Figure 4.3 shows the *s* process path in the Ni/Cu region for those two different phases.

During He core burning, neutron densities are around $N_n = 10^6$ cm^{-3} and not high

Table 4.1: Calculated and measured values for the $^{62}Ni(n,\gamma)$ MACS at k_BT = 30 keV.

Cross section (mb)	Method	Author	Year
26.8 ± 5.0	time-of-flight	Beer and Spencer [69]	1975
37.0 ± 3.2	time-of-flight	Tomyo *et al.*[72]	2005
25.8 ± 3.7	time-of-flight	Alpizar-Vicente *et al.*[70]	2008
26.1 ± 2.6*	activation	Nassar *et al.*[65]	2005
23.4 ± 4.6	activation	Dillmann *et al.*[71]	2010
9.7 – 11.2	calculation	Rauscher and Guber [73, 74]	2002
35.5 ± 4.0	compilation	Bao and Käppeler [66]	1987
12.5 ± 4.0	compilation	Bao *et al.*[17]	2000
22.3 ± 1.6	compilation	KADoNis [67, 68]	2009

* extrapolation from 25 keV.

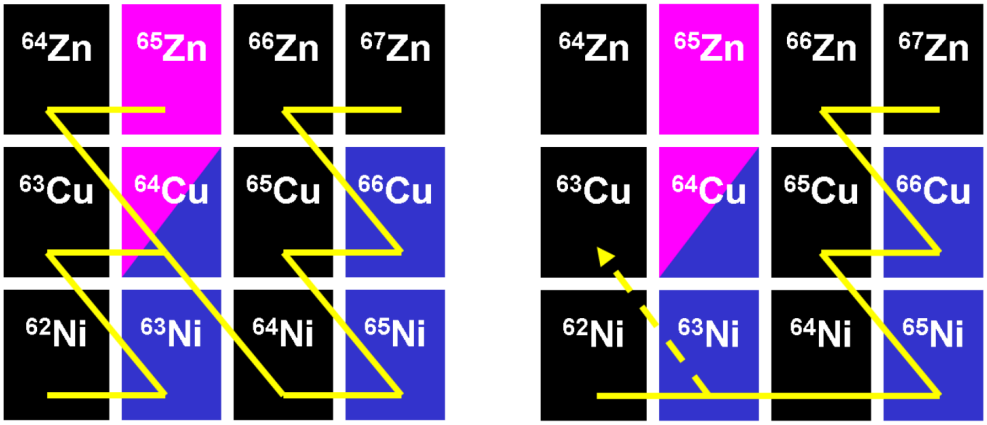

Figure 4.3: Path of the s process for He core burning (left) and C shell burning (right).

enough to bypass the decay of ^{63}Ni by subsequent neutron capture. The branching ratio is therefore close to one ($f_b \approx 0.91$ [76]). This situation changes completely during the subsequent C shell burning. Despite the drastically diminished half life of ^{63}Ni at around 1 GK stellar temperature, neutron densities are 5-6 orders of magnitudes larger, allowing ^{63}Ni to act almost as a stable isotope with $f_b \approx 0.02$ [76]. ^{63}Cu is produced only at the end of C shell burning due to radioactive decay of the present ^{63}Ni.
Pignatari *et al.* calculated weak *s* abundances for a pop. I star[1] with a mass of 25 $M_\odot$, varying the initial abundance distribution and neutron capture cross sections [77]. Since ^{63}Cu is depleted during He core burning due to its comparably large capture cross section, almost all ^{63}Cu produced in the weak *s* process can be attributed to radioactive decay of ^{63}Ni after C shell burning. Pignatari *et al.* found that the neutron capture cross

[1] Stars of population I are metal-rich, therefore young stars (e.g. our sun).

section of ^{63}Ni has a severe impact on the total ^{63}Cu abundance, because 70-80% are produced in the weak *s* process (the rest can be explained by explosive nucleosynthesis and the main *s* component). Starting from solar system abundances, the final Cu abundances would change by about 20% when altering the ^{63}Ni MACS by a factor of 2 [77]. The only experimental data available for the ^{63}Ni(n,γ) cross section are at thermal neutron energies [78, 79, 80]. Therefore, the stellar cross section relies on extrapolation of the thermal value, or on calculations. We proposed to measure this cross section at the n_TOF facility in 2010 [81]. The measurement was finished in spring 2011 and first results are reported here. This reaction has also been investigated at the time-of-flight facility LANL at *Los Alamos National Laboratory*, but data are not yet available [82].

4.2 Measurement

At n_TOF, the amount of beam time designated to a measurement is counted as protons on the spallation target. During one year, n_TOF receives on average 1.4×10^{19} protons. For the ^{62}Ni(n,γ) measurement 2×10^{18} protons were scheduled [60]. The number of protons required was estimated by calculating count rates based on available cross section data. In the case of ^{63}Ni(n,γ) no experimental data were available and the cross section values of the energy region from 1 eV to 1 MeV had to be calculated. The amount of beam time proposed for this experiment was 5×10^{18} protons in order to obtain reasonable statistics since the sample mass of this radionuclide ($\approx 10^{19}$ ^{63}Ni atoms) was much smaller compared to the ^{62}Ni sample [81]. The experimental setup was as described in Section 3.2.1, except that in 2011 one of the optimized C_6D_6 detectors ("FZK-detector") had to be replaced with a commercial detector manufactured by Bicron, which has also been optimized in some points ("BICRON-detector") (see Reference [40] for more information). The samples which were used for both measurement campaigns as well as their properties are listed in Table 4.2. A more detailed description of the ^{62}Ni and the ^{63}Ni sample can be found in Appendix A.
Besides the samples of interest ^{62}Ni and ^{63}Ni, Au was measured for normalizing the capture yield. Additionally, runs without any sample and with neutron filters in the beam were performed to study the background, and measurements without neutron beam were done to measure the ambient background. Although the measurement of ^{62}Ni(n,γ) was already performed in 2009, we decided to re-measure this reaction for background studies in the ^{63}Ni(n,γ) campaign. In contrast to the first ^{62}Ni campaign, a water moderator with boron was used for the ^{63}Ni(n,γ) measurement. This means a significant reduction of background in the keV region, providing the possibility to detect new ^{62}Ni resonances which were covered by background before.

Calibration runs were done in intervals of one week to check the stability of the detector gains of the C_6D_6 detectors. The lower hardware thresholds of the detectors were around 150 keV for the ^{62}Ni(n,γ) campaign and around 200 keV for the ^{63}Ni(n,γ)

Table 4.2: Samples used for the ^{62}Ni and ^{63}Ni measurement at n_TOF. All samples were of cylindrical shape. The thickness is given in atoms per barn.

Sample	Enrichment (at%)	Mass (mg)	∅(mm)	Thickness (b^{-1})	Chemical Form
^{62}Ni	97.95	1989	19.93	(6.203×10^{-3})	metallic
^{63}Ni	≈5.7	1156	20.00	$(3.25 \times 10^{-4})^*$	oxide powder
^{197}Au	100	596	19.94	(5.838×10^{-4})	metallic
C	natural	5285	19.98	(8.455×10^{-2})	graphite
Pb	natural	313	19.90	(2.930×10^{-4})	metallic

* Value given for the number of ^{63}Ni atoms per barn. The number of ^{63}Ni atoms was calculated from the information given in Appendix A.

campaign. The reason for that difference is that in the latter measurement the gain had to be lowered to access γ energies at the neutron separation energy of ^{64}Ni, which is S_n = 9.66 MeV and about 3 MeV higher than the neutron separation energy of ^{63}Ni with S_n = 6.84 MeV.

4.3 Data analysis

4.3.1 Dead-time correction and coincidence rejection

The raw data are corrected for dead-time effects by putting a veto on the time of two consecutive events. This results in a well defined, fixed dead-time τ_d which can be corrected using the relation

$$C' = \frac{C}{1 - C\tau_d} \tag{4.1}$$

where C' is the true and C is the measured count rate. This correction is valid for paralyzable as well as non-paralyzable systems if the corrections are small (see for example Reference [83], Chapter 4.VII), which is the case for the C_6D_6 system. The best value for τ_d can be chosen by plotting a count rate histogram as a function of the time between two consecutive events ΔTOF for each detector. Such a plot is shown in Figure 4.4. The dead-time can then be estimated by the time, when the distribution falls off sharply, indicating a loss of counts due to the system dead-time. In the analysis a value of τ_d = 30 ns was chosen.

At n_TOF, neutron pulses of two different intensities are available which need to be corrected separately. A correction is applied to the sum of all dedicated and parasitic

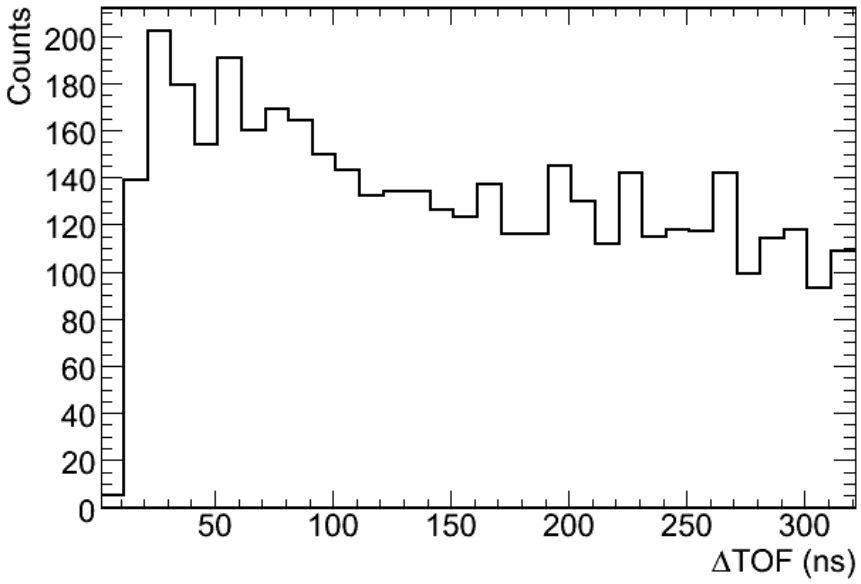

Figure 4.4: The time between two consecutive events for one of the C_6D_6 detectors for one run. The spectrum shows a sharp decrease at very small ΔTOFs which indicates the loss of counts due to system dead-time effects.

pulses, respectively using the relation (which is equivalent to equation 4.1):

$$C' = \frac{C}{1 - 1/\mathcal{B} \int_{t'-\tau_d}^{t'} C dt'} \tag{4.2}$$

$\mathcal{B}$ is the number of proton bunches of the respective pulse type. The dead-time corrections for the data were ≤1% for the 4.9-eV resonance in Au which is used for normalization. For the Ni spectra, the dead-time corrections were less than 1% throughout the entire neutron energy range.

For the time between two consecutive events in different detectors, the opposite effect is observed as shown in Fig. 4.6. The smaller ΔTOF, the higher the number of counts. This is due to coincident events, e.g. if two γ rays of the same cascade are counted in different detectors. By putting a veto of 30 ns, the coincidences are automatically rejected. Coincident events contributed about 4.3% (Ni) and 4.8% (Au) of the total number of counts.

A similar effect is the coincident detection of γ events in the same detector (γ summing). Instead of detecting an event with deposited energy E_{dep1}, the detector measures the sum of the two, $E_{\text{dep1}} + E_{\text{dep2}}$, which leads to an overestimation of the weighted

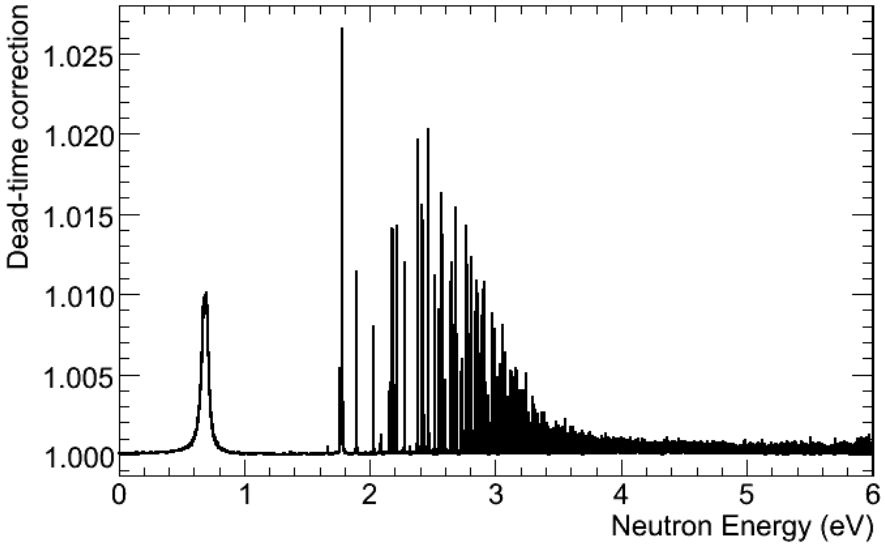

Figure 4.5: Dead-time correction applied to the Au data for the ^{62}Ni campaign.

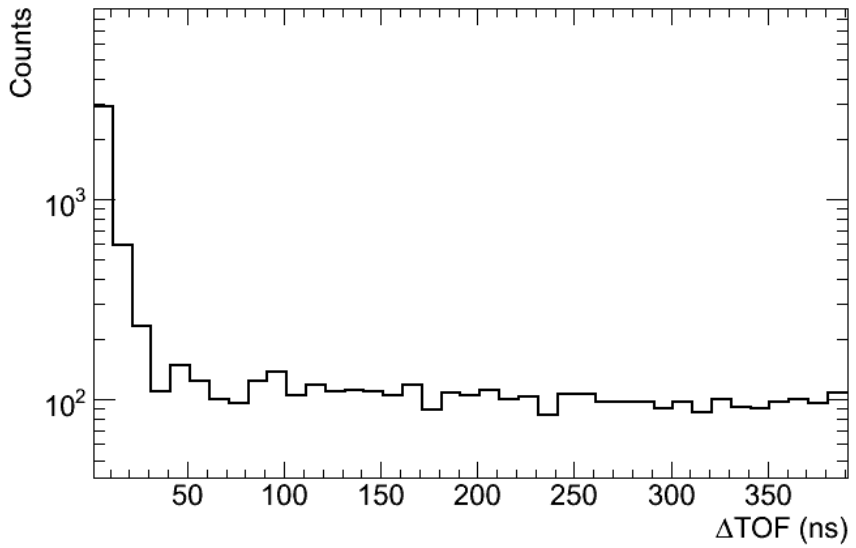

Figure 4.6: Time between two consecutive events in different detectors. The rise of the signal towards smaller ΔTOFs indicates coincident events.

counts for coincident events in all samples. The size of this effect was estimated by ap-

plying weighting functions to the coincident events observed in different detectors. The weighted first events $\sum W(E_{\mathrm{dep1}})$ were counted and compared to the weighted events of the sum of both energies $\sum W(E_{\mathrm{dep1}} + E_{\mathrm{dep2}})$. This approximation gives an upper limit for that correction since in reality, the detector response for two simultaneous γ rays does not equal the detector response for one γ ray with the summed energy (see e.g. [55]). Since the Ni yield is scaled relative to Au this effect essentially cancels and was in the present case only 0.3%.

4.3.2 Detector calibration

C_6D_6 detectors have a fairly low efficiency for full energy detection. The majority of the energy deposited is originating from Compton interactions. The detectors were calibrated in separate runs using a set of radioactive sources:

- ^{137}Cs, emitting a γ ray with an energy of 662 keV
- ^{88}Y, emitting two γ rays in coincidence with energies of 898 keV and 1.836 MeV
- AmBe, producing a γ ray of 4.44 MeV energy via the intrinsic $^{9}\mathrm{Be}(\alpha, n)^{12}\mathrm{C}$ reaction

The detectors are calibrated by comparing the measured spectra to simulations of the detector response. For this purpose, the codes GEANT3 and GEANT4 were used. We assumed γ rays of the respective energy are emitted homogeneously in 4π and the deposited energy in the C_6D_6 liquid was simulated. Since these simulations do not take into account any instrumental broadening effect, the simulated data need to be convoluted with the resolution of the detectors which can be approximated by the relation:

$$\sigma^2(\mathrm{MeV}^2) = b_0 E_\gamma + b_1 E_\gamma^2 \tag{4.3}$$

For calibration, the Compton edge in the deposited energy spectrum could be reproduced by a fit with a Gaussian function. As reference points x_{ref} for determining the calibration coefficients the mean value $\overline{x}$ plus half of the FWHM Δx was chosen:

$$x_{\mathrm{ref}} = \overline{x} + \Delta x/2 \tag{4.4}$$

The four calibration points are fitted with a function of the type

$$E_\gamma(\mathrm{MeV}) = c_0 + c_1 \mathrm{Channel} + c_2 \mathrm{Channel}^2 \tag{4.5}$$

since the calibration turned out to be non-linear.
Calibration runs with all three sources were performed in regular intervals to monitor the gain stability of the detectors and, if necessary calculate a time dependent calibration.

Table 4.3: Resolution coefficients for Eq. 4.3 and energy calibration coefficients for Eq. 4.5 for the ^{63}Ni(n,γ) campaign. The detector gain was stable throughout the measurement.

	b_0	b_1	c_0	c_1	c_2
BICRON	7.72×10^{-3}	0.93×10^{-3}	0.059	0.041	-9.778×10^{-6}
FZK	1.10×10^{-3}	0.95×10^{-3}	0.065	0.037	-4.973×10^{-6}

The fact that the highest γ energy available for calibration runs is 4.44 MeV turned out to be a problem for calibrating the detectors for the ^{63}Ni campaign. The neutron separation energy of the compound nucleus ^{64}Ni is 9.66 MeV, which means that a correct calibration up to that energy is crucial. For this reason, the amplitude spectrum of ^{63}Ni itself was additionally used to calibrate the detectors at higher energies. Both isotopes present in the sample ^{62}Ni and ^{63}Ni show strong γ ray transitions from the capture to the ground state [80, 84]. The respective energies are 6.84 MeV for ^{62}Ni(n,γ) and 9.66 MeV for ^{63}Ni(n,γ). The response of these two γ rays was simulated and used as further reference energies for calibration. The resulting calibrated spectra compared to the simulations as shown in Fig. 4.7 are in good agreement. The coefficients obtained for the resolution b_0 and b_1, as well as for the calibration c_0, c_1 and c_2 for the 2011 runs, are listed in Table 4.3. It should be noted that small disagreements from the simulated spectra do not affect the capture cross section, since these effects cancel almost completely when normalizing to Au.

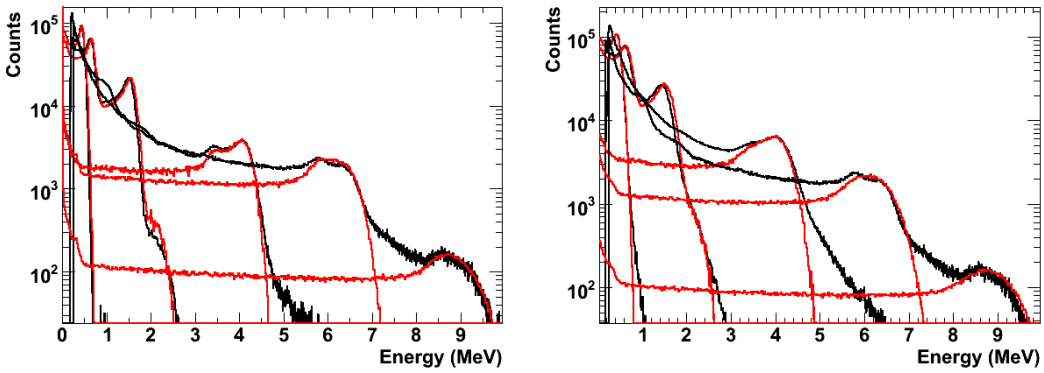

Figure 4.7: Calibrated amplitude spectra of the BICRON (left) and the FZK (right) detector measured with Cs, Y, AmBe sources and the ^{63}Ni sample (black) compared to simulations (red).

4.3.3 Weighting functions

The detector response for the analysis in this work has been simulated using the codes GEANT3 [85] for data taken in 2009 (^{62}Ni campaign) [86] and GEANT4 [87] for 2011 (^{63}Ni campaign). The geometry of the detection setup 2011 [88] as used in the simulations is shown in Figure 4.8.

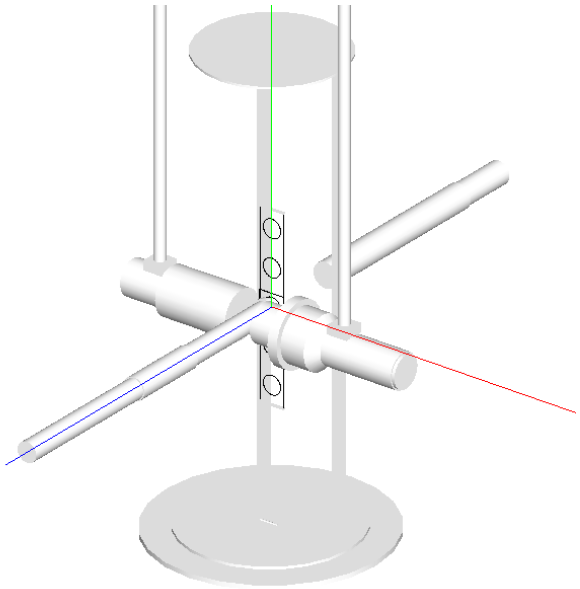

Figure 4.8: Geometry of the C_6D_6 setup for simulating the detector response.

Monoenergetic γ rays were simulated for energies of 200, 300, 500, 700, 800 keV and from 1 to 11 MeV in steps of 1 MeV. Figure 4.9 shows the simulated γ-response spectrum of both C_6D_6 detectors for ^{62}Ni (2011 setup). γ rays were assumed to be emitted throughout the ^{62}Ni sample volume taking into account the neutron beam profile for the radial distribution of primary γ rays. The coefficients of the WF of the form $\sum_{n=0}^{4} a_n E^n$ were fitted to fulfill condition 3.15 in Sec. 3.3.2. The WF parameters of all samples concerning the ^{62}Ni(n,γ) and ^{63}Ni(n,γ) measurements are shown in Table 4.4.
Since in 2011 two different C_6D_6 detectors were used (”BICRON” and ”FZK” detector), two different WFs, one for each detector were applied in the analysis. To the WFs the same threshold was applied as used in the data analysis, which was 200 keV and 250 keV in 2009 and 2011, respectively. Figure 4.10 shows the WF including the residuals for the ^{62}Ni sample (2011 setup). Another possibility is to calculate WFs without threshold and correcting the capture yield for the fraction which is omitted by the analysis threshold as second step.
Weighting functions were calculated for a homogeneous γ ray emission throughout the sample thickness. For high cross sections, this is not a realistic assumption, since neu-

Table 4.4: Coefficients of the WFs of the form $W(E) = \sum_{n=0}^{4} a_n E^n$ for samples used in this analysis. A threshold of 200 keV and 250 keV was applied to the "2009" and "2011" data, respectively.

Sample	a_0	a_1	a_2	a_3	a_4
^{62}Ni (2009)	-3.794	34.429	-1.308	1.235	-0.09287
^{197}Au (2009)	-4.623	35.037	-2.503	1.493	-0.10199
^{62}Ni (2011) BICRON	17.534	-5.510	33.238	-4.802	0.25720
FZK	10.810	-4.182	20.769	-3.005	0.16135
^{63}Ni (2011) BICRON	15.455	0.31185	28.954	-3.823	0.20938
FZK	9.250	0.35335	17.458	-2.302	0.12364
^{197}Au (2011) BICRON	17.470	-5.105	32.698	-4.650	0.25572
FZK	10.614	-3.6336	20.236	-2.890	0.15423

trons can be absorbed already in the first layers of the sample. This is for example the case for the 4.9-eV resonance in Au which is used for normalizing the capture yield. Therefore, WFs were additionally calculated for the Au sample, assuming an exponentially decreasing γ intensity with increasing sample thickness.

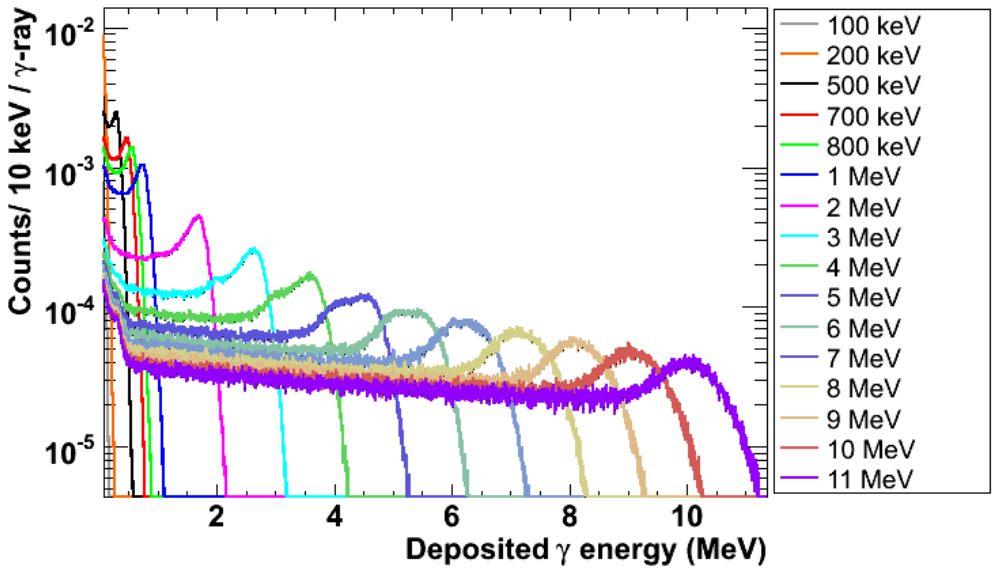

Figure 4.9: Simulated response of the C_6D_6 detection setup for a homogeneous emission of γ-rays from the ^{62}Ni sample. The energy spectrum is already corrected for the detector resolution.

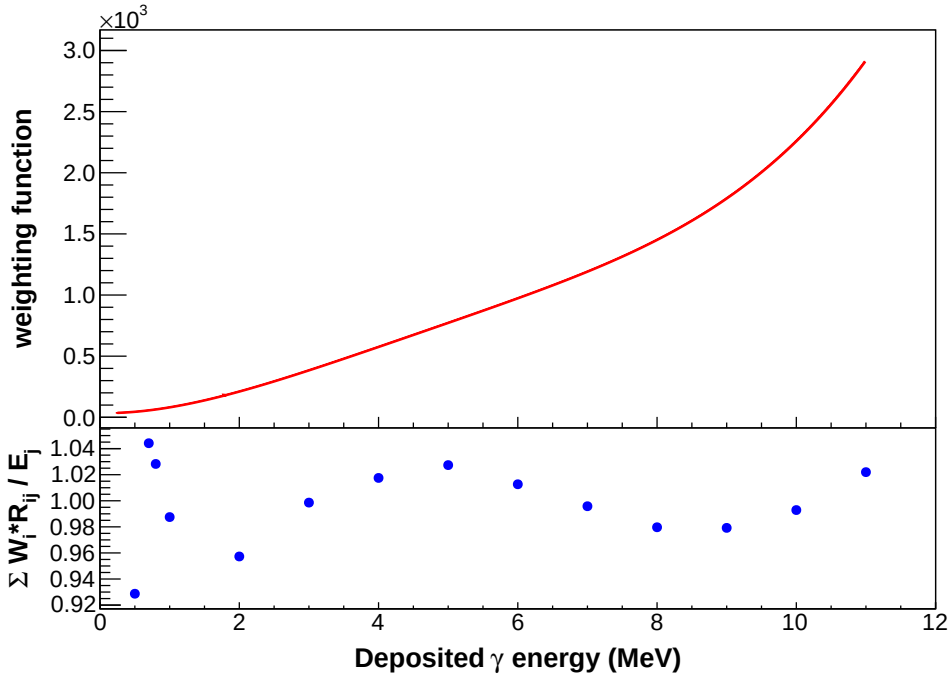

Figure 4.10: Weighting function for ^{62}Ni of the measurement in 2011 (top) and corresponding residuals (bottom). A threshold of 250 keV, as used in the data analysis was applied to the WFs.

4.3.4 Determination of the flight-path length

The flight path was calibrated with respect to resonances in the ^{197}Au(n,γ) cross section at low neutron energies (eV range). These resonance energies were recently measured with high precision at GELINA in Geel [57, 89]. For that measurement the flight path was calibrated relative to a very well known resonance in the ^{238}U cross section with an energy of $E_R = 6.673 \pm 0.001$ eV [90]. The flight path for the two campaigns was determined being $L_{2009} = 186.94 \pm 0.07$ m and $L_{2011} = 184.12 \pm 0.07$ m. The uncertainties of the flight path are obtained from the fit of five resonance energies. The difference in the flight-path lengths is due to a different position of the capture setup in the experimental area.

4.3.5 Background

Ambient background

The ambient background was measured in runs without beam. Due to the radioactivity of the ^{63}Ni sample the ambient background was measured for different positions of the

^{63}Ni sample in the sample holder relative to the neutron beam. This allowed to correct the ambient background for each sample that was measured individually. The runs need to be scaled according to their total acquisition time, which is proportional to the number of trigger signals (bunches) received. The background subtracted spectrum C_{net} can then be obtained via

$$C_{\text{net}} = C - \frac{\mathcal{B}}{\mathcal{B}_{\text{amb}}} C_{\text{amb}} \tag{4.6}$$

where $\mathcal{B}$ and $\mathcal{B}_{\text{amb}}$ are the number of bunches received for both, the sample and ambient measurement, respectively, and C and C_{amb} are the corresponding number of counts per energy bin. Naturally, the relative contribution of the ambient background is expected to be higher for parasitic pulses than for dedicated pulses. This is illustrated in Fig. 4.11 for the ^{63}Ni spectrum which is scaled for the number of protons times the nominal pulse intensity of 7×10^{12} protons per pulse. In this case, the two spectra should lie exactly on top of each other, however, due to the ambient background the parasitic spectrum seems enhanced, specifically at low neutron energies (top panel Fig. 4.11). Indeed, a higher background at low neutron energies is expected, since the bins cover generally longer time-of-flight intervals. Additionally, the scaled ambient background according to Eq. 4.6 for the dedicated and the parasitic pulses is shown. The bottom panel shows the background-subtracted spectrum for both pulse types, and illustrates the very good agreement.

Beam related background

The background produced independently of the sample was measured in runs with an empty sample frame and with an empty PEEK (Polyetheretherketone) canning. The canning had the same dimensions as the PEEK canning that was used for the ^{63}Ni sample (see Appendix A). Additionally in case of ^{63}Ni(n,γ), neutron capture on ^{62}Ni represents the highest background. Figure 4.12 shows the weighted spectra of ^{63}Ni(n,γ) and ^{62}Ni(n,γ) normalized to the number of proton bunches. The spectra are compared to measurements with an empty sample holder and with the empty PEEK canning. The canning introduces only a small additional background. This background can be simply subtracted from the respective spectrum. To estimate the effect of the smooth, sample dependent background, the spectra taken with filters are compared to the respective empty spectrum taken with filters (Fig. 4.13). We used W, Co and Al filters. Within statistical uncertainties the filter dips of the black resonances at 4.2 eV, 18.8 eV and 130 eV respectively, match the level of the spectrum taken with only the canning or the empty sample holder. Therefore, only a very small contribution of sample dependent smooth background is expected. The resonance dip of Al at 34 keV vanishes in the overall background.

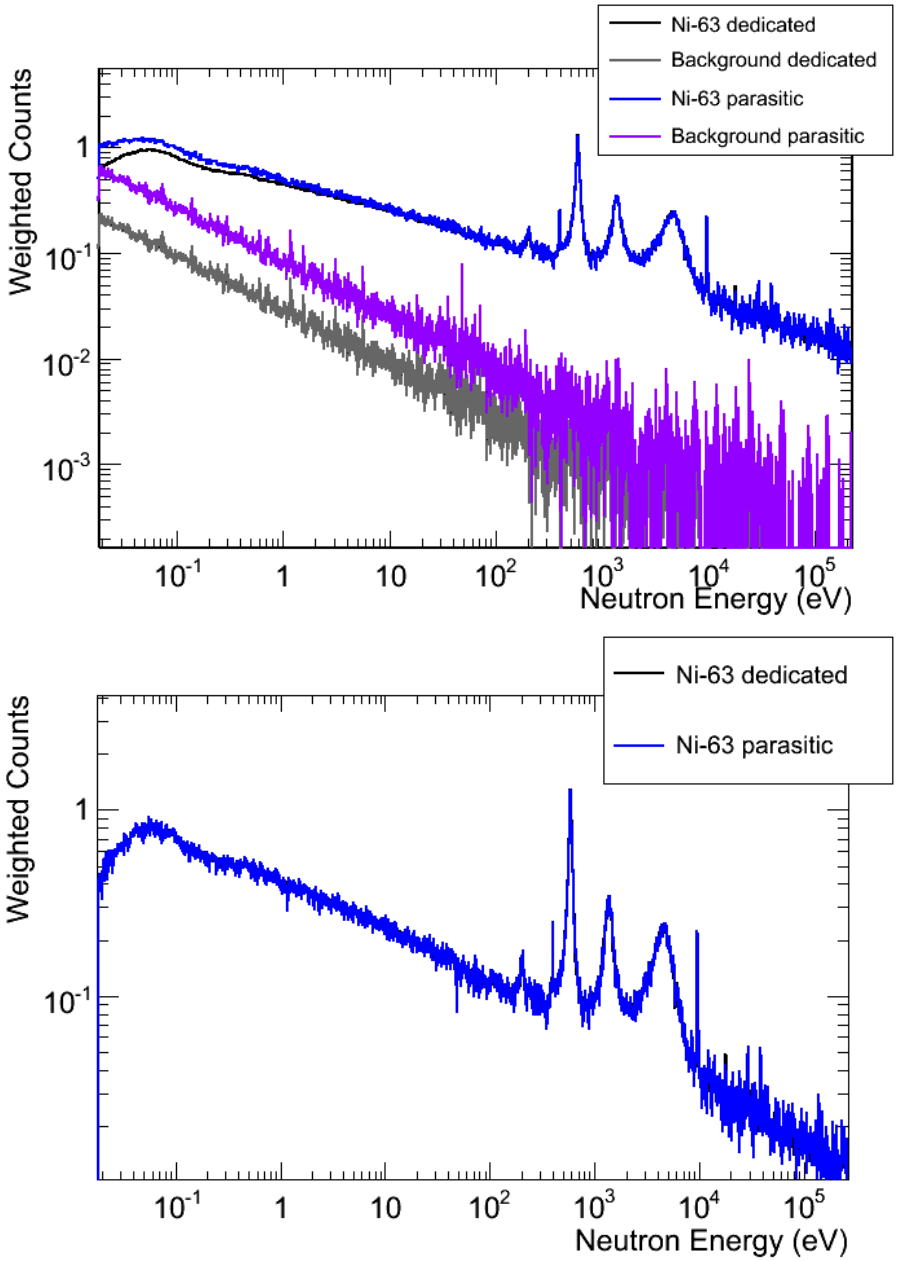

Figure 4.11: (top) Normalized spectrum of ^{63}Ni for the two different proton pulse intensities (black and blue). The measured ambient background has been scaled according to the total acquisition time for dedicated and parasitic runs (grey and purple). (bottom) After subtraction of the ambient background the spectra with different pulse types were found in very good agreement.

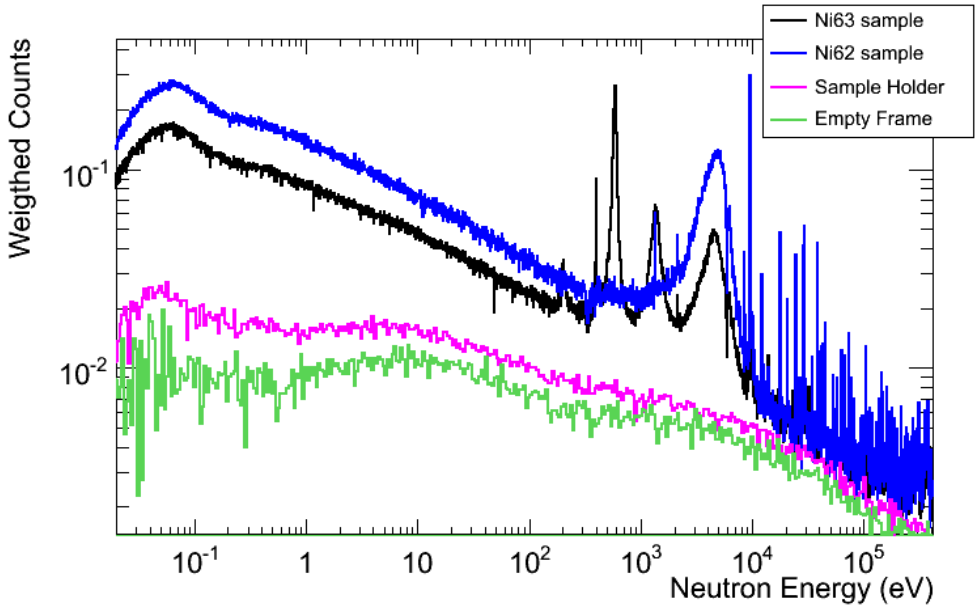

Figure 4.12: Weighted count spectra of ^{63}Ni(n,γ) and ^{62}Ni(n,γ) compared to the backgrounds due to the empty sample frame and the empty PEEK canning.

4.3.6 Yield and normalization

The normalized spectra are transformed to the capture yield via

$$Y_{n\gamma} = \frac{1}{\mathcal{A}} \frac{C_\mathrm{w}}{E_c \phi} \tag{4.7}$$

which is analogous to Eq. 3.4 in Section 3.3. C_w are the weighted counts already corrected for background per proton pulse, E_c is the excitation energy of the compound nucleus, ϕ is the neutron flux per proton pulse and $\mathcal{A}$ is the fraction of the sample that intercepts the neutron beam. Corrections for multiple scattering and self-shielding are not given explicitly since they are taken into account in the resonance analysis. $\mathcal{A}$ was determined by fitting the plateau of the 4.9-eV resonance in Au with the code SAMMY [53]. The fit was performed with the resonance parameters recently published by Massimi *et al.* [57] (E_R = 4.8995 ± 0.0002 eV[2], Γ_n = 14.96 ± 0.02 eV and Γ_γ = 121.4 ± 0.3 eV). The normalization $\mathcal{A}$ obtained from the fit was $\mathcal{A}_{2009}$ = 0.661 ± 0.002 for the ^{62}Ni(n,γ) campaign and $\mathcal{A}_{2011}$ = 0.618 ± 0.002 for the ^{63}Ni(n,γ) campaign. The effect of a different WF due to inhomogeneous γ emission in the 4.9-eV resonance from the sample was only 0.3%. Figure 4.14 shows a compar-

[2]The uncertainty given here is the published uncertainty derived from the resonance shape analysis. Since the neutron energy was calibrated relative to a resonance in ^{238}U with an uncertainty of 0.015% the total uncertainty of the resonance energy is E_R = 4.8995 ± 0.0008 eV.

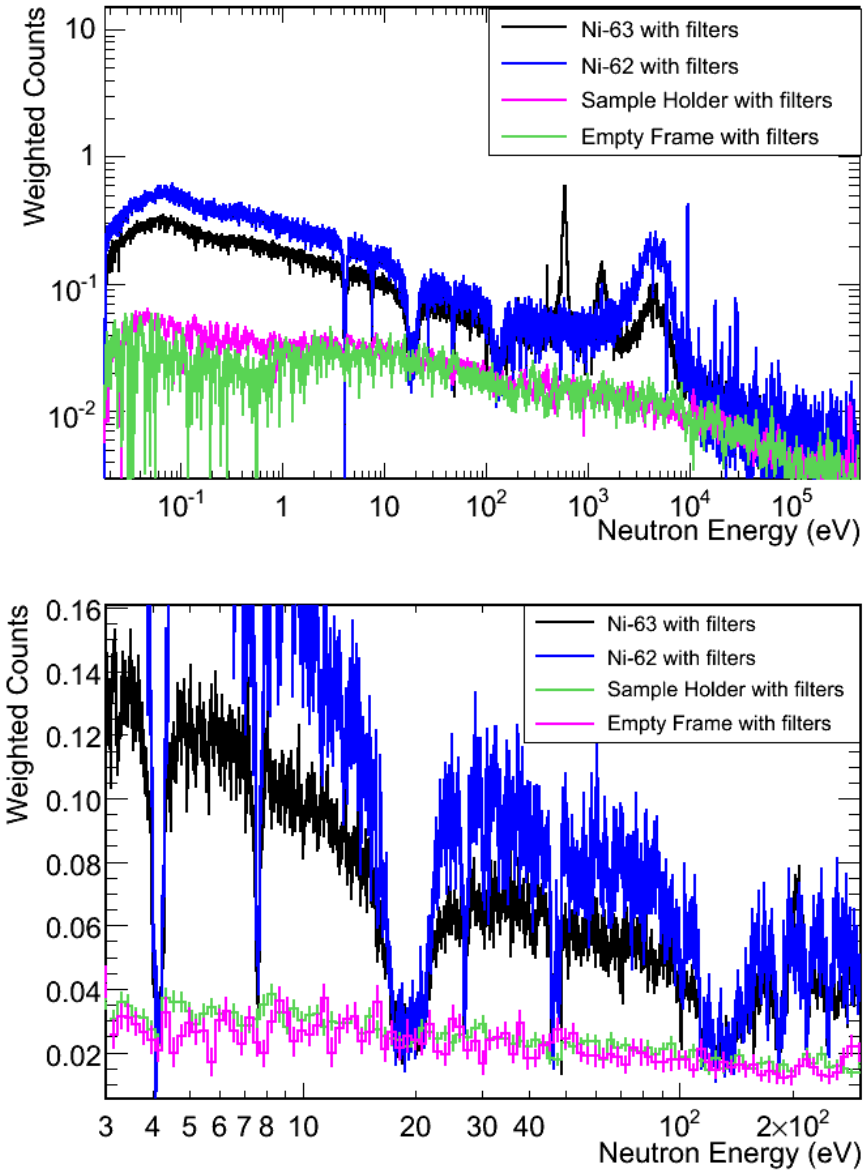

Figure 4.13: (top) Weighted count spectra for ^{63}Ni and ^{62}Ni with filters in the beam compared to the canning and the empty frame measured with filters. (bottom) Zoom into the energy region from 3 to 300 eV. No sample-dependent background can be observed, since the filter dips of the black resonances are at the same level as the empty spectrum and the canning. The spectra are normalized to the total number of neutrons obtained from SiMon.

ison of the data with the calculated capture yield.
The energy dependence of the beam-interception factor was calculated using the sim-

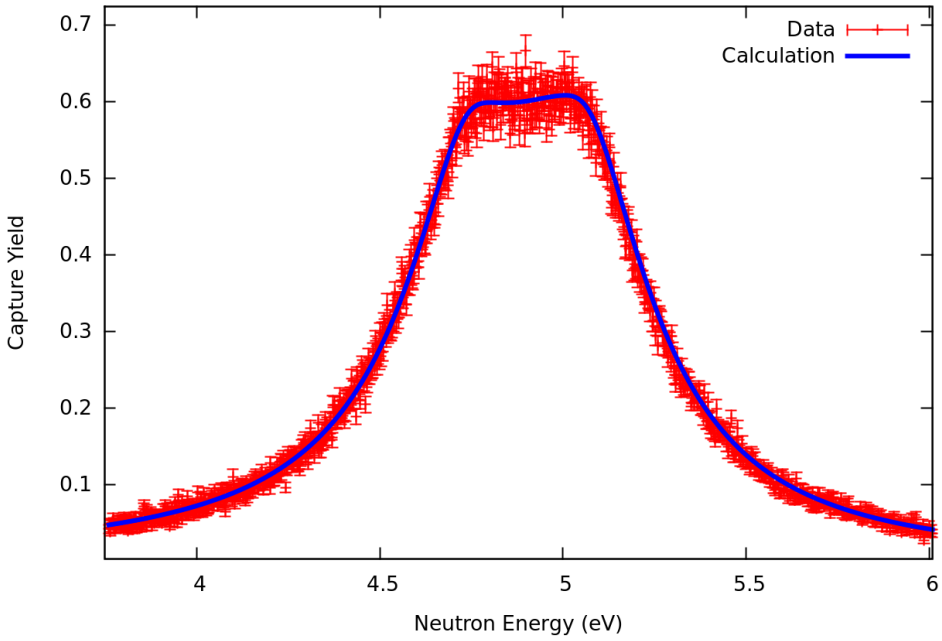

Figure 4.14: A SAMMY calculation of the 4.9-eV resonance for the sample used is compared to the experimental data. The plateau as well as the wings of the resonance are correctly reproduced

ulated neutron beam profile [91]. The correction that was applied to the data relative to the 4.9-eV resonance of Au is shown in Fig. 4.15 for both campaigns. Corrections for this energy dependence are below 2% for most neutron energies. Larger corrections are necessary for thermal neutron energies and for neutron energies above few hundred keV.

4.4 Results

4.4.1 Previous measurements

Few experimental data on the ^{62}Ni(n,γ) reaction in the keV neutron energy region are available as a function of energy. There are two datasets of measurements with the time-of-flight technique [70, 72], apart from that there are some measurements of neutron resonance parameters [69, 92, 93, 94, 95]. Fig. 4.16 shows a comparison of three recent evaluated cross sections [96, 97, 98] with experimental data [70, 72], including some cross section results at thermal neutron energies [79, 84, 99, 100]. The thermal cross sections vary by about 12% from 14.2 b to 15.9 b for the different datasets. The evaluations show some discrepancies already at low neutron energies, ENDF/B-VII.1 [96] and

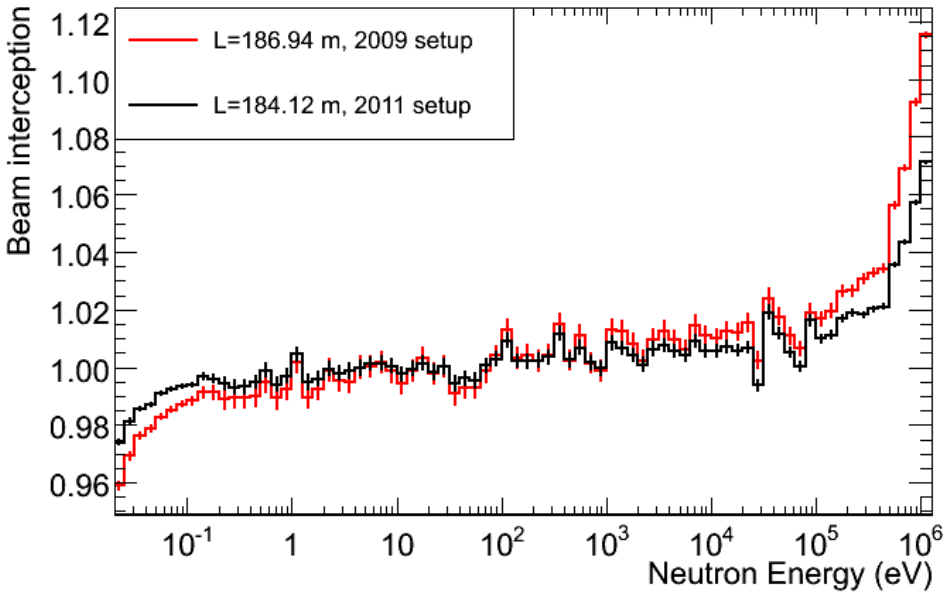

Figure 4.15: Beam-interception factor (BIF) for the two Ni campaigns as a function of neutron energy relative to the 4.9-eV resonance in Au for a sample of 2 cm diameter. The beam interception is constant within ±2% for most of the energy range. Larger corrections are necessary at thermal neutron energies (E_n = 0.0253 eV) and from few hundred keV. The uncertainties shown are statistical.

JENDL-4.0 [97] match the experimental data by Alpizar-Vicente *et al.* [70] rather well, whereas the JEFF-3.1 [98] evaluation seems to underestimate the cross-section value at the first prominent resonance around 4.6 keV. The prediction of a sub-threshold resonance makes the data match the thermal cross section around 14 b. ENDF/B-VII.1 and JEFF-3.1 use the recommended resonance parameters by Mughabghab [101], however, ENDF/B-VII.1 updated resonance parameters according to newer experimental results, e.g. by Alpizar-Vicente *et al.* JENDL-4.0 uses resonance parameters from Ref. [69, 102], which are also listed in Ref. [101]. The data of Alpizar-Vicente *et al.* [70] are normalized to the thermal cross section of Ref. [99] (14.2 ± 0.3 b). The averaged cross section given by Tomyo *et al.* [72] seems to be systematically higher, which is also reflected in the MACS at 30 keV (see Table 4.1 in Sec. 4.1).

Three measurements were performed of the thermal cross-section value of ^{63}Ni(n,γ) [78, 79, 80]. The results are shown in Table 4.5. Values are ranging from 20 b to 26 b and uncertainties are between 12% and 25%. The measurements were normalized to the thermal cross sections of ^{62}Ni(n,γ) [78, 80] or of ^{64}Ni(n,γ) [79].

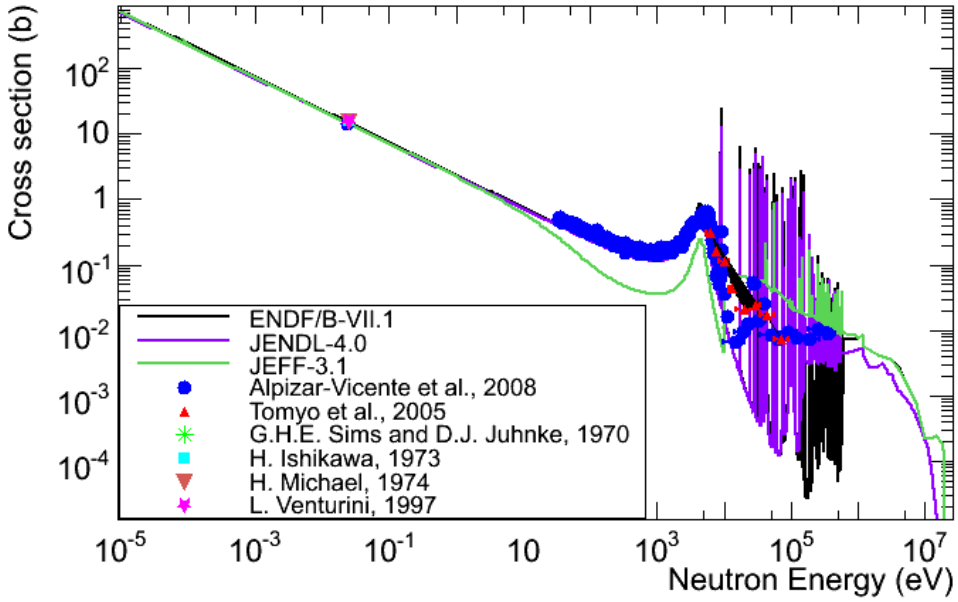

Figure 4.16: Comparison of experimental cross section data on $^{62}Ni(n,\gamma)$ with evaluations. There is a fairly good agreement between the time-of-flight data of Alpizar-Vicente *et al.* [70] with the evaluations ENDF/B-VII.1 [96] and JENDL-4.0 [97]. The JEFF-3.1 [98] evaluation is systematically lower in cross section.

Table 4.5: Experimental thermal cross section values for the reaction $^{63}Ni(n,\gamma)$.

Cross section (mb)	Author
23.0 ± 3.0	I.L. Barnes *et al.*, 1971 [78]
25.7 ± 3.0	H. Michael *et al.*, 1974 [79]
20^{+5}_{-2}	A. Harder *et al.*, 1992 [80]

4.4.2 n_TOF results

The capture yield of the ^{62}Ni and the ^{63}Ni sample was calculated as described in Section 4.3. The measured background due to the empty sample frame and to the PEEK container, have been subtracted from the data. Fig. 4.17 shows a comparison of the $^{62}Ni(n,\gamma)$ yield from thermal to 200 keV obtained from the campaign in 2011. The data are compared to the capture yield calculated from the resonance parameters of the JENDL-4.0 library with SAMMY. The yield has been calculated for the sample including all other Ni isotopes present in the sample (blue) and for the assumption of a pure ^{62}Ni sample (black). As illustrated in the first panel, there is good agreement between

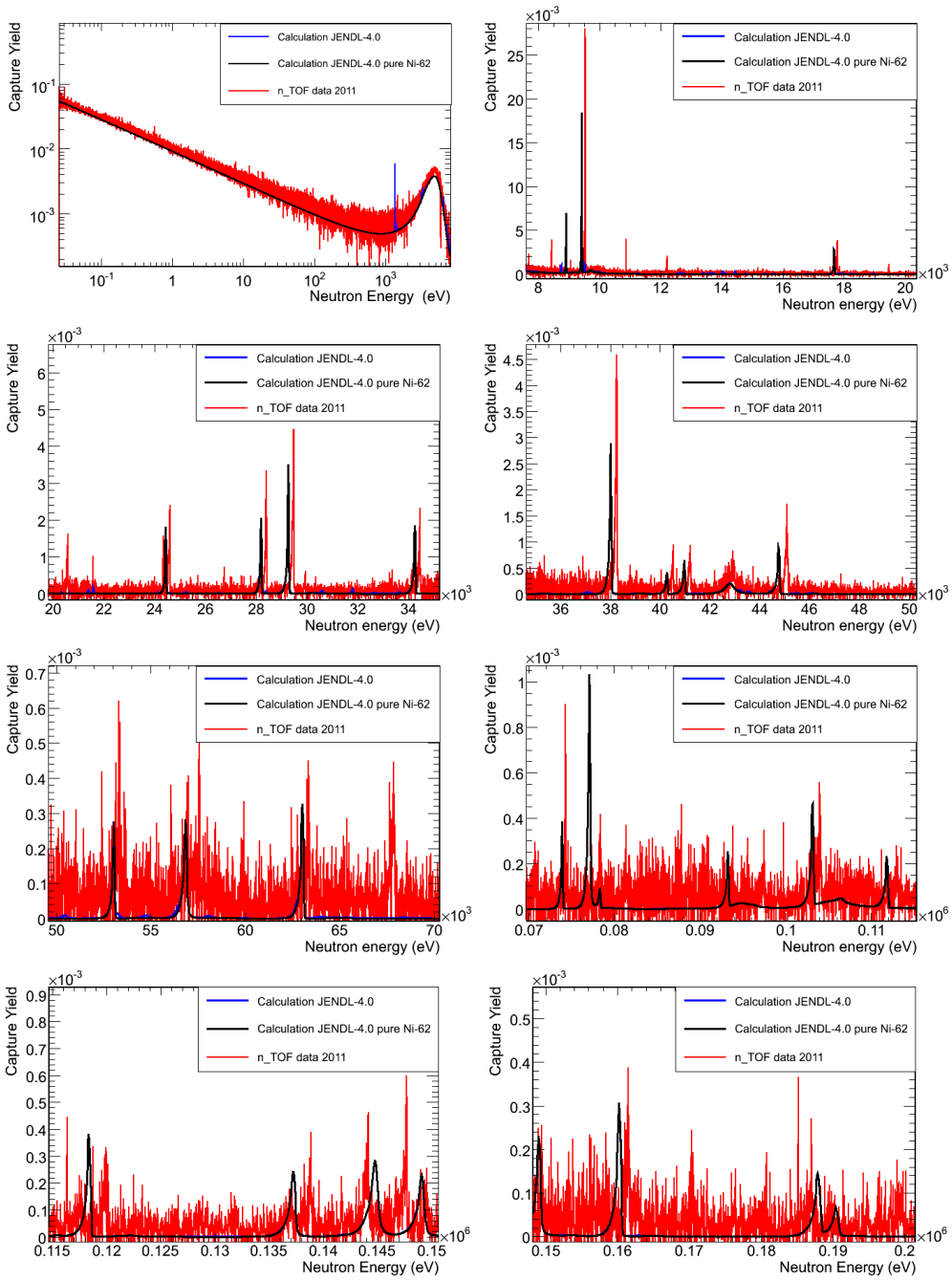

Figure 4.17: Capture yield of ^{62}Ni(n,γ) measured at n_TOF from thermal to 200 keV neutron energy compared to a calculation with resonance parameters listed in the JENDL-4.0 library. Most resonances of JENDL-4.0 can be seen in the data and additionally some new resonances are visible. However, there is a systematic offset in resonance energy between JENDL-4.0 and the n_TOF data.

the thermal cross section values, but the measured yield is systematically higher up to the prominent resonance at 4.6 keV. Apart from that there is a mismatch for most resonance energies, and some resonances in the measured data are missing in the JENDL library. A resonance which can be also seen in the data at 1.35 keV (first panel) can be attributed as being due to a strong resonance of the neutron capture cross section of ^{61}Ni, which has an abundance of 0.91% in the sample (see Appendix A). Apart from that resonance, there seems to be no significant contribution from resonances of the other Ni isotopes.

The first big resonance in ^{62}Ni(n,γ) provides a dominant contribution to the MACS at k_BT = 30 keV. The experimental information available about this resonance is listed in Table 4.6. The available data are scarce and contradictory, not only for the capture width, but also for the neutron width derived e.g. from transmission measurements.

Table 4.6: Resonance parameters of the 4.6 keV resonance in ^{62}Ni(n,γ) according to the EXFOR data base [103]

E_R (keV)	Γ_γ (eV)	Γ_n (keV)	Spin J	Author
4.6	0.76 ± 0.12	1.30*	0.5	Hockenbury *et al.* [95]
4.54 ± 0.05		1.34 ± 0.09	0.5	Garg *et al.* [104]
4.6	2.5			Axmann *et al.* [93]
4.5695		2.075		Axmann *et al.* [93]
4.607 ± 0.016		1.822 ± 0.018		Litvinskiy *et al.* [94]

* This value was assumed for fitting Γ_γ.

For a first fit of the 4.6-keV resonance, the value for Γ_n was kept fixed to the value obtained in the most recent measurement by Litvinskiy *et al.* since it reproduced best the measured data. A fit was performed from 3 keV to 8 keV, yielding a capture width of Γ_γ = 2.895 ± 0.003 eV and a resonance energy E_R = 4.641 ± 0.003 keV. The uncertainties given here are from the fit only. The comparison between data and a calculation using these parameters is shown in Fig. 4.18. The agreement between the fit and the data is good for thermal neutron energies and at the high energy tail of the resonance. The shape of the data cannot be reproduced at the low energy tail, which could be due to background in the data. In principle it is also possible to vary Γ_n additionally, since the resonance width is much broader than the resolution, which is of the order of eV in this energy range. A more detailed investigation has to be postponed, since there are no final results on the beam-interception factor as a function of energy yet, which affects the shape of the tail, especially in the thermal neutron energy region. Additionally, it needs to be investigated if the overall resonance shape is affected by prompt neutron scattering.

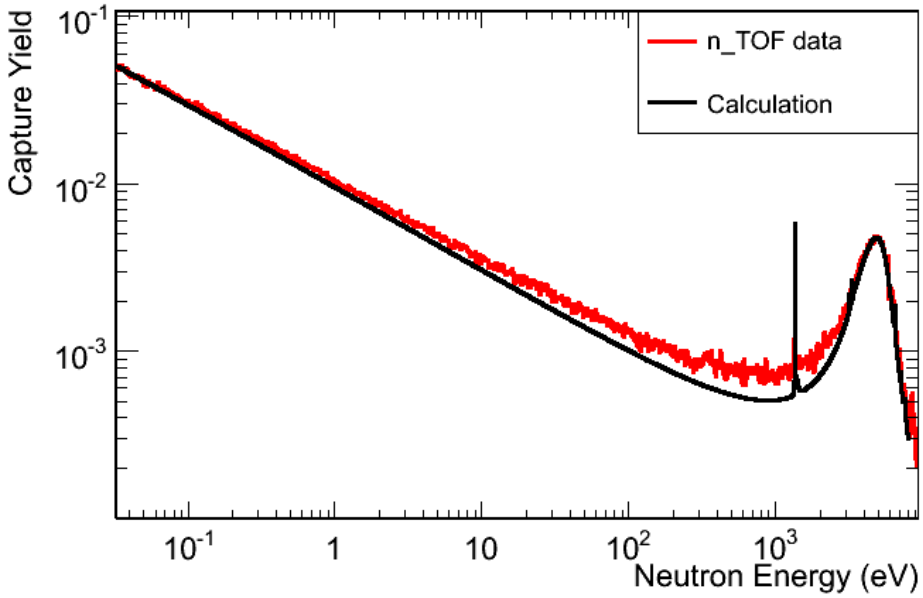

Figure 4.18: Calculation of the capture yield compared to the ^{62}Ni(n,γ) data from thermal to 8 keV with the resonance parameters obtained from a fit with SAMMY. The resonance parameters were obtained by fitting the resonance from 3 keV to 8 keV and fixing spin J and Γ_n. The thermal cross section as well as the high energy tail of the resonance was reproduced very well. Larger differences were found in the low energy tail.

A first calculation of the capture yield of ^{63}Ni(n,γ) compared to the expected background due to ^{62}Ni(n,γ) is shown in Fig. 4.19. The ^{62}Ni(n,γ) data are scaled according to the calculated mass ratio between ^{62}Ni present in the ^{63}Ni sample and the mass of the ^{62}Ni sample. At the top of the 4.6 keV resonance the data clearly don't match. Whether this is related to the isotopic composition of the ^{63}Ni sample, or due to the different multiple scattering background, needs to be addressed when more information is available. A mass spectroscopic measurement of the isotopic composition of the sample is currently performed at *Paul Scherrer Institute* (PSI) and results should be available in spring 2012 [105] (see also Appendix A). Below 2 keV there are several resonances in the ^{63}Ni data which cannot be seen in the ^{62}Ni spectra (upper panel on the right in Fig. 4.19). Those three big resonances originate from ^{63}Ni(n,γ) reactions. A resonance at around 200 eV neutron energy visible in the first panel is due to a strong resonance in the ^{59}Ni(n,γ) cross section. Radioactive ^{59}Ni was produced when breeding the ^{63}Ni sample in the reactor by neutron capture on the stable ^{58}Ni. Already an amount of less than 0.1% of ^{58}Ni in the sample can explain the presence of this resonance.
A rough estimation of the ^{63}Ni(n,γ) cross section can be given by subtracting the scaled ^{62}Ni spectrum and simply scaling the capture yield with a preliminary value for the

thickness according to $\sigma = Y/n$. The resulting cross section at thermal energies is around 20-25 b, which is in agreement with the available measurements. Of course this calculation neglects any effects due to multiple scattering and self-shielding. Also, the influence of the oxygen in the ^{63}Ni sample is not taken into account.

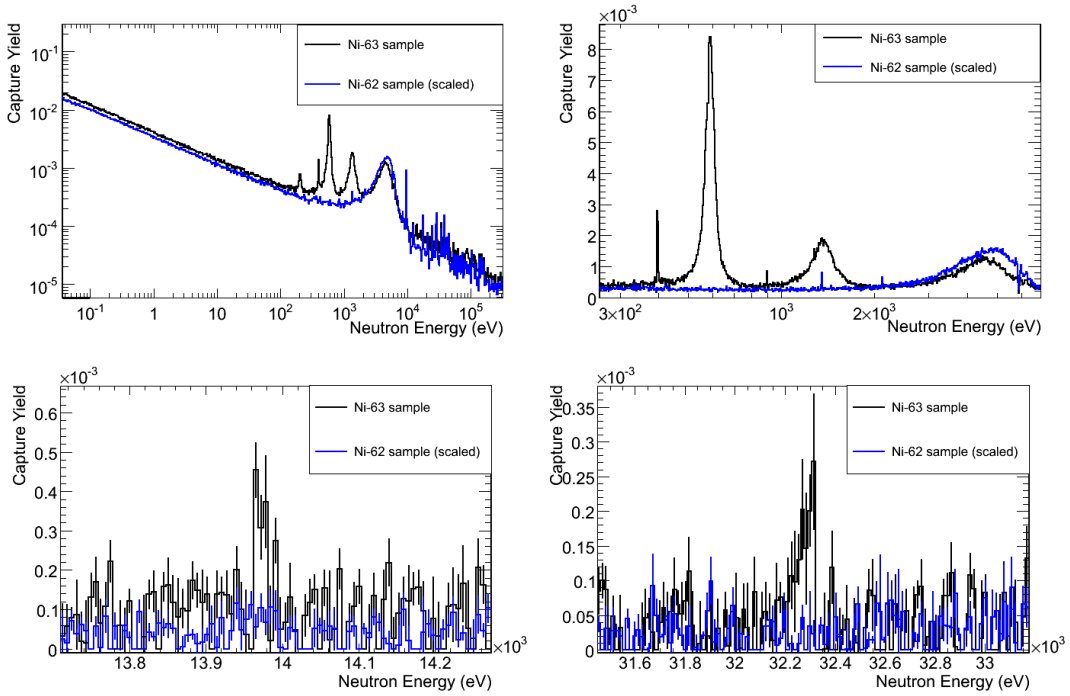

Figure 4.19: Capture yield of the ^{63}Ni sample compared to the expected background due to ^{62}Ni(n,γ). The upper panel on the left shows the energy range from thermal to 300 keV neutron energy, the upper panel on the right is a zoom into the lower keV region. The panels on the bottom show two examples for structures present in the ^{63}Ni data, which could be attributed to resonances in ^{63}Ni(n,γ).

4.4.3 Summary and Outlook

Cross sections of the reactions ^{62}Ni(n,γ) and ^{63}Ni(n,γ) were measured over a wide energy range from thermal neutron energies to several hundred keV at n_TOF. The results for ^{62}Ni(n,γ) show a fairly good agreement with the most recent evaluations ENDF/B-VII.1 and JENDL-4.0. The data have high energy resolution and resonances can be identified up to at least 200 keV. Overall uncertainties of the final results in the energy dependent cross section are expected to be around few percent, which will allow to determine MACSs over the entire energy range relevant for *s* process nucleosynthesis from $k_BT = 5$ keV to $k_BT = 90$ keV.

For the ^{63}Ni(n,γ) reaction, three new resonances were identified below 1 keV neutron energy. A first analysis shows that the cross section at thermal neutron energies is compatible with previously measured values. After a careful resonance analysis of ^{62}Ni(n,γ), the background in the ^{63}Ni data due to this reaction can be subtracted. This will allow for the first time to determine MACSs of ^{63}Ni(n,γ), which is crucial for understanding the production of Cu in the *s* process.

Neutron capture cross sections are the key ingredient for *s* process studies. In the weak *s* process, a set of accurate neutron capture cross sections in the intermediate mass region from $60 < A < 90$ is of major importance since one (n,γ) cross section affects the abundances of a number of successive isotopes in the reaction chain (see Sec. 4.1).
Besides ^{62}Ni and ^{63}Ni, the neutron capture cross sections of the isotopes ^{58}Ni and ^{54,56,57}Fe have been measured recently at n_TOF with the aim of providing accurate cross sections in this mass region. Furthermore the study of neutron capture reactions on radionuclides, acting as branching points in the *s* process (e.g. ^{79}Se, ^{95}Zr or ^{151}Sm) are critical to understanding physical conditions in stellar environments. In this respect, exciting new possibilities open up at future facilities, providing much higher neutron fluxes which allow the measurement of even smaller sample masses and cross sections by the time-of-flight technique, for example the neutron source FRANZ in Frankfurt [106] producing neutrons in the keV region via the ^{7}Li$(p,n)^{7}$Be reaction and EAR-2 at n_TOF (second experimental area at n_TOF, with a shorter flight path of 20 m) [107].

5 ^{197}Au(n,γ) cross section in the unresolved resonance region

5.1 Motivation

Standard cross sections are critical for obtaining accurate and precise reaction cross sections, such as for the (n,γ) reactions described in the thesis. Besides normalizing to a saturated resonance as already described in the previous chapter, it is important to determine the normalization also at different neutron energies. The ^{197}Au(n,γ) cross section is an established cross section standard for thermal neutron energies (at 0.0253 eV) and for the energy range between 0.2 and 2.8 MeV [108]. The evaluation of the Au standard cross section is based on available experimental data, including absolute measurements, as well as information from relative measurements and from measurements of cross-section ratios. Although the evaluation covers the lower keV region above the resolved resonance region as well, it is not a recommended standard below 200 keV due to discrepancies of 6-8% compared to results, which were essentially obtained in two well-designed experiments, a time-of-flight measurement at Oak Ridge Electron Linear Accelerator (ORELA) [109, 110] and an activation measurement at the Karlsruhe Van de Graaff accelerator [34], which agree within 1.5%.

The time-of-flight measurement of Macklin [109, 110] was performed in the energy range from thermal up to 2 MeV with the intention to establish an accurate (n,γ) cross section for use as a standard. The experiment was carried out with the pulse height weighting technique (PHWT) [54] at the 40-m station of the ORELA facility. The data were taken with a sample 0.55 mm in thickness and an energy resolution that increased from 0.25% (FWHM) at 100 keV to 0.8% at 2 MeV. This pioneering effort, which claimed an overall uncertainty of 3.6 to 4.7%, reported also significant structures in the energy region up to about 200 keV.
In the completely different activation measurement at Karlsruhe neutrons were produced via the ^{7}Li$(p,n)^{7}$Be reaction at proton energies of 1912 keV [34] (for more information see Section 3.4 and Chapter 6). The capture cross section of ^{197}Au was measured in this spectrum by irradiation of a spherically shaped gold sample that covered the entire neutron beam. In this configuration, the total neutron fluence could be determined with an uncertainty of 1.4% by the ratio of the induced γ activities of ^{198}Au and ^{7}Be without any further normalization. In astrophysics applications, the accurate result

of the activation measurement [34] has been used to normalize the energy-dependent Au(n,γ) cross section of Macklin [110] to define a reference cross section that was adopted in numerous measurements for quantitative *s*-process studies as described in Ref. [111].

This work is part of a new attempt for measuring the ^{197}Au(n,γ) cross section via the time-of-flight technique at the n_TOF facility. The two different detection systems described in Chapter 3 have been used in the experiment, the C_6D_6 detection system for the energy range from 1 eV to 1 MeV and the TAC for the region below about 20 keV. Partial results have been published for the resolved resonance region below 5 keV [112], showing excellent agreement between the values obtained with both techniques.
The present study deals with the analysis of the C_6D_6 measurement in the unresolved region up to 400 keV neutron energy. Experimental information on systematic effects was collected in a series of background runs with a lead sample, and comprehensive Monte Carlo (MC) simulations were carried out to validate the remaining corrections.

5.2 Measurement

The measurement was performed during n_TOF Phase I. The gold sample was 15.02 mm in diameter and 0.38 mm in thickness. It was glued onto a 75 μm thick Kapton foil sustained by a carbon fiber frame, which was always outside of the neutron beam. A lead sample was used for determining the neutron induced backgrounds (e.g. from neutrons scattered on the sample) and in-beam γ rays. The sample characteristics are listed in Table 5.1. An empty position on the sample ladder served for measuring the sample-independent background. For transforming time-of-flight to neutron energy, the relation from Ref. [51] was adopted.

Table 5.1: Sample characteristics. The thickness is given in atoms per barn.

Sample	Mass	Thickness	Diameter	Chemical
	(mg)	(10^{-3} b^{-1})	(mm)	form
Au	1299.0	2.243	15.02	metal
^{nat}Pb	2027.0	3.173	15.38	metal

5.3 Data analysis

5.3.1 Determination of the capture yield

The weighted count spectra were already obtained from the preceding n_TOF analysis of the resolved resonance region [112]. After application of the WFs the capture yield is obtained as

$$Y = \frac{1}{\mathcal{A}} f_{\mathrm{ms}} \frac{(C_{\mathrm{w}} - B_{\mathrm{w}})}{\phi E_{\mathrm{c}}} \tag{5.1}$$

where $\mathcal{A}$ is the fraction of the neutron beam covering the sample, C_{w} is the weighted, dead-time corrected energy spectrum, B_{w} is the weighted background, ϕ is the neutron flux, and E_{c} is the excitation energy.
For the flux a modeled version of the standard flux of n_TOF phase I [44] was used. To determine the beam-interception factor $\mathcal{A}$, the data were normalized relative to the saturated 4.9-eV resonance in Au. The energy dependence of $\mathcal{A}$ was taken into account using information on the beam profile, which has been simulated (2-4% uncertainty) and is in agreement with corresponding measurements [47] (see Chapter 3.2.2). The beam-interception factor relative to the value at 4.9 eV is plotted in Fig. 5.1 for a sample that is 15 mm in diameter. The same factor was used in previous measurements of ^{232}Th

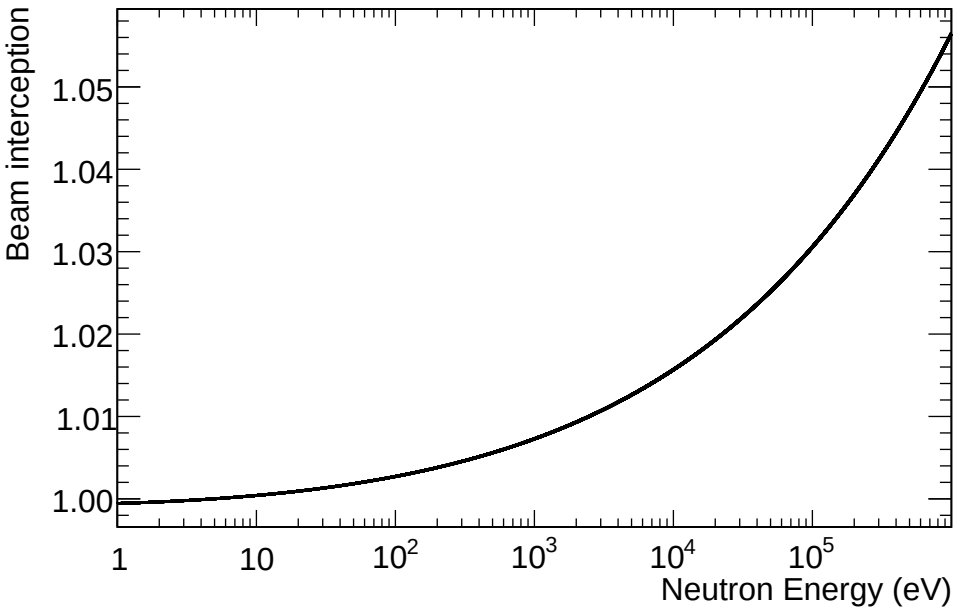

Figure 5.1: The fraction of the neutron beam covered by a sample 15 mm in diameter relative to the value applied at the saturated resonance at 4.9 eV.

[113] which were in excellent agreement with results for ^{232}Th obtained at GELINA [114]. The uncertainty on the beam profile correction factor is negligible.
Since in the present case the measurement is self normalized to the 4.9-eV resonance, additional corrections, e.g. the energy threshold applied to the deposited γ energy or the creation of conversion electrons are not necessary, assuming that the decay spectra of the compound nucleus are similar for different neutron energies. This has been verified by analyzing the data using different energy thresholds and comparing the resulting capture yields. The sample-related correction f_{ms} for neutron multiple-scattering and neutron self-shielding was calculated with the code SESH [58]. As shown in Fig. 5.2, f_{ms} is always smaller than 4% in the considered energy range. Assuming a conservative value for the uncertainty of 10%, this correction will enter into the final uncertainty with 0.4%.

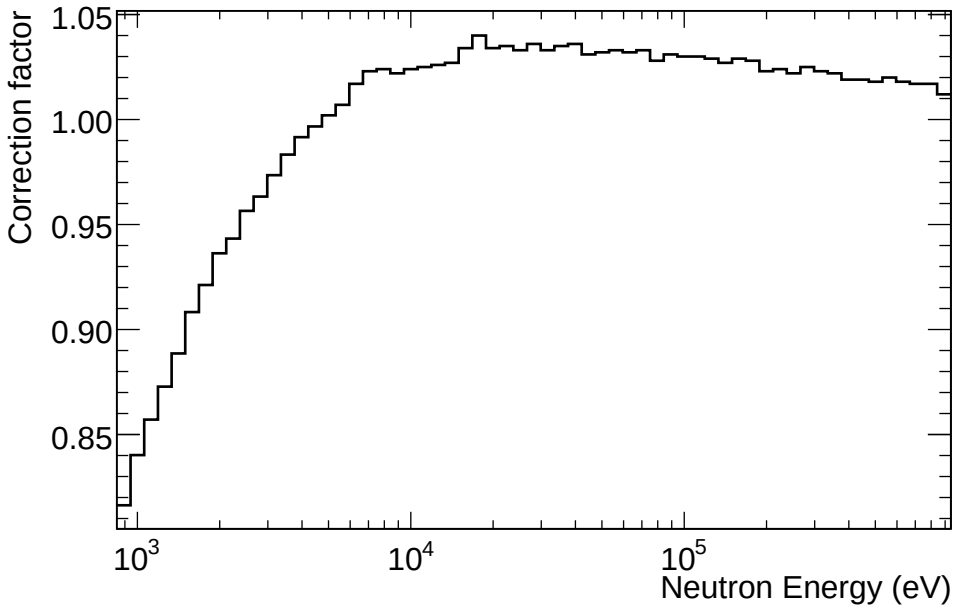

Figure 5.2: Correction factor for multiple scattering and self-shielding calculated with the code SESH [58].

5.3.2 Background components

The background in the keV region is essentially determined by elastic neutron scattering and by the contributions due to in-beam γ rays. These components were determined experimentally in dedicated runs with a lead sample. Additional measurements with

neutron filters have been made for normalization of these background runs. The sample-independent background was obtained with an empty position in the sample ladder. The individual spectra are shown in Fig. 5.3. The effect of sample activation was practically negligible thanks to the highly intense neutron pulses of the n_TOF facility.
The contribution of neutron induced background and (to a lesser extent) the sample-independent background measured without a sample exhibit a smooth decrease close to a $1/v$ dependence with neutron energy. The background reduces to this component below 200 eV.

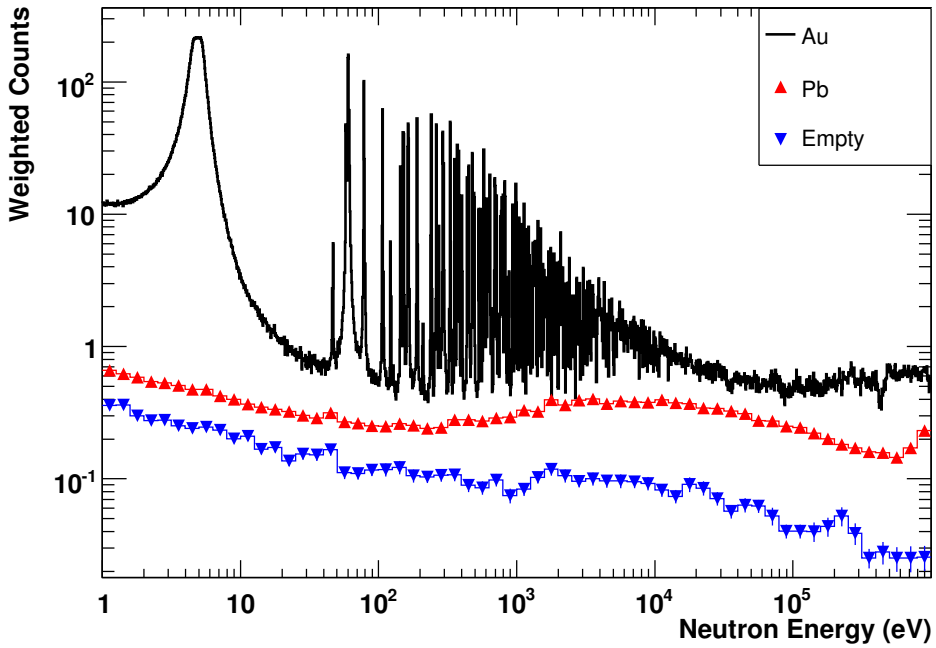

Figure 5.3: Weighted Au spectrum compared to runs with Pb and with an empty position in the sample ladder.

Between 200 eV and 500 keV the detection of in-beam γ rays, which are scattered in the sample represents the main background contribution (see also Sec. 3.3.3). It turned out that the spectrum taken with the Pb sample shown in Fig. 5.4 was particularly useful for characterizing both background components described above because the capture cross section of Pb is extremely low compared to that of Au and is almost free of resonances in the energy range of interest, whereas the cross section for neutron elastic and γ scattering is similar to that of gold.

At high energies, γ rays produced by inelastic neutron scattering add another background component, which was investigated by increasing the energy threshold from the nominal 200 keV to 1 MeV. The comparison of both spectra in Fig. 5.5 shows good

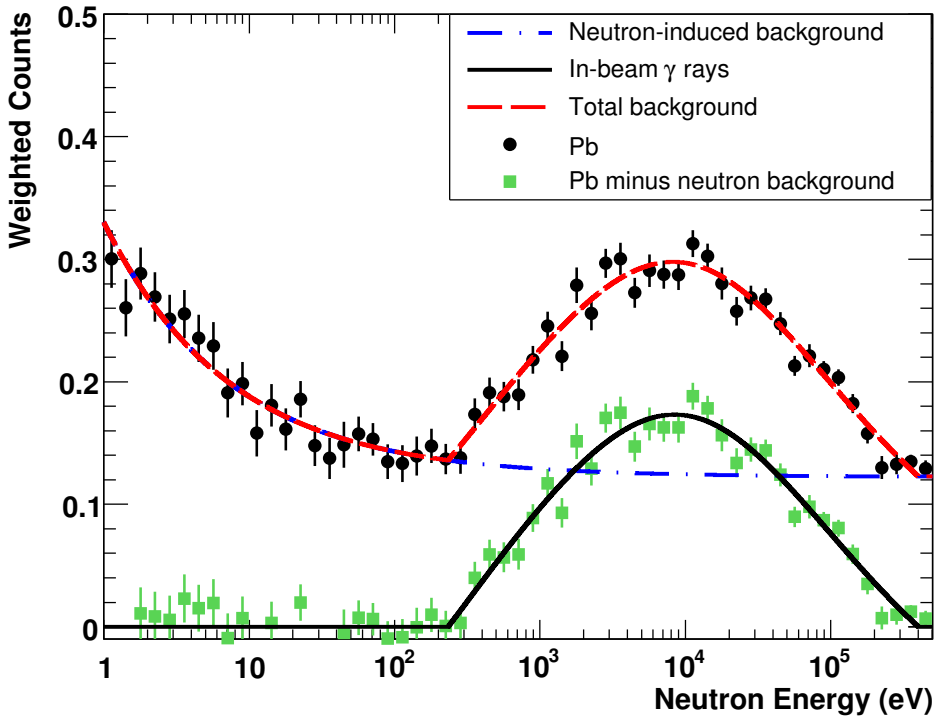

Figure 5.4: Decomposition of the spectrum measured with the Pb sample into the close to a $1/v$ dependence of the neutron scattering background and the contribution from in-beam γ rays.

agreement up to 600 keV. The small discrepancies in the 10-80 keV region are due to the small remaining in beam γ background in the 1 MeV spectrum where a proper subtraction due to low statistics is not possible.

5.3.3 Background shape and normalization

Once the neutron-energy dependence of both, neutron-induced and in-beam γ ray components have been accurately characterized (see Sec. 5.3.2), the total background can be expressed as

$$B(E_n) = f_n\, B_n(E_n) + f_{\text{att}}\, f_\gamma\, B_\gamma(E_n) \tag{5.2}$$

where the terms B_{n} and B_γ describe the background shape due to different background components, and f_n and $f_{\text{att}}\, f_\gamma$ are the respective factors for normalizing these components to the Au measurement. The neutron induced and in-beam γ component $B_n(E_n)$ and $B_\gamma(E_n)$ were parametrized as

$$B_n(E_n) = a + b/\sqrt{E_n} \tag{5.3}$$

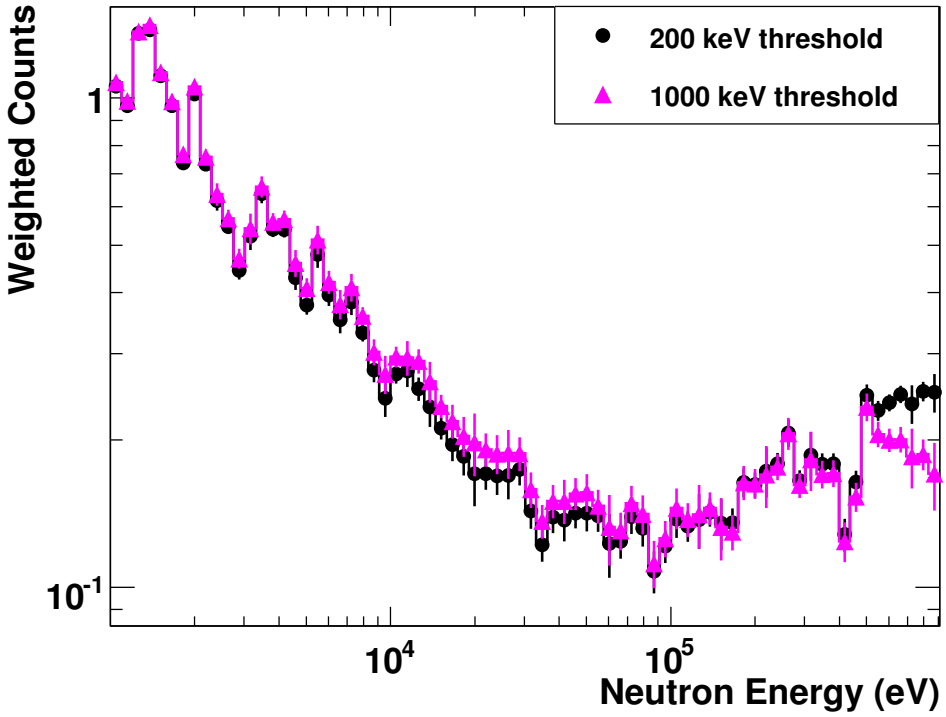

Figure 5.5: Normalized, weighted counts obtained with the nominal γ ray threshold of 200 keV and with a threshold of 1 MeV. The effect of the inelastic channel appears at energies of about 600 keV.

and

$$B_\gamma(E_n) = c + d \times \exp(-e/\sqrt{E_n}) + f \times \exp(g/\sqrt{E_n}) \tag{5.4}$$

The exponential terms in Eq. 5.4 represent the production and decay of activation products in the spallation target. Values for a and b were determined by a least squares fit of the Pb spectrum from 1 eV to 100 eV and at 500 keV where the in-beam γ background disappears again. After subtracting the resulting neutron induced background from the Pb spectrum, the coefficients c to g were fitted to the remaining part (Fig. 5.4).

To normalize these background components, a spectrum of the Au sample was taken with filters in the neutron beam downstream of the first collimator [115]. The thickness of the filters (30 mm for Al and for 0.8 mm W) was chosen such that neutrons were completely removed at the position of black resonances at 18.8 eV in W and at 34.7 keV in Al. The Au spectrum taken with filters was first corrected for the overall flux attenuation in the filters. The normalization factors f_n and f_γ for the neutron induced and in-beam γ ray components were then determined such that the sum of the background components matched the filter dips, as shown in Fig. 5.6.

The best fit values were found for $f_n = 0.558 \pm 0.033$ and $f_\gamma = 0.354 \pm 0.017$. The uncertainties were evaluated by considering the counting statistics in the filter dips, the fit of the filter transmission with a single-level Breit-Wigner shape, and by repeated fits using different energy bin widths.
The factor f_{att} accounts for the attenuation of in-beam γ rays in the filters. It was determined by a series of GEANT3 [116] simulations based on the in-beam γ ray spectrum from Ref. [37] and on a detailed replica of the experimental setup[1]. The simulated events were analyzed in the same way as the real data, with a threshold of 200 keV on the deposited energy in the C_6D_6 detectors. The correction for the γ attenuation in the W and Al filters was 1.83±0.08, where the uncertainty in the simulation was mostly due to the effect of the detection threshold.
In addition, the background was also investigated in a second approach by determin-

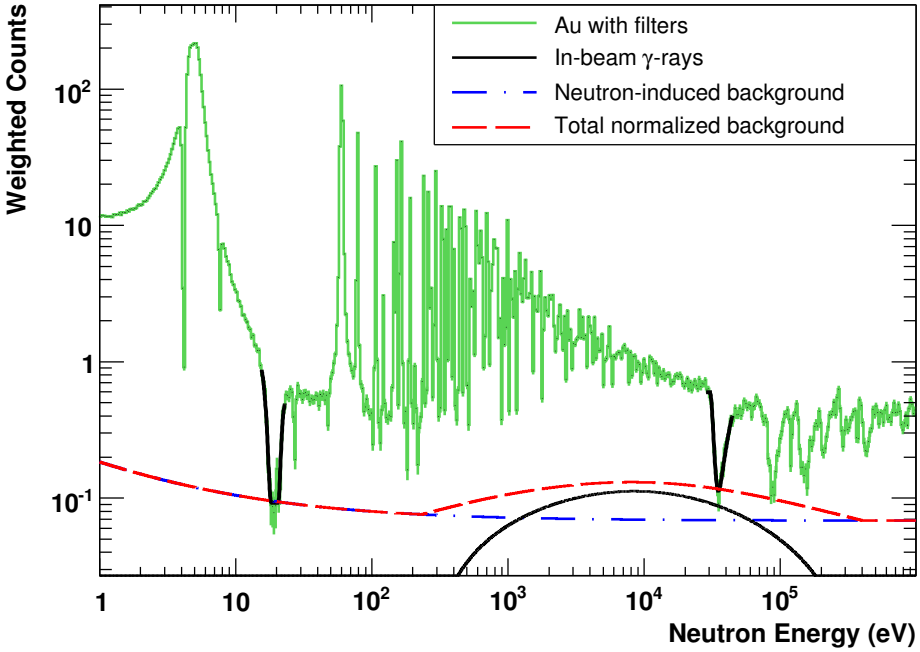

Figure 5.6: Au spectrum with filters in the neutron beam. The two background components B_n and B_γ have been fitted to match the minimum of the filter dips.

ing the scaling factor of the in-beam γ background by Monte-Carlo simulations using GEANT3 and MCNPX[2]. The simulations of the γ interaction in the Pb and Au samples and their subsequent detection in the C_6D_6 scintillators were performed taking into account the areal density, the atomic number of the Pb and Au, and the spectrum

[1]The simulation has been performed by co-authors of the article [I1].
[2]The simulations have been performed by co-authors of the article [I1].

of the in-beam γ rays. The scaling factors obtained from the simulations were 0.625 (GEANT3) and 0.658 (MCNPX), respectively, and thus were in excellent agreement with each other and with the corresponding value $f_{\text{att}}f_{\gamma} = 0.648$, found by the method previously described. Hence $f_{\text{att}}f_{\gamma}$ was adopted with 0.648 ± 0.032, estimating an uncertainty of 5%. The resulting uncertainty of the background varies with neutron energy and peaks at the minimum of the signal/background ratio near 30 keV. Due to a signal/background ratio of 3-10, the contribution to the uncertainty of the cross section amounts to 0.6-1.7% in the energy range of the experiment (see also Table 5.2).

5.3.4 Normalization of the capture yield

The neutron capture yield is self-normalized since the 4.9-eV resonance is saturated for the thickness of the used sample. The normalization was obtained by fitting the top of this resonance with the code SAMMY [53]. The uncertainty of the normalization is estimated as being 1.0%. However, the used weighting function may be different in a saturated resonance because the capture γ rays originate only in a thin layer of the sample instead of throughout the sample in the URR. The size of this effect and the corresponding correction factor depend on the details of the detector-sample geometry and can be obtained by Monte Carlo simulations[3] of the weighting function, modeling either a thin layer or a homogeneous gamma source inside the sample [117]. In the present geometry, the effect was 0.6%; hence, the yield was scaled by the factor 1.006.

5.3.5 Uncertainties

The uncertainties related to the various steps of data analysis have been discussed throughout the previous subsections. These contributions are summarized in Table 5.2 for three representative neutron energies to illustrate the relatively weak effect of the energy-dependent components.

The comparison shows that the present systematic uncertainty is dominated by the energy dependence of the neutron flux and the PHWT. Imperfections in the sample shape introduce an additional systematic uncertainty of 0.5%.

5.4 Results

5.4.1 Comparison with evaluations and previous data

The neutron capture cross section of ^{197}Au was measured from 5 to 400 keV with an overall uncertainty of 3.9-6.7%. Although the energy range was extending to about 1

[3]The simulation has been performed by co-authors of the article [I1].

Table 5.2: Systematic and statistical uncertainties at different energies for the ^{197}Au(n,γ) cross section measurement at n_TOF.

Source of uncertainty	Uncertainty (%)		
	10 keV	30 keV	100 keV
PHWT		2.0	
Neutron flux shape		2.0	
Normalization		1.0	
Sample geometry		0.5	
Background subtraction	1.0	1.5	1.3
Multiple scattering and self shielding	0.3	0.4	0.3
Counting statistics*	3.0	4.4	3.7
Total	4.4	5.6	5.0

* For a neutron energy resolution of 20 bins per energy decade.

MeV, the data given here are restricted to the region below 400 keV, because the uncertainties of the present data are increasing at higher energies and did not provide meaningful constraints for the standard. The results are given in Table 5.3 with a resolution of 20 bins per decade. The comparison with evaluated cross sections transformed to 20 bins per decade in Fig. 5.7 shows good agreement with the ENDF/B-VII.1 [96] evaluation, which contains the standard evaluation, as well as with the evaluations JENDL-4.0 [97] and JEFF-3.1 [98]. From 200 to 400 keV, where the Au(n,γ) cross section is an accepted standard, the agreement is within quoted uncertainties for all energy bins except the region from 223 to 251 keV and from 282 to 316 keV, where the deviations are 5.3% and 7.3%, respectively. The cross section averaged from 200 to 400 keV differs by 2.1% from the averaged standard cross section.
In view of the discrepancy between the ENDF evaluation and the accurate cross sections reported by Macklin *et al.* [109, 110] and by Ratynski and Käppeler [34], the following discussion concentrates on these measurements. The comparison with the first of these data sets is particularly illustrative, because the energy-dependent cross section provides a more stringent test compared to the spectrum-averaged result. In Fig. 5.8, the present results and the data of Refs. [109, 110] are plotted with the same binning to facilitate the direct comparison. Also, the ratio of the two datasets is shown. While the top and middle panels show that the cross sections obtained in this work are systematically higher up to 100 keV, the zoom into the region from 8 to 40 keV with a resolution of 250 bins per decade in the bottom panel demonstrates that the cross section fluctuations reported by Macklin *et al.* [109, 110] are quantitatively confirmed by the present data. The origin of these structures is discussed in Section 5.4.2.

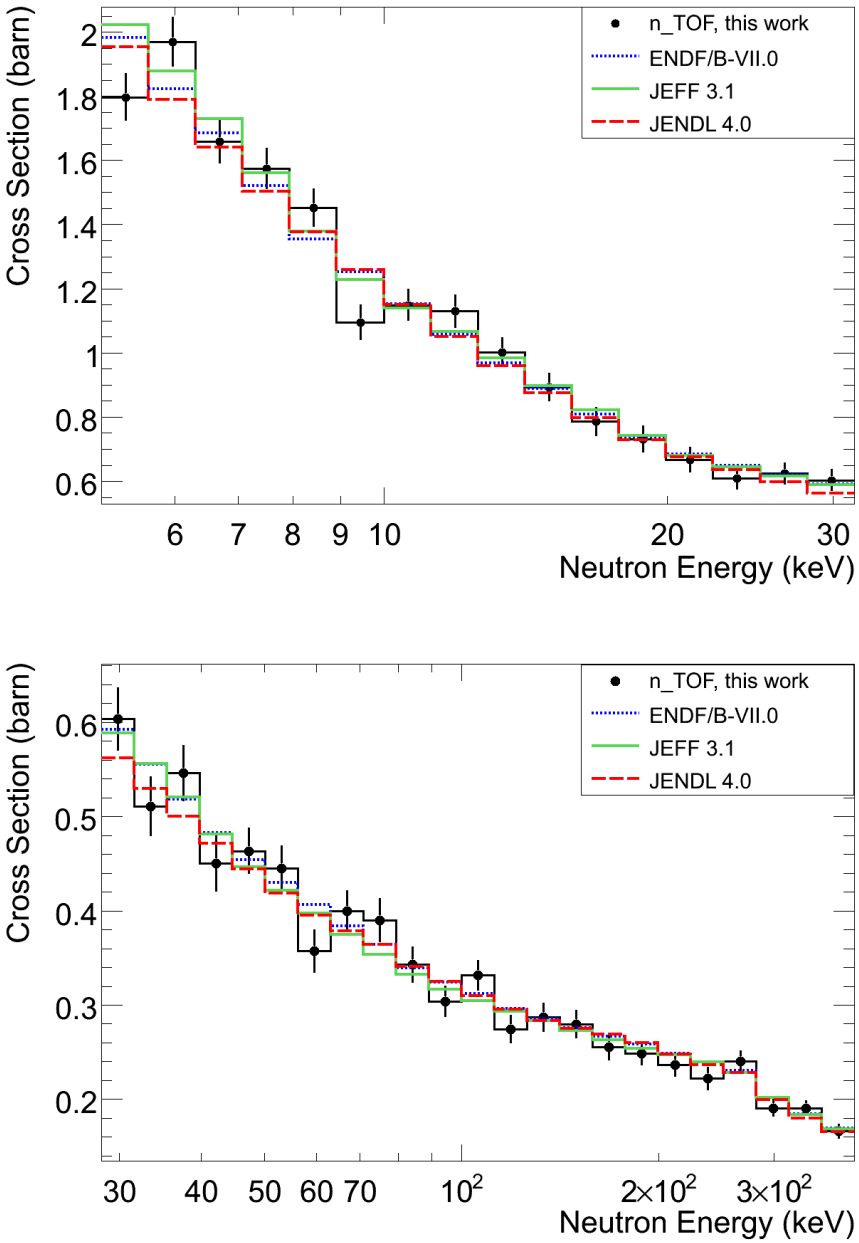

Figure 5.7: Comparison of present results with a resolution of 20 bins per decade with evaluated data sets from the ENDF/B-VII.1 [96], JEFF-3.1 [98] and JENDL-4.0 [97] libraries.

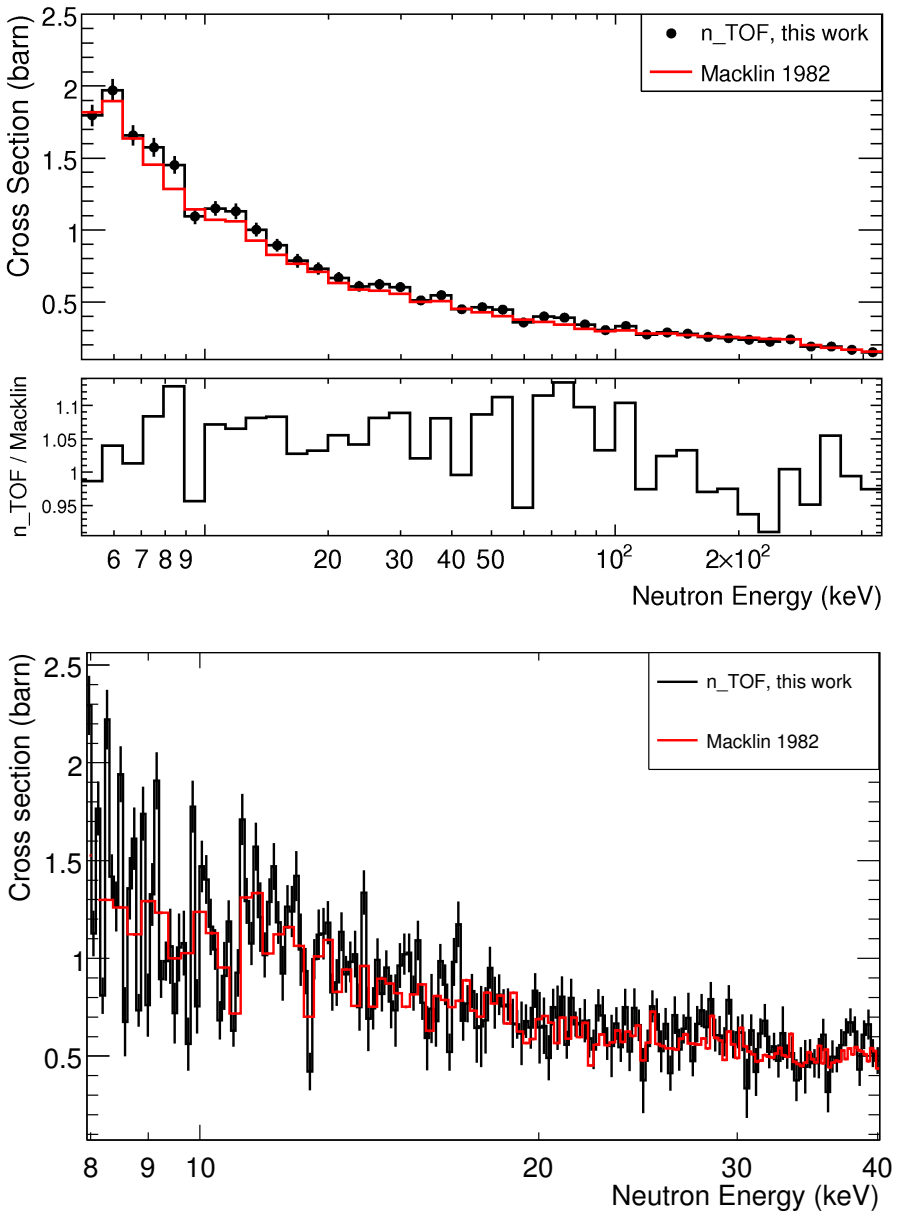

Figure 5.8: (top) The present results compared to the data of Macklin *et al.* [109, 110] for the full energy range from 5 to 400 keV (20 bins per decade). (middle) Results divided by the data of Macklin *et al.* (bottom) Comparison of present results with the data by Macklin *et al.* in the energy region from 8 to 40 keV (250 bins per decade, with the original binning of Refs. [109, 110]) to highlight the pronounced cross section fluctuations. Uncertainties shown for n_TOF data in the bottom panel are statistical.

Table 5.3: The ^{197}Au(n,γ) cross sections and overall uncertainties.

E_{low} (keV)	E_{high} (keV)	σ (mb)	Uncertainty (%)		
			Statistic	Systematic	Total
5.010	5.621	1817	2.7	3.1	4.1
5.621	6.307	1970	2.4	3.1	3.9
6.307	7.076	1661	2.7	3.1	4.1
7.076	7.940	1569	2.6	3.1	4.1
7.940	8.908	1447	2.7	3.2	4.1
8.908	9.995	1092	3.8	3.2	5.0
9.995	11.215	1150	3.0	3.2	4.4
11.215	12.583	1125	3.3	3.2	4.6
12.583	14.119	1000	3.3	3.2	4.7
14.119	15.842	894	3.6	3.3	4.8
15.842	17.775	786	4.7	3.3	5.8
17.775	19.943	730	4.6	3.4	5.7
19.943	22.377	666	4.9	3.4	6.0
22.377	25.107	608	4.8	3.4	5.9
25.107	28.171	623	4.2	3.4	5.4
28.171	31.608	601	4.4	3.4	5.6
31.608	35.465	509	5.2	3.6	6.3
35.465	39.792	547	4.2	3.5	5.5
39.792	44.648	450	5.7	3.5	6.7
44.648	50.096	463	4.1	3.4	5.4
50.096	56.208	446	4.2	3.4	5.4
56.208	63.067	357	5.4	3.5	6.4
63.067	70.762	400	4.2	3.3	5.4
70.762	79.396	389	5.1	3.3	6.1
79.396	89.084	342	4.4	3.4	5.6
89.084	99.954	304	4.3	3.4	5.5
99.954	112.150	332	3.7	3.3	5.0
112.150	125.835	274	4.3	3.3	5.5
125.835	141.189	287	4.3	3.3	5.4
141.189	158.416	280	4.3	3.3	5.4
158.416	177.746	256	4.4	3.3	5.5
177.746	199.434	249	4.0	3.2	5.2
199.434	223.769	236	4.1	3.2	5.2
223.769	251.073	222	4.6	3.2	5.6
251.073	281.709	240	3.5	3.2	4.7
281.709	316.082	191	3.8	3.2	4.9
316.082	354.650	190	2.9	3.2	4.3
354.650	397.924	166	3.3	3.2	4.6

Furthermore, we calculated the MACS from 5 keV to 100 keV using the code SAMMY. For energies below 5 keV we used resonance parameters determined at n_TOF in the same experiment, published in Ref. [112], above 400 keV we used the ENDF/B-VII.1 cross section. This allows a direct comparison to the MACS at 30 keV given by Ratynski and Käppeler. In Table 5.4 the MACSs are listed from 5 to 100 keV. The contributions from the regions below 5 and above 400 keV, which are not covered by the present results, are indicated separately.

Table 5.4: MACSs of ^{197}Au(n,γ) from 5 to 100 keV with total uncertainties. Contributions outside of the investigated energy range are listed separately.

kT (keV)	MACS (mb)	Contribution to MACS (%)	
		$E_n < 5$ keV	$E_n > 400$keV
5.0	1970 ± 70	49.6	-
6.0	1729 ± 61	42.2	-
7.0	1550 ± 54	36.5	-
8.0	1412 ± 49	32.0	-
9.0	1302 ± 46	28.3	-
10.0	1212 ± 42	25.3	-
12.5	1044 ± 37	19.7	-
15.0	927 ± 33	15.9	-
17.5	841 ± 30	13.2	-
20.0	775 ± 27	11.2	-
25.0	678 ± 24	8.4	-
30.0	611 ± 22	6.6	-
35.0	560 ± 20	5.3	-
40.0	521 ± 18	4.4	-
45.0	490 ± 17	3.7	0.1
50.0	464 ± 16	3.2	0.2
60.0	423 ± 14	2.5	0.5
70.0	392 ± 13	2.0	1.2
85.0	357 ± 12	1.5	2.9
100.0	330 ± 10	1.2	5.2

The total uncertainty of the MACS ranges from 3.1-3.6% since it is dominated by systematic uncertainties. In the URR we see a contribution of 0.7% to the MACS uncertainty due to counting statistics. Because the cross section increases toward lower energies, it is safe to assume that the statistical uncertainty becomes smaller as well. Therefore, we adopt a 0.7% uncertainty for the fraction of the RRR as a conservative estimate. The systematic uncertainties on the MACS ranges from 3.0-3.5%. The MACS

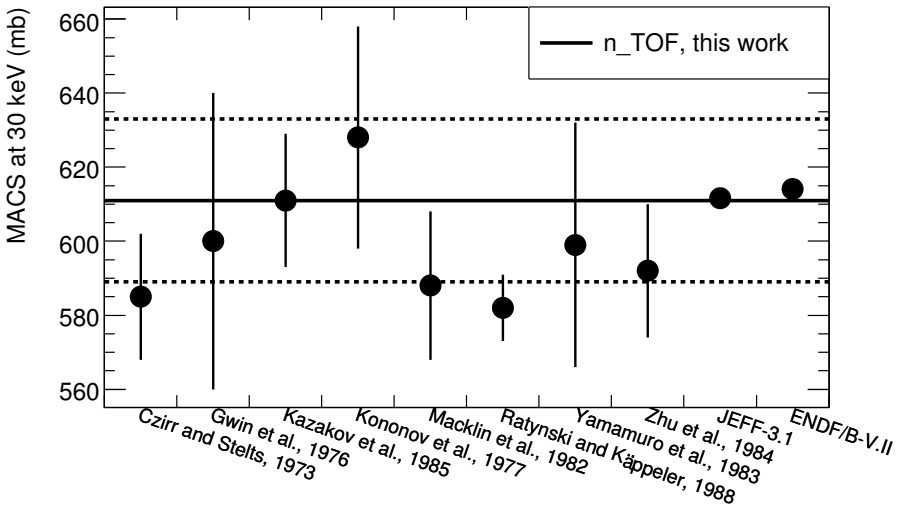

Figure 5.9: Comparison of the MACS at 30 keV (dashed lines indicate 1σ uncertainty) with selected experimental data [110, 34, 118, 119, 120, 121, 122, 123] and the evaluations ENDF/B-VII.1 and JEFF-3.1. All data are taken from the KADoNiS compilation [67, 68].

at 30 keV is 582 ± 9 mb, according to Ratynski and Käppeler [34], while the present data yield a MACS of 611 ± 22 mb, which is 4.7% higher. In Fig. 5.9 a comparison between selected experimental data and the two evaluations ENDF/B-VII.1 and JEFF-3.1 is shown. Our data show perfect agreement with Kazakov *et al.* [123] and the evaluations and are also still in fair agreement with Refs. [34, 109, 110, 118, 119, 120, 121, 122].

5.4.2 Gross structures

From the average level spacing of $\ell = 0$ states in ^{198}Au above the neutron binding energy ($\langle D_0 \rangle = 16.5 \pm 0.9$ eV) and from the width of these compound states (of the order of 0.3 eV at 10 keV) it is obvious that the significant structures in the capture cross section of Au (Figs. 5.7 and 5.8) are certainly not due to single resonances. Likewise, structures in the neutron flux can be excluded as a possible explanation because these are much smaller and are not at all correlated with those seen in the gold data.
The origin of these structures has been investigated by simulations[4] using artificial sets of resonances with realistic statistical properties, which were obtained from the observed average level spacings $\langle D_0 \rangle$, neutron strength function ($S_0 = 1.9 \times 10^{-4}$), and average γ ray width ($< \Gamma_\gamma >= 0.128 \pm 0.006$ eV) assuming a $(2J + 1)$ dependence of the level density. Based on the standard Fermi-gas model this yields 454 and 758 levels

[4] All simulations of Au resonances and calculations using the simulated data of the Au cross section in this subsection have been performed by co-authors of the article [I1].

in the range from 0 to 20 keV for $J = 1$ ($\langle D_0 \rangle = 44.1$ eV) and $J = 2$ ($\langle D_0 \rangle = 26.4$ eV), respectively. The statistical properties of each set are compatible with a Wigner distribution of the level spacings, a Porter-Thomas distribution of neutron widths and a constant or Gaussian distribution of the gamma widths.
The point-wise cross section data calculated with the multilevel Breit-Wigner formalism using the PREPRO code [124] are Doppler broadened with $T = 300$ K and $T = 4560$ K. The higher temperature was chosen because it corresponds to the n_TOF resolution in the neutron energy range from 10 to 20 keV (FWHM $\approx$ 18 eV). The calculated spectra with three sets of simulated resonances are compared in Fig. 5.10 with the experimental cross section using a resolution of 100 bins per decade.

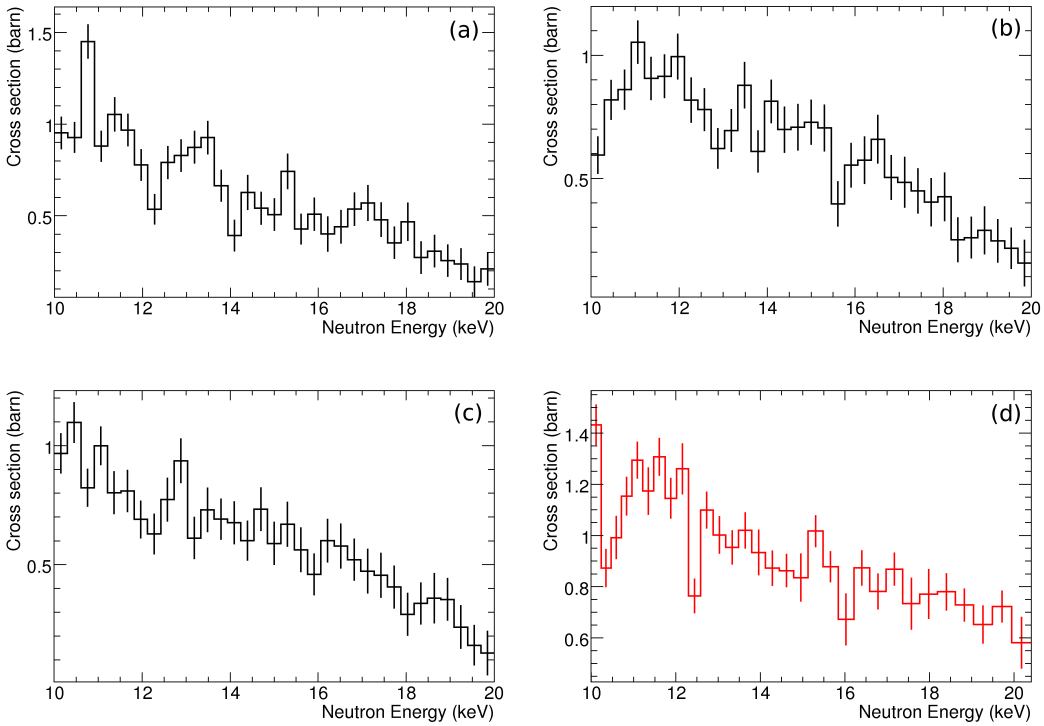

Figure 5.10: (a-c) Simulated cross sections compared to (d) experimental data in the region between 10 and 20 keV. Uncertainties shown for n_TOF data and simulations are statistical.

Three different sets of simulations have been performed, resulting in three completely different sets of resonances, which exhibit fluctuations corresponding to the experimentally observed structures. The error bars are estimated assuming a statistical uncertainty of $N^{-0.5}$ for N events in the bin. Although no real agreement with the experimental data is to be expected, the simulated fluctuation properties are clearly compatible with the structures in the cross section. This supports the adopted interpretation that they reflect

the density of compound states at excitation energies of 10 – 20 keV above the neutron separation energy.
If the data are plotted with much finer binning, the comparison with the simulations confirms the real nature of the structure. This is illustrated in Fig. 5.11, where the bin width of ≈ 7 eV is considerably smaller than the experimental resolution of 22 eV at 17.5 keV neutron energy.

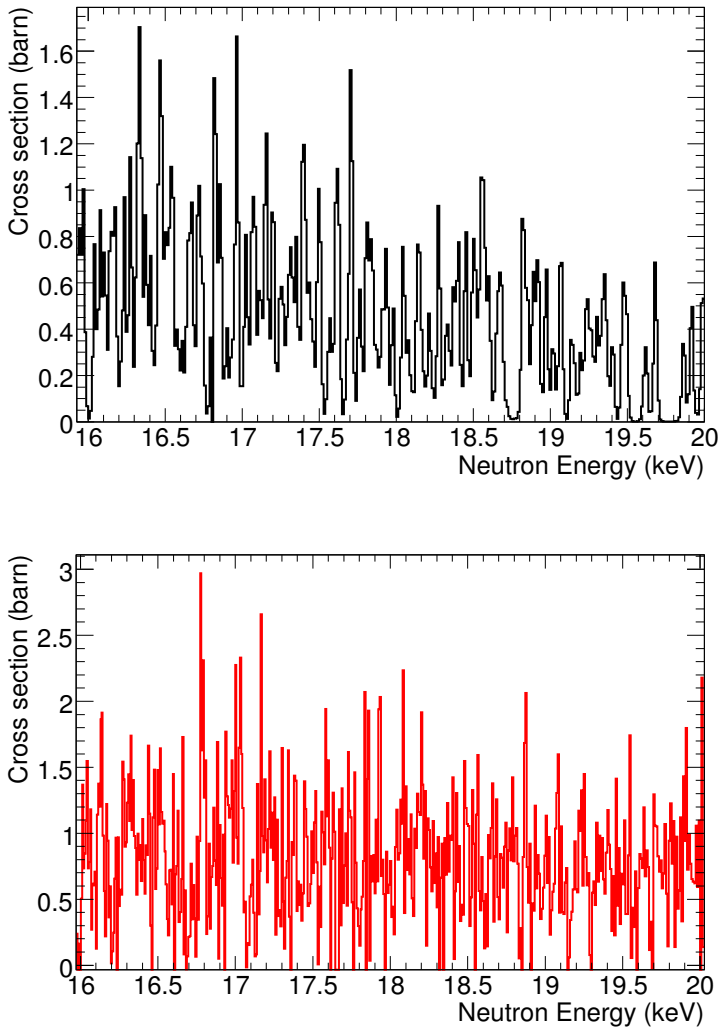

Figure 5.11: The same comparison as in Fig. 5.10 (top: simulation, bottom: experiment) but using a bin width of 7 eV, about 3 times smaller than the experimental resolution of 22 eV at 17.5 keV. This confirms that the cross section fluctuations are observed independently of the bin width, thus providing additional evidence for their real existence.

5.5 Summary and Conclusions

The neutron capture cross section of ^{197}Au has been measured at n_TOF over the wide energy range from 1 eV to 400 keV. Following a detailed resonance analysis [112], this work deals with the unresolved region starting at 5 keV. Based on a thorough study of the various background components and on the careful evaluation of the uncertainties, the cross section was derived with an accuracy of 3.9-6.7% on a grid of 20 bins per energy decade (Table 5.3). In the critical energy range below 200 keV the present results are in fair agreement with the standard evaluation, while being systematically higher by few percent than the time-of-flight measurement of Macklin *et al.* [109, 110].
MACSs from 5 to 100 keV have been extracted with an uncertainty from 3.1-3.6%. A comparison of the MACS at 30 keV shows good agreement with other experimental data and is 4.7% higher than the MACS determined in the activation study of Ratynski and Käppeler [34].
The structures in the ^{197}Au cross section have been investigated by simulation of the expected level density using average resonance properties deduced from the resolved resonance region. It could be shown that the experimental evidence for such structures was confirmed by the gross features of the simulated data. Accordingly, these structures are physically relevant and could be included in a future evaluation.
In light of the accuracy, the high energy resolution, and the wide energy range of the present results, it appears likely that the goal of establishing the ^{197}Au(n,γ) cross section as a standard in the keV region can soon be reached. The comparison with the most accurate previous data shows fair agreement within the actual uncertainties. Nevertheless, further efforts to resolve the remaining differences would be most welcome, either by current time-of-flight experiments at other facilities [125] or by additional activation studies [126] (see also Chapter 6). In this context, the recent implementation of the use of boron in the water moderator at n_TOF, which leads to a reduction of the in-beam γ background, also bear promising options for complementary improvements.

6 Definition of a standard neutron field with the ^{7}Li$(p,n)^7$Be reaction

6.1 Introduction

The ^{7}Li$(p,n)^7$Be reaction represents the most prolific neutron source in the keV region and has been extensively used in a large number of neutron cross section measurements, predominantly for nucleosynthesis studies in astrophysics but also as an independent check of important cross sections for technological applications.
With respect to astrophysics this reaction became particularly important because it can be used to mimic the stellar neutron spectrum for a thermal energy of $k_BT = 25$ keV [34], right in the temperature range between 250 and 300 MK, where stellar nucleosynthesis by the *s* process takes place [7, 127]. Due to this unique feature, MACSs can be measured directly by activation. Such measurements are important for establishing a complete and reliable set of MACSs data, which are the essential nuclear physics input of comprehensive model calculations characterizing the *s* process abundance component (see Sec. 1.4.1).
The possibility to simulate the stellar environment has been used in a large number of activation experiments (e.g. [128, 129]) covering the entire periodic table [17]. Simulations of quasi-stellar spectra have been also obtained for $k_BT = 5$ [36] and 52 keV [35] using the (p,n) reactions on ^{18}O and ^{3}H, but with significantly reduced intensities. All measurements with this technique were performed relative to the ^{197}Au(n,γ) cross section and rely on the verification of this "quasi-stellar" spectrum as well as on the fact that the gold cross section has been determined for this spectrum with an accuracy of 1.4% [34]. The results obtained with activation measurements in the quasi-stellar spectrum depend on a careful measurement of the induced activities, but also on the accurate definition of the neutron spectrum itself. The latter problem clearly affects also the value of the gold cross section measured in that spectrum and touches the question, whether the ^{197}Au(n,γ) cross section could be considered as a standard in such applications [130].
This work was intended to check and to solidify existing information [34, 131] concerning the quasi-stellar neutron field produced by the ^{7}Li$(p,n)^7$Be reaction at a proton energy of $E_p = 1912$ keV. In parallel, a very similar study has been performed by Feinberg *et al.* [126]. Measurement and data analysis are presented in Secs. 6.2 and 6.3. The results are presented in Sec. 6.4, and possible implications for the extension of the

gold standard cross section to the energy range below 200 keV are discussed in Sec. 6.5.

6.2 Measurement

The experiment was performed at the Ion Accelerator Facility (PIAF) at Physikalisch-Technische Bundesanstalt Braunschweig (PTB) [132]. The low-scatter facility for the production of neutron reference fields in open geometry was perfectly suited for the purpose of the present measurement and could be used without further modifications. The particular advantage of this facility (shown in the upper left corner of Fig. 6.1) is the large open pitch around the neutron target in the center. In this way background from scattered neutrons is reduced significantly.

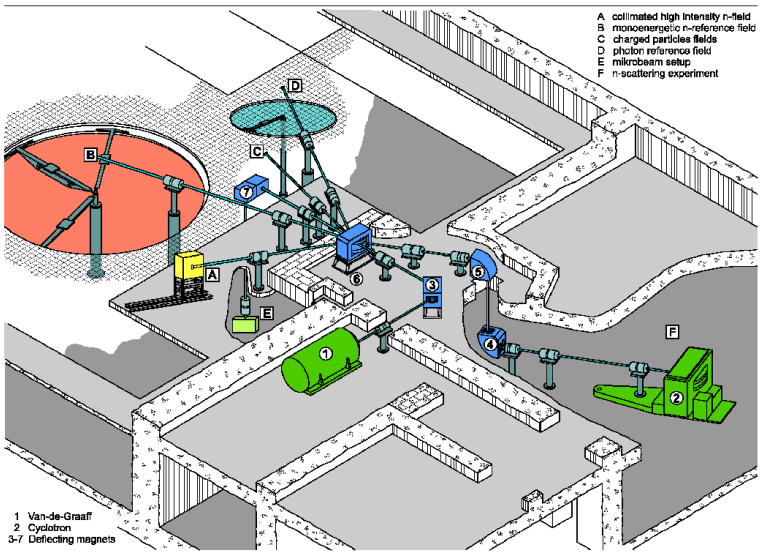

Figure 6.1: The Ion Accelerator Facility (PIAF) at PTB Braunschweig. The low-scatter facility for the production of neutron reference fields in the upper left corner is designed with an open pitch around the central neutron target to minimize background from scattered neutrons [133].

The proton beam for neutron production was delivered by the PTB pulsed 3.75 MV Van de Graaff accelerator with a repetition rate of 625 kHz, a nominal pulse width of 1.5 ns, a nominal energy of 1912±1.2 keV, and an average current of 0.5-0.8 μA. The lithium target in the center of the spectrometer (position B in Fig. 6.1) was prepared by vapour deposition of a metallic lithium layer 25 mm in diameter on a tantalum backing 0.5 mm in thickness. The target thickness of 10 μm (564 μg/cm^2) was sufficient to slow all protons down below the threshold of the ^{7}Li$(p,n)^7$Be reaction at 1881 keV for obtaining a reproducible and well defined neutron field.
The target was mounted on the beam line without breaking the vacuum to protect the Li

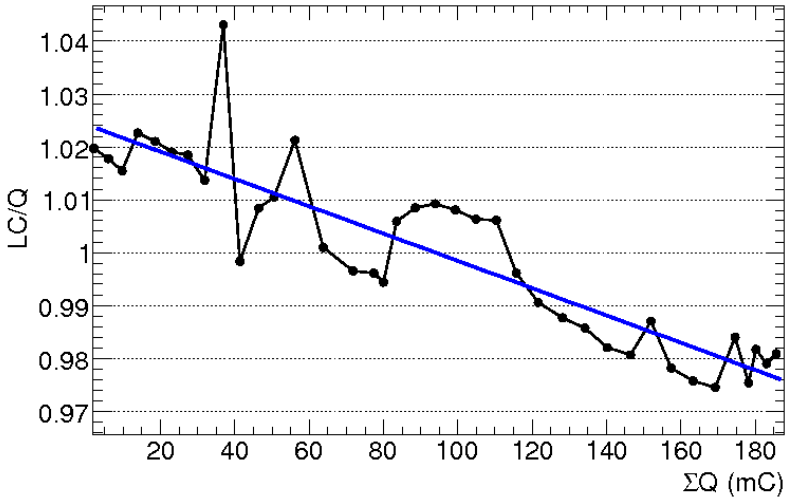

Figure 6.2: Ratio of the long counter readings (LC) and the accumulated beam charge (Q) for the individual runs as a function of the total accumulated beam charge (ΣQ). During the experiment a decrease of neutron yield by about 4.8% was observed due to target degradation. The data are fitted with a linear function $a_0 + a_1 \times \Sigma Q$.

layer from oxidation. To reduce the heat load to the lithium layer, the target was rotated during the measurements at a frequency of 1 rotation per second such that the beam spot described a circle about 6 mm in diameter. The target was cooled by a jet of cold air to avoid the moderating influence of cooling water. The neutron yield decreased almost linearly by only 4.8% during the four days of the experiment as indicated in Figure 6.2. A low-mass target assembly was used to minimize the effect of neutron scattering in the target surroundings.

Because the proton energy is chosen only 31 keV above the reaction threshold, the center-of-mass velocity of the ^{8}Be* produced in the reaction still exceeds the speed of the subsequently emitted neutrons. Accordingly, the resulting neutron field is restricted to a forward cone with 120° opening angle as sketched in Fig. 6.3.

Neutron spectra were recorded using a ^{6}Li-glass detector, which is a scintillation detector containing Li for converting neutrons to charged particles via the reaction $^6\mathrm{Li}(n,\alpha)^3\mathrm{H}$. The detector was mounted on the arm of the spectrometer B, that could be rotated around the neutron target in the center of an open pitch (upper left corner of Fig. 6.1). With the movable detector the angular range between 0° and 65° was covered in steps of 5°. The ^{6}Li-glass scintillator was 38.9 mm in diameter and 2.85 mm in thickness and had a density of 2.405 g/cm^3. The detector was directly coupled to the window of an XP2020 photomultiplier and covered with a light-weight can made of stainless steel. The entrance window of this can had a thickness of 0.25 mm. The neutron yield was

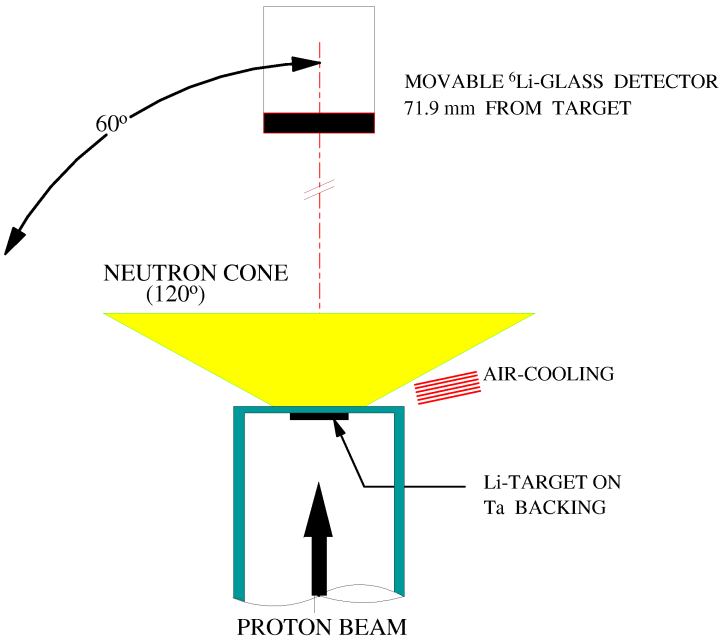

Figure 6.3: Schematic sketch of the experimental setup, showing the air-cooled Li target, the 0.5 mm thick Ta backing, and the forward peaked neutron field obtained with the ^{7}Li$(p,n)^7$Be reaction at E_p = 1912 keV [34]. Courtesy of F. Käppeler.

monitored throughout the entire experiment with a long counter, which is a detector based on a slow neutron detector (e.g. BF_3) inside a moderating medium. That way, a detection efficiency which is almost constant with neutron energy is achieved. The long counter was mounted at an angle of -17° about 6 m from the neutron target. The statistical uncertainties of the resulting normalization factors were negligibly small. The relative standard deviation of the individual long counter readings per unit beam charge was 0.8%, demonstrating the stability of the monitoring procedure (see Fig. 6.2). This figure shows also a slight decrease of 4.8% in neutron yield due to target degradation effects.
The data were accumulated in two-dimensional spectra consisting of 2048 time-of-flight versus 1024 pulse height channels. The total time resolution of the experiment was 3.0 ns FWHM which includes the time spread of the proton beam pulses and the time resolution of the ^{6}Li-glass detector.

In a first series of runs the ^{6}Li-glass detector was mounted at an effective flight path of 719 mm between the target and the center plane of the scintillator. Measuring times varied between about 1.5 h and 3 h to compensate for the decrease in intensity with increasing emission angle. The stability of the system was checked twice a day by reference measurements at 0°. In a second series of runs the flight path was reduced to

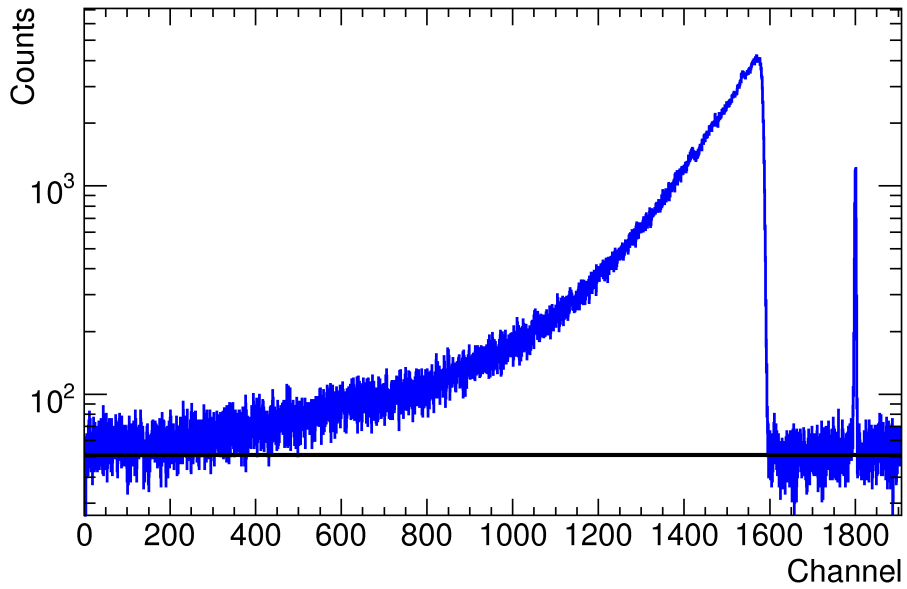

Figure 6.4: Time of flight spectrum taken at a flight path of 719 mm and a neutron angle of 25° relative to the direction of the proton beam. The full width at half maximum (FWHM) of the γ peak and the width of the time-of-flight channels were 3 ns and 0.83 ns, respectively. The flat background is defined in the region between γ peak and onset of the neutron distribution (channels 1800 and 1600).

369 mm. By using the same measuring times as before the signal/background ratio at the lower energy end of the spectrum could be considerably improved. The different flight paths were also useful to check whether the background in the time-of-flight spectra was really flat or whether corrections, for instance for in-scattering of neutrons, had to be considered. Such effects, which would give rise to inconsistencies in the spectral shapes, were also studied in dedicated background runs by using a blank target without any lithium. None of these tests showed detectable indications for hidden backgrounds (see below). Additional control runs were performed with targets, which consisted of LiF layers, of 565 and 550 μg/cm^2 in thickness, evaporated onto Ta and Ag backings, respectively.

The quality of the time-of-flight measurements is illustrated in Fig. 6.4, which shows the spectrum at 25° taken at a flight path of 719 mm. The 3.0 ns resolution in time-of-flight was determined by the sharp γ peak at channel 1800. The background level was reduced by setting a pulse height threshold in the minimum between neutron-induced signals and the low energy part of the distribution containing mostly low-energy γ events and electronic noise as illustrated in the pulse height spectrum of Fig. 6.5.

The repetition rate was low enough that corrections due to overlap of successive neutron

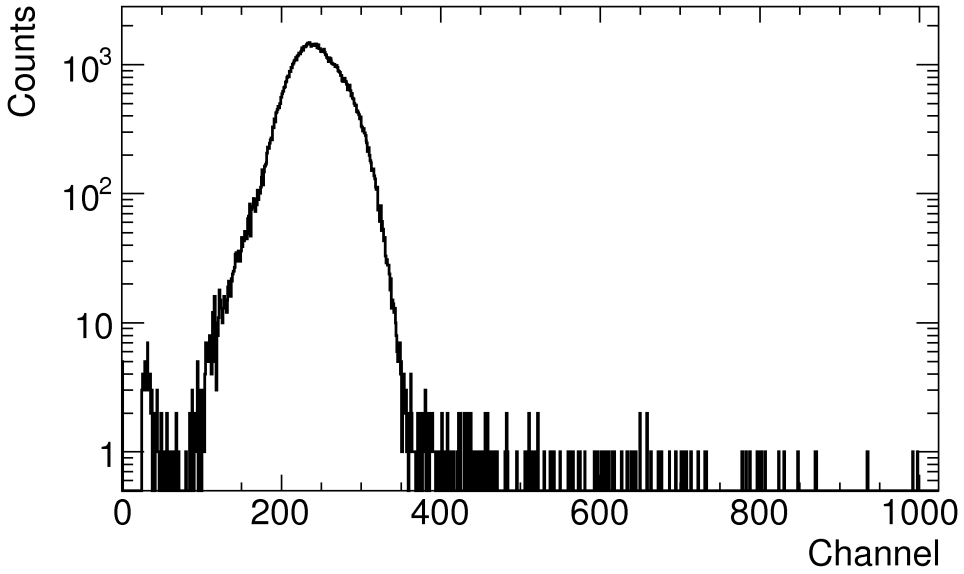

Figure 6.5: Pulse height spectrum showing the separation between neutron events and background. Most of the γ signals are suppressed by the pulse height threshold.

bursts were negligibly small. Therefore, a time-independent background was defined in the region between the γ peak and the onset of the neutron distribution (near channel 1600 in the example of Fig. 6.4). The assumption of a constant background was justified, because significant structure in the time-of-flight background underneath the neutron distribution in Fig. 6.4 would have caused corresponding differences in the neutron spectra measured at 719 and 369 mm.

6.3 Data analysis

A dead-time correction was applied by means of the real and live time ratio determined by the data acquisition system. This correction was never exceeding 1% and had negligible impact on the data. The flat background defined in the region between γ peak and onset of neutron events was subtracted.
At larger angles, intensities are decreasing and the maximum neutron energy is expected to decrease as well. The time-of-flight spectra acquired in this angular range were found to show a feature on the high energy side, independent of the angle. This background component, which was attributed to neutron scattering in the target, could be determined by the spectrum at 65°, where the detector was already outside of the direct neutron beam. The effect is illustrated in Fig. 6.6 by comparison of the 55° and 65° spectra taken at a flight path of 719 mm. This scattering background was eliminated

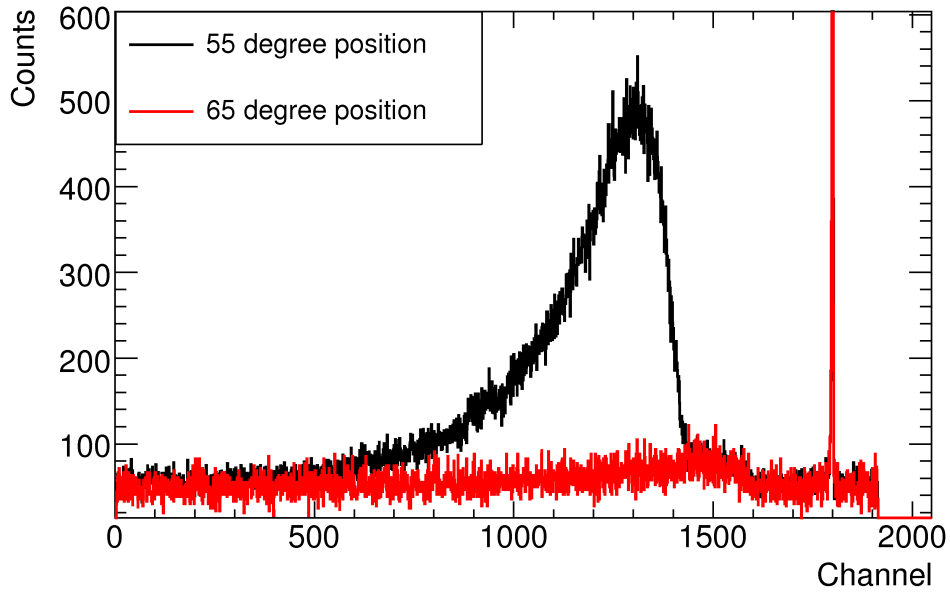

Figure 6.6: Time-of-flight spectra taken at 55° and 65°. The 65° spectrum, where the detector was already outside the direct neutron beam (lower red curve), was used for correcting the background due to neutrons scattered in the target backing. The 65° and 55° spectra shown in the figure were measured at a flight path of 719 mm.

by subtraction of the 65° spectrum (scaled for the respective fluence).
After transformation to an energy grid the histograms were rebinned in the region from 0 to 120 keV with bin widths of 0.5 and 1 keV, respectively. The uncertainty of the background and dead-time corrected spectrum per bin is

$$\sigma = \sqrt{\left(\frac{C}{\sqrt{C'}}\right)^2 + \sigma_{\mathrm{bg}}^2} \tag{6.1}$$

where C refers to the dead-time corrected spectrum without background subtraction, C' to the raw spectrum, and σ_{bg} denotes the uncertainty of the background components due to neutron scattering in the experimental area (flat background) and due to neutron scattering in the target.
The efficiency of the ^{6}Li-glass detector is essentially determined by the cross section of the $^{6}\mathrm{Li}(n,\alpha)^{3}\mathrm{H}$ reaction. However, after conversion of the time-of-flight spectra to a neutron energy scale, structures appeared at 28 and 55 keV, which could be attributed to the 27.8 keV and 55.67 keV resonances in ^{56}Fe and ^{28}Si, respectively. These features are clearly visible in the reference spectra taken at 0°, which were acquired in regular

intervals to verify the stability of the system (Fig. 6.7). The effect of structural materials in the setup has, therefore, been considered by means of Monte Carlo simulations using a detailed model of the detector as input for the code GEANT3[1] [116]. The simulated efficiency is compared in Fig. 6.8 with the respective curve based only on the $^6Li(n,\alpha)^3H$ cross section [42].

To obtain the angle integrated neutron spectrum, each spectrum has been scaled by

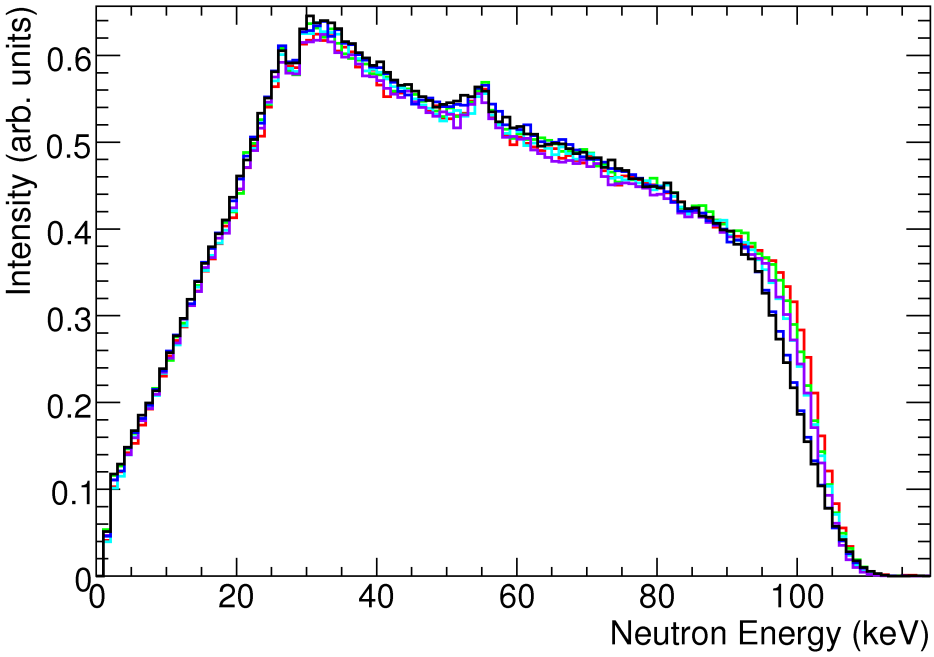

Figure 6.7: Reference runs recorded in regular intervals throughout the experiment. The loss of high energy neutrons observed in later runs is due to target degradation effects. Most likely, thin carbon layers were deposited on the target surface which reduced the energy of the protons entering the lithium layer.

the respective solid angle. For angles $\alpha > 0°$ the corresponding factors

$$f_\alpha = (\cos(\alpha - 2.5°) - \cos(\alpha + 2.5°))/(1 - \cos(60° + 2.5°)), \tag{6.2}$$

and for the 0° position

$$f_0 = (1 - \cos(2.5°))/(1 - \cos(60° + 2.5°)) \tag{6.3}$$

are listed in Table 6.1. Fig. 6.9 presents a comparison of the neutron spectra at 0°, which were measured in subsequent runs at the two flight paths of 719 and 369 mm.

[1]The simulation has been performed by co-authors of the article [I2].

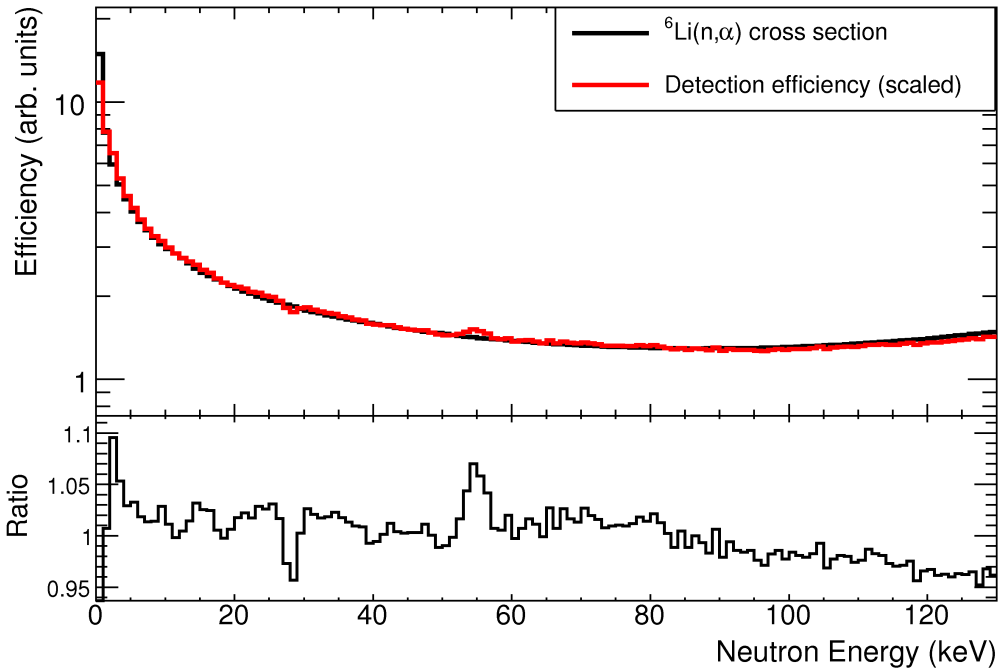

Figure 6.8: Monte Carlo simulation of the detector efficiency with the GEANT3 code compared to the efficiency exclusively based on the ^{6}Li$(n,\alpha)^3$H cross section. The ratio of the two curves is shown in the lower panel.

The spectra are in very good agreement, apart from small differences at the high energy part, which are due to the different broadening by the time resolution. This consistency justifies the assumption of a flat background in the time-of-flight spectra mentioned before.

Table 6.1: Scaling factors considering the solid angle of the individual angular positions.

Angle	0°	5°	10°	15°	20°	25°	30°
f_α	0.00177	0.01413	0.02815	0.04195	0.05543	0.06850	0.08104
Angle		35°	40°	45°	50°	55°	60°
f_α		0.09296	0.10418	0.11461	0.12416	0.13277	0.14036

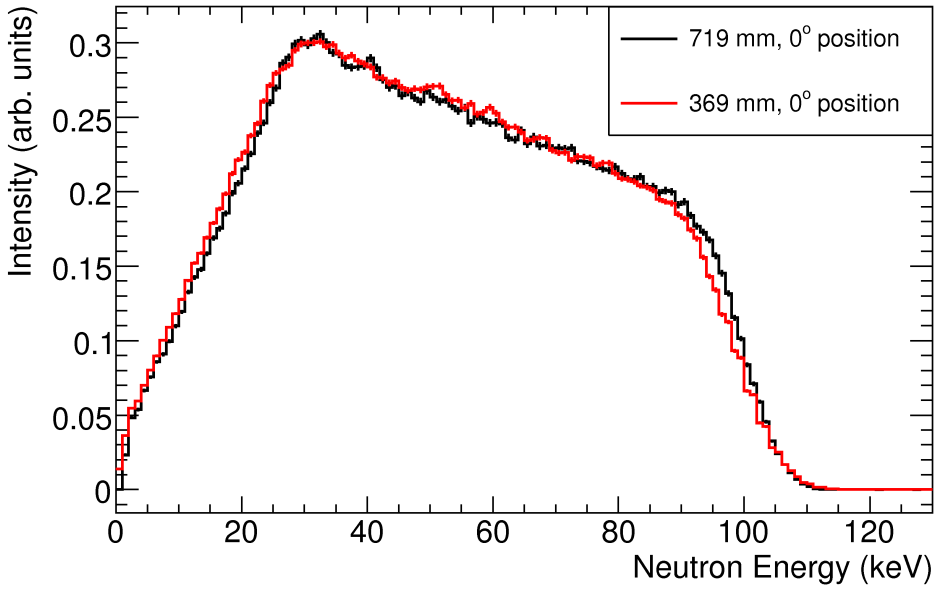

Figure 6.9: Comparison of the neutron spectra taken at 0° at flight paths of 369 cm and 719 mm. The very good agreement justifies the assumption of a flat time-of-flight background in data analysis.

6.4 Results

The spectra for the measured emission angles for a flight path of 719 mm are plotted in Fig. 6.10. The highest intensity part of the integrated spectrum is contributed by the angular range from 25° to 45°. Numerical values of all spectra can be found in Appendix B. The spectrum is given in Table 6.2 with a bin width of 0.5 keV and 1 keV below and above 10 keV, respectively. Above 40 keV the bin width is smaller than the neutron energy resolution of the experiment, which is reaching 4% at 100 keV. The smallest accessible energy is determined by the repetition rate of the accelerator and was 1.2 keV for the 719 mm flight path. The energy range could be extended down to 0.3 keV by normalizing the spectrum obtained at the shorter flight path in the energy range between 1.5 and 3.5 keV. This affects only the first three entries in Table 6.2.

The values of N_E for the angle-integrated neutron spectrum are listed in Table 6.2 together with their statistical uncertainties. Additional systematic uncertainties of 2.9% are due to the simulated detection efficiency including the contribution by the ^{6}Li$(n,\alpha)^3$H cross section, and due to the scaling factors f_α. The 0.8% uncertainty of the neutron fluence provided by the long counter (Sec. 6.2) has a negligible impact on the total systematic uncertainty.
The ^{6}Li$(n,\alpha)^3$H cross section is specified with an accuracy ranging from 0.14% at 1

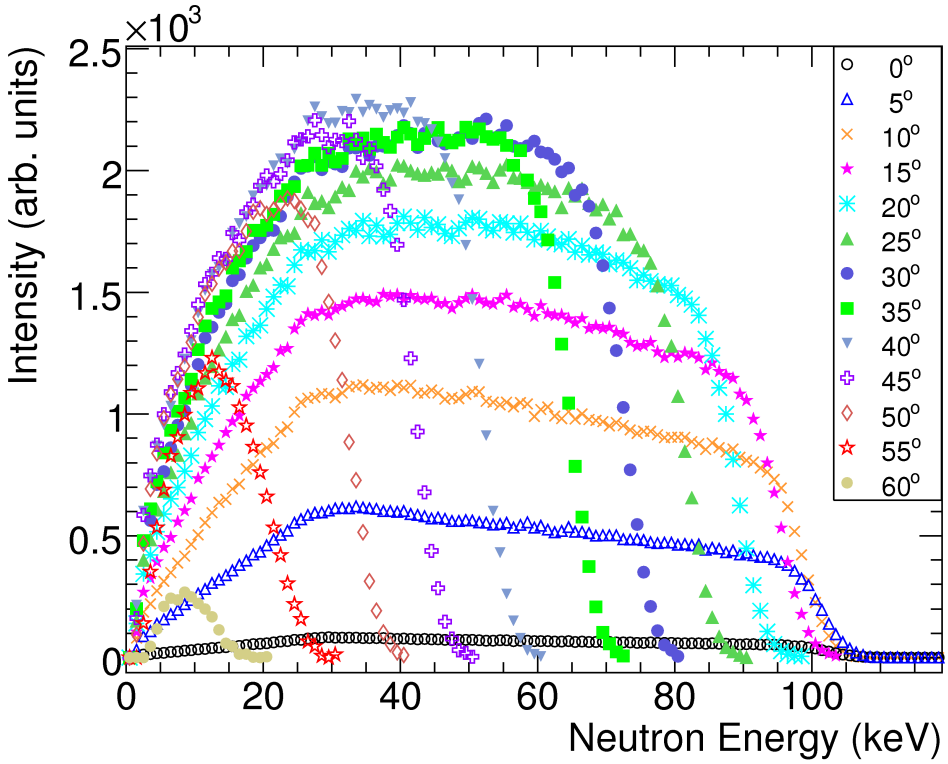

Figure 6.10: Neutron spectra from 0° to 60° in steps of 5° for a flight path of 719 mm. Spectra are corrected for the respective solid angle.

keV to 0.4% at 120 keV [42]. A detection efficiency proportional to the ^{6}Li(n,α) standard cross section deviates between −5% to +5% from the realistic detection efficiency determined by the GEANT3 simulations as shown in Fig. 6.8. Assuming a 20% uncertainty of the respective corrections including the contribution by the ^{6}Li$(n,\alpha)^3$H cross section, yields a total uncertainty of 2% for the detection efficiency.
The scaling factors f_α were calculated for the geometry of the setup and the measurement. For the longer flight path only about 2/3 of the respective solid angle was covered by the ^{6}Li glass detector, whereas the detector was slightly overlapping the angular positions at the shorter flight path. The resulting differences are most pronounced in the spectra at 55° and 60° and leads to somewhat broader distributions for the shorter flight path as shown in Fig. 6.11. However, these differences are barely visible in forward direction (Fig. 6.9), presumably because the distribution is also slightly broadened by the extended beam spot, which was about 3 mm in diameter. In summary, the angle-integrated spectrum is only marginally affected by the experimental coverage of the solid angle. Accordingly, the contribution of the scaling factors f_α to the uncertainty of

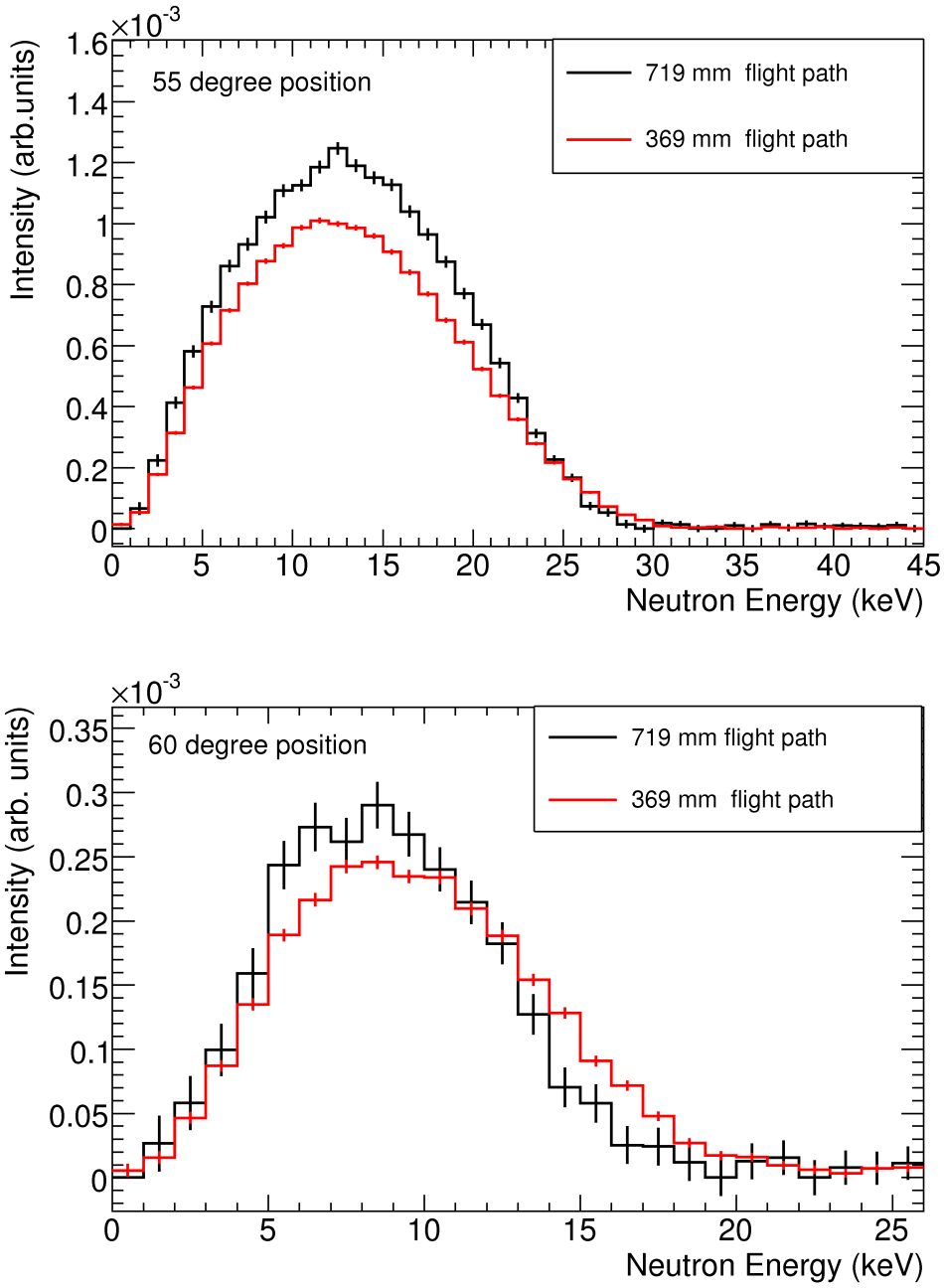

Figure 6.11: Comparison of the spectra recorded at an angular position of 55° (top) and 60° (bottom) for the two different flight paths to illustrate the broadening effect due to the different coverage of the solid angle at flight paths of 719 and 369 mm.

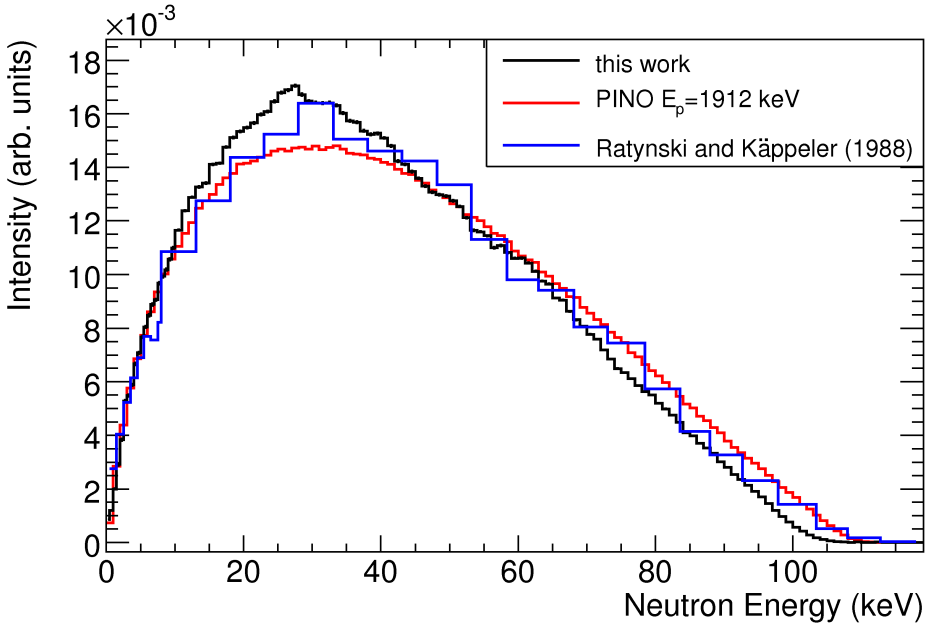

Figure 6.12: Angle-integrated spectrum compared to the histogram reported by Ratynski and Käppeler [34] and a calculation using the code PINO.

N_E is less than 2%.
In Fig. 6.12, the present quasi-stellar spectrum is compared with the histogram of Ratynski and Käppeler [34] and with an example for a calculated spectrum using the code PINO [134], which generates spectra for the ^{7}Li$(p,n)^7$Be reaction (http://exp-astro.physik.uni-frankfurt.de/pino/). An alternative, less specialized code for neutron spectrum calculations is DROSG-2000 (http://www-nds.iaea.org/drosg2000.html). The spectra in Fig. 6.12 are normalized to unit area. In general there is good agreement for the spectra in Fig. 6.12. The difference between the present results and the PINO calculation indicates that the proton energy in the experiment was around 1910 keV rather than the nominal 1912 keV. In particular the high-energy tail of the distribution is a very sensitive indicator of the highest proton energies in the lithium layer. The deviation of the experimental and the nominal proton energy can be due to the calibration of the voltage stabilization system of the Van de Graaff accelerator or due to a small energy loss in a thin additional layer on top of the lithium layer.
A follow-up code of PINO, which includes also angular distribution in the entrance and exit channel, is called n17 and is currently under development [135]. First results are presented in Fig. 6.13, which illustrates a comparison of the measured angular spectra with a simulation assuming proton energies of 1909 and 1910 keV[2]. The small struc-

[2]The calculation of the spectra has been performed by co-authors of the article [I2].

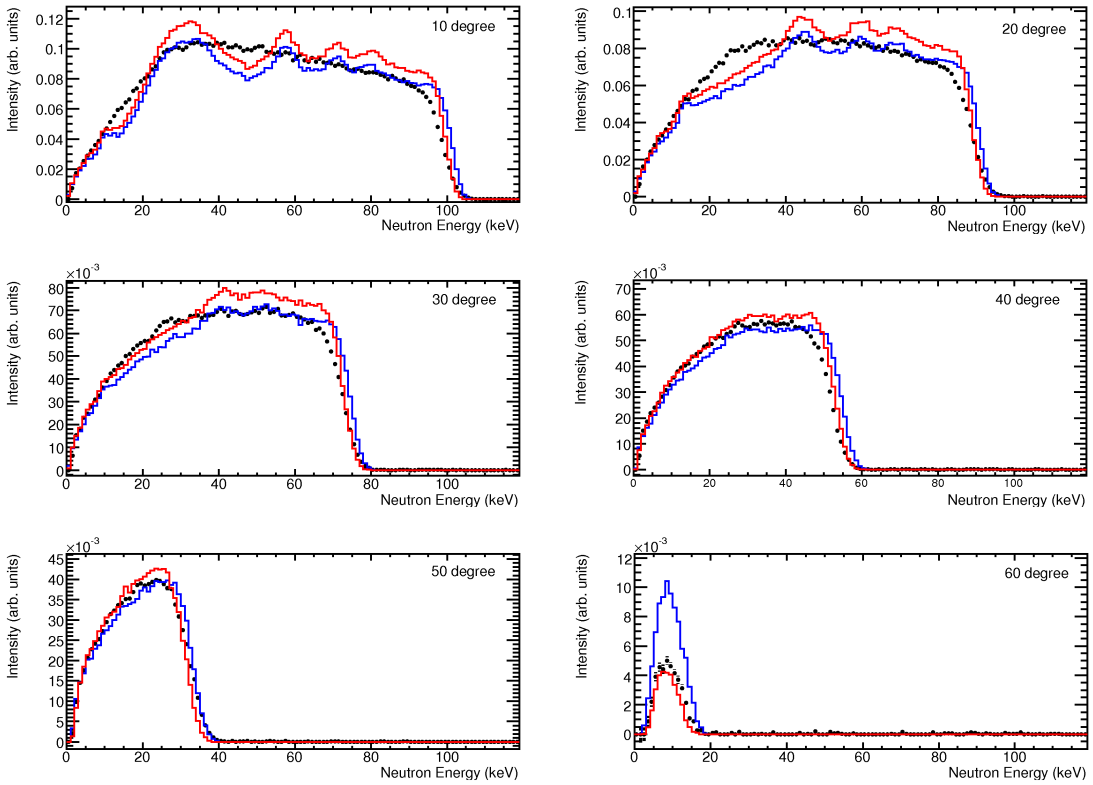

Figure 6.13: Measured angular spectra at a flight path of 719 mm (black dots) compared to calculations using a proton energy of 1909 keV (red) and 1910 keV (blue).

tures in the neutron distribution at medium energies are the result of the numerical interpolation of remaining uncertainties in the ^{7}Li(p,n) cross section very close to the threshold.
The deviation of the proton energy from the nominal energy of 1912 keV is still compatible with the uncertainty quoted for the energy calibration of the accelerator. A similar but less pronounced difference is seen with respect to the spectrum in Ref. [34], which confirms the small mismatch of the proton energy in the present data.

6.5 Implications for the (n,γ) cross section of ^{197}Au

Standard and reference cross sections play a key role in cross section measurements of neutron-induced reactions. The criteria for cross section standards are (i) that they are smoothly varying with neutron energy, i.e. that their values depend only slightly on experimental resolution, (ii) that they are convenient to use in measurements, and (iii) that they have been determined by absolute techniques and with high accuracy of

1-3%. So far, the (n,γ) cross section of ^{197}Au is recommended as a standard at thermal neutron energies and between 0.2 and 2.5 MeV [136].
Reference cross sections are cases which are particularly useful for specific measurements, but do not meet all criteria of a standard, i.e. because of fluctuations with neutron energy due to overlapping resonances. The neutron capture cross section of ^{197}Au represents such an example. Apart from cross section fluctuations below about 20 keV, there are a number of attractive features, which make it desirable to extend the energy range, where the ^{197}Au(n,γ) cross section could be used as a standard. Gold is an element with a single stable isotope, it is easily available in large amounts and with high purity, and has a conveniently large capture cross section.
For these reasons gold has already been used as a reference in numerous (n,γ) cross section measurements at keV neutron energies. This holds in particular for applications in nuclear astrophysics [17], where the capture cross sections of the stable isotopes between ^{12}C and ^{209}Bi represent the key ingredients for describing stellar nucleosynthesis by the *s* process between Fe and Bi.

The present measurement of the quasi-stellar spectrum for $k_BT = 25$ keV confirms the definition of the neutron field used in Ref. [34], thus supporting the accurate absolute capture cross section obtained in that activation experiment. In this context it is particularly important that the slight mismatch in proton energy has only a very small effect on the gold cross section. This is demonstrated by calculating the spectrum averaged (n,γ) cross section of Au using the evaluated Au cross section from the ENDF/B-VII library [96]. The results are 627.7 mb and 632.6 mb for the present spectrum and for that of Ref. [34], respectively. Using spectra calculated with PINO at proton energies of 1909 keV and 1912 keV, one finds a difference of 1.8% for the spectrum averaged cross section, still compatible with the 1.4% uncertainty claimed for the gold cross section in the quasi-stellar spectrum. In summary, the present results could be considered as important steps for establishing the gold cross section as a capture standard below the present limit of 200 keV.
Recent time-of-flight measurements at the n_TOF facility at CERN (Chapter 5) lead to a somewhat higher but within uncertainties still compatible spectrum averaged cross section, more consistent with the ENDF/B-VII library, which is about 5.5% higher than the result of Ref. [34]. Similar results have been reported from GELINA in Geel [137, 138]. The ENDF/B-VII compilation of the gold cross section in the keV region relies mostly on the high-resolution time-of-flight data from Macklin [110] and on additional information from a variety of measurements in narrower energy regions (for a summary see Ref. [136]). Whether the differences between activation and time-of-flight measurements can be attributed to possible uncertainties of the prompt γ-ray technique, i.e. to variations of the capture γ-ray spectrum with neutron energy, or to enhanced internal conversion effects in the capture γ cascades of ^{197}Au [139] needs to be clarified and will be crucial for accepting the (n,γ) cross section of ^{197}Au as a capture standard for the keV region.

Table 6.2: Angle-integrated neutron spectrum obtained from the ^{7}Li$(p,n)^7$Be reaction at 1910±1.2 keV proton energy (derived from the measured time-of-flight spectra). Uncertainties given are statistical. The systematic uncertainty is 2.9%.

E_n (keV)	N_E ($\times 10^{-6}$)	E_n (keV)	N_E ($\times 10^{-6}$)	E_n(keV)	N_E($\times 10^{-6}$)
0.3 - 0.5	863 ± 24	31 - 32	16397 ± 71	72 - 73	7185 ± 47
0.5 - 1.0	1204 ± 34	32 - 33	16416 ± 72	73 - 74	6843 ± 46
1.0 - 1.5	1994 ± 56	33 - 34	16316 ± 72	74 - 75	6488 ± 44
1.5 - 2.0	2913 ± 86	34 - 35	16024 ± 72	75 - 76	6341 ± 43
2.0 - 2.5	3836 ± 79	35 - 36	15734 ± 72	76 - 77	6116 ± 42
2.5 - 3.0	5284 ± 74	36 - 37	15686 ± 72	77 - 78	5852 ± 42
3.0 - 3.5	5484 ± 76	37 - 38	15360 ± 71	78 - 79	5640 ± 40
3.5 - 4.0	5889 ± 76	38 - 39	15233 ± 71	79 - 80	5504 ± 40
4.0 - 4.5	6672 ± 77	39 - 40	15269 ± 72	80 - 81	5195 ± 38
4.5 - 5.0	7083 ± 75	40 - 41	15097 ± 72	81 - 82	4990 ± 37
5.0 - 5.5	7671 ± 75	41 - 42	14801 ± 71	82 - 83	4753 ± 36
5.5 - 6.0	8049 ± 75	42 - 43	14232 ± 69	83 - 84	4481 ± 35
6.0 - 6.5	8484 ± 77	43 - 44	14113 ± 69	84 - 85	4096 ± 34
6.5 - 7.0	8883 ± 77	44 - 45	13846 ± 69	85 - 86	3982 ± 34
7.0 - 7.5	9055 ± 78	45 - 46	13589 ± 68	86 - 87	3712 ± 32
7.5 - 8.0	9680 ± 79	46 - 47	13304 ± 67	87 - 88	3525 ± 30
8.0 - 8.5	9930 ± 79	47 - 48	13082 ± 66	88 - 89	3339 ± 29
8.5 - 9.0	10187 ± 79	48 - 49	12979 ± 66	89 - 90	3019 ± 27
9.0 - 9.5	10567 ± 79	49 - 50	12934 ± 66	90 - 91	2799 ± 27
9.5 - 10.0	10995 ± 79	50 - 51	12746 ± 66	91 - 92	2541 ± 26
10 - 11	11657 ± 57	51 - 52	12537 ± 65	92 - 93	2348 ± 25
11 - 12	12385 ± 59	52 - 53	12116 ± 63	93 - 94	2133 ± 23
12 - 13	12890 ± 60	53 - 54	11651 ± 60	94 - 95	1917 ± 22
13 - 14	13269 ± 60	54 - 55	11591 ± 60	95 - 96	1696 ± 21
14 - 15	13415 ± 61	55 - 56	11451 ± 60	96 - 97	1454 ± 21
15 - 16	14113 ± 62	56 - 57	11005 ± 59	97 - 98	1200 ± 19
16 - 17	14154 ± 63	57 - 58	11088 ± 60	98 - 99	977 ± 17
17 - 18	14765 ± 65	58 - 59	10819 ± 60	99 - 100	762 ± 16
18 - 19	15120 ± 66	59 - 60	10607 ± 59	100 - 101	561 ± 16
19 - 20	15337 ± 67	60 - 61	10616 ± 60	101 - 102	415 ± 14
20 - 21	15482 ± 67	61 - 62	10425 ± 58	102 - 103	276 ± 14
21 - 22	15657 ± 67	62 - 63	10122 ± 57	103 - 104	173 ± 13
22 - 23	15977 ± 68	63 - 64	9760 ± 56	104 - 105	108 ± 13
23 - 24	16083 ± 68	64 - 65	9650 ± 56	105 - 106	64 ± 13
24 - 25	16465 ± 69	65 - 66	9126 ± 53	106 - 107	39 ± 13
25 - 26	16787 ± 70	66 - 67	9047 ± 54	107 - 108	20 ± 12
26 - 27	16888 ± 72	67 - 68	8623 ± 52	108 - 109	9^{+13}_{-9}
27 - 28	17045 ± 74	68 - 69	8313 ± 51	109 - 110	10^{+11}_{-10}
28 - 29	16715 ± 75	69 - 70	8082 ± 50	110 - 111	8^{+12}_{-8}
29 - 30	16467 ± 73	70 - 71	7764 ± 48	111 - 112	4^{+12}_{-4}
30 - 31	16414 ± 71	71 - 72	7592 ± 48	112 - 113	12 ± 12

Appendix A

^{62}Ni sample

The ^{62}Ni sample used in this measurement was purchased from ISOFLEX USA[3]. The sample was delivered in the form of a metallic powder with an enrichment of 97.95% in ^{62}Ni and 2000 mg in mass. To prepare it for measurement at n_TOF the powder was pressed into a stable pellet of cylindrical form at the *Institut für Chemische Technologien und Analytik* of the Technical University of Vienna. The isotopic composition and chemical admixtures quoted by ISOFLEX are given in Tables 6.3 and 6.4.

Table 6.3: Isotopic composition of the ^{62}Ni sample

Isotope	^{58}Ni	^{60}Ni	^{61}Ni	^{62}Ni	^{64}Ni
Content (at%)	0.005	0.035	0.91	97.95	1.1

Table 6.4: Chemical admixture of the ^{62}Ni sample

Isotope	C	Mg	Al	Si	S	Ti	Cr	Mn	Fe	Co	Cu	Zn	Pb
Content (ppm)	49	5	25	30	11	< 3	< 3	< 3	10	30	< 3	15	50

^{63}Ni sample

The sample, which was obtained from Technical University of Munich (TUM) consisted originally of 3 Ni foils. Foils no. 1 and 2 were bought from New England Nuclear Boston (initially 669 mg Ni with 11.9% enrichment in ^{63}Ni) for a PhD thesis [140]. Foil no. 3 was produced by irradiating a Ni foil, 784 mg in mass and enriched by 98% in ^{62}Ni, at the thermal reactor of ILL Grenoble. This work was performed in the course of a PhD thesis [141] about Mössbauer-spectroscopy where all 3 Ni foils were used.

Since the samples were produced around 1984 (foil 1 and 2) and in 1992 (foil 3),

[3] www.isoflex.com

Table 6.5: Composition of the ^{63}Ni sample at the time of production, before and after the Cu separation. The composition is calculated based on the total masses, the activity and the enrichment of the original foils as quoted in [141].

Date	Dec 31, 1992			Feb 7, 2011			After separation
Sample	foil 1 and 2	foil 3		foil 1 and 2	foil 3		All foils
Mass (mg)	347.0	655.0		347.0	655.0		919.0
^{62}Ni mass (mg)	300.9	549.4		300.9	549.4		779.8
^{63}Ni mass (mg)	39.2	92.5		34.6	81.7		106.7
^{63}Cu mass (mg)	-	-		4.6	10.8		< 0.01

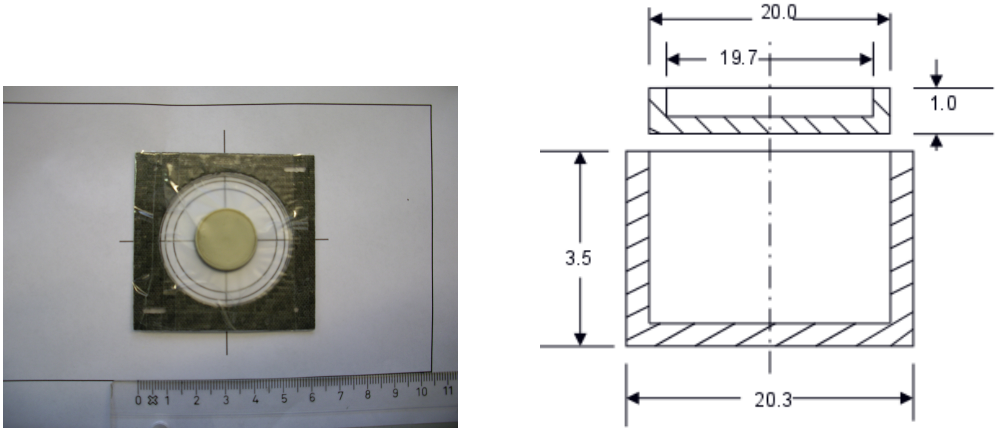

Figure 6.14: (left) Photo of the ^{63}Ni sample on the sample holder that was measured at n_TOF. (right) Schematic sketch of the PEEK canning for the NiO powder. Figure is not to scale. Courtesy of F. Käppeler.

already around 10% of the decay product ^{63}Cu accumulated with respect to ^{63}Ni. To avoid additional background by neutron capture on ^{63}Cu, which has a large capture cross section, a chemical pretreatment was performed by D. Schumann and co-workers at the *Paul Scherrer Institut* (PSI) to remove Cu from the sample. Due to the chemical processing, the sample was transformed to a NiO powder with grain sizes between 0.1 mm and 1.5 mm. Table 6.5 lists the sample composition in 1992 based on the activities given in Reference [141], compared to the calculated initial composition in 2011 and the composition after the chemical separation. A detailed isotopic analysis of the chemically pretreated sample is underway [105]. It turned out that it was not possible to press this powder into a stable pellet without adding a big amount of graphite, which would have introduces an additional background component in the measurement. Therefore, a thin PEEK ($C_{20}H_{12}O_3$) container for the NiO powder was produced at Karlsruhe Institute of Technology with the aim of reducing the additional material in the neutron beam

to a minimum. All elements present in PEEK are favorable for these kind of measurements since neutron capture cross sections are small and don't show resonances in the energy range of interest. A sketch of the sample including the sample holder is shown in Fig. 6.14.

Appendix B

The individual angular spectra with statistical uncertainties are listed in the following tables. They have been scaled for their solid angle. Data are given for the same binning and energy range as for the summed spectrum in Table 6.2.

Table 6.6: 0° position

E_n (keV)	N_E ($\times 10^{-6}$)	σ ($\times 10^{-6}$)	E_n (keV)	N_E ($\times 10^{-6}$)	σ ($\times 10^{-6}$)	E_n (keV)	N_E ($\times 10^{-6}$)	σ ($\times 10^{-6}$)
0.3 - 0.5	3.4	0.1	31 - 32	81.7	0.8	72 - 73	60.9	0.8
0.5 - 1.0	6.3	0.2	32 - 33	81.7	0.8	73 - 74	61.0	0.8
1.0 - 1.5	9.1	0.3	33 - 34	81.9	0.8	74 - 75	59.5	0.8
1.5 - 2.0	8.4	0.6	34 - 35	80.2	0.8	75 - 76	60.0	0.8
2.0 - 2.5	11.2	0.5	35 - 36	79.7	0.8	76 - 77	61.6	0.8
2.5 - 3.0	14.1	0.5	36 - 37	79.7	0.8	77 - 78	60.2	0.8
3.0 - 3.5	14.3	0.5	37 - 38	78.8	0.8	78 - 79	59.4	0.8
3.5 - 4.0	15.0	0.5	38 - 39	76.8	0.8	79 - 80	59.3	0.8
4.0 - 4.5	17.2	0.5	39 - 40	76.6	0.8	80 - 81	58.3	0.8
4.5 - 5.0	18.5	0.5	40 - 41	77.1	0.8	81 - 82	58.4	0.8
5.0 - 5.5	19.2	0.5	41 - 42	76.2	0.8	82 - 83	58.5	0.8
5.5 - 6.0	20.8	0.5	42 - 43	73.8	0.8	83 - 84	58.8	0.8
6.0 - 6.5	22.4	0.6	43 - 44	75.4	0.8	84 - 85	57.0	0.8
6.5 - 7.0	23.7	0.6	44 - 45	73.9	0.8	85 - 86	57.3	0.8
7.0 - 7.5	24.6	0.6	45 - 46	74.2	0.8	86 - 87	56.9	0.8
7.5 - 8.0	25.6	0.6	46 - 47	72.1	0.8	87 - 88	55.6	0.7
8.0 - 8.5	27.0	0.6	47 - 48	71.1	0.8	88 - 89	54.7	0.7
8.5 - 9.0	28.6	0.6	48 - 49	72.3	0.8	89 - 90	53.3	0.7
9.0 - 9.5	29.0	0.6	49 - 50	72.1	0.8	90 - 91	54.8	0.7
9.5 - 10.0	30.3	0.6	50 - 51	72.1	0.8	91 - 92	53.9	0.7
10 - 11	33.2	0.4	51 - 52	71.0	0.8	92 - 93	52.8	0.7
11 - 12	35.5	0.5	52 - 53	68.3	0.8	93 - 94	52.1	0.7
12 - 13	38.9	0.5	53 - 54	69.3	0.8	94 - 95	52.3	0.7
13 - 14	40.8	0.5	54 - 55	70.2	0.8	95 - 96	50.7	0.7
14 - 15	42.4	0.5	55 - 56	70.1	0.8	96 - 97	49.3	0.7
15 - 16	45.6	0.5	56 - 57	67.5	0.8	97 - 98	46.1	0.7
16 - 17	47.1	0.5	57 - 58	68.9	0.8	98 - 99	44.9	0.7
17 - 18	51.2	0.6	58 - 59	68.5	0.8	99 - 100	41.2	0.6
18 - 19	53.8	0.6	59 - 60	66.6	0.8	100 - 101	36.1	0.6
19 - 20	56.0	0.6	60 - 61	67.1	0.8	101 - 102	29.9	0.5
20 - 21	58.8	0.6	61 - 62	66.5	0.8	102 - 103	24.8	0.5
21 - 22	61.6	0.6	62 - 63	64.9	0.8	103 - 104	17.6	0.4
22 - 23	64.5	0.7	63 - 64	65.2	0.8	104 - 105	12.7	0.3
23 - 24	67.0	0.7	64 - 65	66.4	0.8	105 - 106	8.6	0.3
24 - 25	71.7	0.7	65 - 66	64.1	0.8	106 - 107	5.4	0.2
25 - 26	73.0	0.7	66 - 67	65.5	0.8	107 - 108	3.0	0.2
26 - 27	77.4	0.8	67 - 68	64.0	0.8	108 - 109	1.4	0.1
27 - 28	79.0	0.8	68 - 69	64.2	0.8	109 - 110	0.7	0.1
28 - 29	81.8	0.8	69 - 70	63.5	0.8	110 - 111	0.3	0.1
29 - 30	82.9	0.8	70 - 71	62.8	0.8	111 - 112	0.1	0.1
30 - 31	81.6	0.8	71 - 72	61.4	0.8	112 - 113	0.0	0.1

Table 6.7: 5° position

E_n (keV)	N_E ($\times 10^{-6}$)	σ ($\times 10^{-6}$)	E_n (keV)	N_E ($\times 10^{-6}$)	σ ($\times 10^{-6}$)	E_n (keV)	N_E ($\times 10^{-6}$)	σ ($\times 10^{-6}$)
0.3 - 0.5	26.6	0.7	31 - 32	609.7	6.6	72 - 73	482.5	6.5
0.5 - 1.0	47.8	1.3	32 - 33	608.8	6.6	73 - 74	480.8	6.5
1.0 - 1.5	73.3	2.1	33 - 34	617.9	6.7	74 - 75	481.9	6.5
1.5 - 2.0	60.3	4.7	34 - 35	612.4	6.7	75 - 76	479.2	6.5
2.0 - 2.5	73.8	4.3	35 - 36	607.8	6.7	76 - 77	470.5	6.4
2.5 - 3.0	110.3	4.2	36 - 37	607.4	6.8	77 - 78	467.2	6.4
3.0 - 3.5	108.9	4.3	37 - 38	598.1	6.8	78 - 79	468.7	6.4
3.5 - 4.0	116.3	4.3	38 - 39	597.7	6.8	79 - 80	468.7	6.4
4.0 - 4.5	137.4	4.4	39 - 40	594.6	6.8	80 - 81	459.2	6.3
4.5 - 5.0	144.1	4.3	40 - 41	597.0	6.9	81 - 82	463.0	6.4
5.0 - 5.5	151.8	4.3	41 - 42	585.8	6.8	82 - 83	457.9	6.4
5.5 - 6.0	165.3	4.4	42 - 43	581.3	6.8	83 - 84	462.0	6.4
6.0 - 6.5	175.3	4.6	43 - 44	575.7	6.8	84 - 85	440.3	6.2
6.5 - 7.0	182.6	4.6	44 - 45	568.5	6.8	85 - 86	446.5	6.3
7.0 - 7.5	189.1	4.6	45 - 46	571.9	6.8	86 - 87	444.2	6.3
7.5 - 8.0	205.3	4.8	46 - 47	566.0	6.8	87 - 88	430.0	6.2
8.0 - 8.5	208.8	4.8	47 - 48	557.0	6.7	88 - 89	436.7	6.2
8.5 - 9.0	229.7	4.9	48 - 49	557.9	6.8	89 - 90	421.2	6.0
9.0 - 9.5	224.8	4.9	49 - 50	560.6	6.9	90 - 91	428.6	6.2
9.5 - 10.0	248.0	5.0	50 - 51	559.2	6.9	91 - 92	417.6	6.1
10 - 11	262.1	3.7	51 - 52	552.0	6.8	92 - 93	410.6	6.0
11 - 12	279.6	3.8	52 - 53	550.8	6.8	93 - 94	409.7	6.0
12 - 13	305.0	4.0	53 - 54	543.7	6.6	94 - 95	400.4	5.9
13 - 14	318.7	4.1	54 - 55	545.0	6.6	95 - 96	390.8	5.9
14 - 15	336.3	4.2	55 - 56	549.3	6.7	96 - 97	377.8	5.8
15 - 16	355.3	4.4	56 - 57	530.1	6.6	97 - 98	354.3	5.5
16 - 17	378.4	4.5	57 - 58	540.3	6.8	98 - 99	320.7	5.2
17 - 18	397.5	4.7	58 - 59	552.6	6.9	99 - 100	295.3	5.0
18 - 19	421.8	5.0	59 - 60	530.2	6.7	100 - 101	238.0	4.4
19 - 20	432.4	5.1	60 - 61	537.0	6.9	101 - 102	195.0	4.0
20 - 21	458.1	5.2	61 - 62	521.2	6.7	102 - 103	138.2	3.3
21 - 22	482.2	5.4	62 - 63	511.6	6.6	103 - 104	94.6	2.7
22 - 23	501.1	5.6	63 - 64	515.5	6.7	104 - 105	63.2	2.2
23 - 24	518.2	5.7	64 - 65	533.0	6.9	105 - 106	36.9	1.8
24 - 25	551.1	5.9	65 - 66	512.7	6.6	106 - 107	21.0	1.4
25 - 26	564.3	6.0	66 - 67	512.2	6.7	107 - 108	10.2	1.1
26 - 27	581.7	6.2	67 - 68	507.5	6.6	108 - 109	4.1	0.9
27 - 28	591.2	6.5	68 - 69	496.3	6.6	109 - 110	1.9	0.7
28 - 29	592.5	6.6	69 - 70	498.1	6.6	110 - 111	0.7	0.7
29 - 30	598.9	6.5	70 - 71	497.6	6.5	111 - 112	0.1	0.7
30 - 31	607.7	6.5	71 - 72	498.9	6.6	112 - 113	0.6	0.7

Table 6.8: 10° position

E_n (keV)	N_E ($\times 10^{-6}$)	σ ($\times 10^{-6}$)	E_n (keV)	N_E ($\times 10^{-6}$)	σ ($\times 10^{-6}$)	E_n (keV)	N_E ($\times 10^{-6}$)	σ ($\times 10^{-6}$)
0.3 - 0.5	55.6	1.6	31 - 32	1079.0	12.2	72 - 73	945.6	12.7
0.5 - 1.0	97.6	2.7	32 - 33	1105.7	12.4	73 - 74	928.4	12.6
1.0 - 1.5	144.5	4.0	33 - 34	1107.5	12.5	74 - 75	914.8	12.5
1.5 - 2.0	142.1	9.8	34 - 35	1113.2	12.6	75 - 76	922.6	12.6
2.0 - 2.5	174.9	9.0	35 - 36	1095.5	12.6	76 - 77	924.3	12.6
2.5 - 3.0	230.7	8.5	36 - 37	1103.0	12.7	77 - 78	909.4	12.5
3.0 - 3.5	226.5	8.7	37 - 38	1104.1	12.8	78 - 79	896.7	12.3
3.5 - 4.0	236.6	8.7	38 - 39	1089.7	12.7	79 - 80	898.7	12.4
4.0 - 4.5	271.5	8.9	39 - 40	1110.6	13.0	80 - 81	898.9	12.3
4.5 - 5.0	294.2	8.8	40 - 41	1100.3	13.0	81 - 82	897.9	12.4
5.0 - 5.5	305.0	8.8	41 - 42	1111.1	13.1	82 - 83	880.5	12.3
5.5 - 6.0	333.7	8.9	42 - 43	1079.0	12.8	83 - 84	871.2	12.3
6.0 - 6.5	350.6	9.2	43 - 44	1078.9	12.9	84 - 85	849.7	12.1
6.5 - 7.0	356.9	9.1	44 - 45	1091.3	13.1	85 - 86	875.1	12.4
7.0 - 7.5	375.2	9.3	45 - 46	1079.5	13.1	86 - 87	856.3	12.1
7.5 - 8.0	408.5	9.6	46 - 47	1054.5	12.9	87 - 88	838.2	12.0
8.0 - 8.5	418.1	9.7	47 - 48	1062.3	12.9	88 - 89	851.0	12.2
8.5 - 9.0	419.9	9.6	48 - 49	1056.4	13.0	89 - 90	817.0	11.7
9.0 - 9.5	473.8	9.9	49 - 50	1074.6	13.3	90 - 91	805.2	11.8
9.5 - 10.0	458.1	9.8	50 - 51	1086.0	13.4	91 - 92	798.7	11.6
10 - 11	504.6	7.3	51 - 52	1085.2	13.3	92 - 93	772.0	11.5
11 - 12	553.5	7.6	52 - 53	1046.2	13.0	93 - 94	756.2	11.3
12 - 13	594.3	7.9	53 - 54	1042.8	12.8	94 - 95	727.4	11.1
13 - 14	637.2	8.1	54 - 55	1031.1	12.6	95 - 96	691.8	10.8
14 - 15	648.8	8.3	55 - 56	1042.4	12.8	96 - 97	614.8	10.1
15 - 16	690.8	8.6	56 - 57	1023.2	12.8	97 - 98	514.1	9.1
16 - 17	709.2	8.8	57 - 58	1041.2	13.2	98 - 99	418.6	8.1
17 - 18	772.1	9.3	58 - 59	1034.2	13.2	99 - 100	315.5	7.0
18 - 19	789.9	9.5	59 - 60	984.0	12.7	100 - 101	224.2	5.9
19 - 20	839.7	9.9	60 - 61	1011.7	13.1	101 - 102	146.5	4.8
20 - 21	857.3	10.0	61 - 62	1023.3	13.2	102 - 103	87.7	3.8
21 - 22	874.6	10.1	62 - 63	984.7	12.8	103 - 104	48.2	2.9
22 - 23	923.0	10.6	63 - 64	975.7	12.8	104 - 105	25.6	2.3
23 - 24	943.0	10.7	64 - 65	1002.5	13.1	105 - 106	10.8	1.9
24 - 25	1001.8	11.1	65 - 66	973.1	12.7	106 - 107	4.1	1.6
25 - 26	1043.9	11.4	66 - 67	994.5	13.0	107 - 108	0.8	1.4
26 - 27	1059.4	11.7	67 - 68	971.4	12.7	108 - 109	0.0	1.4
27 - 28	1063.2	12.1	68 - 69	967.3	12.8	109 - 110	0.2	1.3
28 - 29	1078.9	12.4	69 - 70	962.4	12.8	110 - 111	0.1	1.3
29 - 30	1075.7	12.2	70 - 71	944.2	12.5	111 - 112	0.0	1.3
30 - 31	1060.6	12.0	71 - 72	958.3	12.7	112 - 113	1.1	1.3

Table 6.9: 15° position

E_n (keV)	N_E ($\times 10^{-6}$)	σ ($\times 10^{-6}$)	E_n (keV)	N_E ($\times 10^{-6}$)	σ ($\times 10^{-6}$)	E_n (keV)	N_E ($\times 10^{-6}$)	σ ($\times 10^{-6}$)
0.3 - 0.5	79.8	2.2	31 - 32	1434.5	15.6	72 - 73	1319.6	16.6
0.5 - 1.0	126.9	3.6	32 - 33	1447.6	15.8	73 - 74	1285.2	16.5
1.0 - 1.5	200.6	5.6	33 - 34	1464.7	16.0	74 - 75	1270.8	16.4
1.5 - 2.0	200.1	13.2	34 - 35	1466.1	16.0	75 - 76	1274.6	16.4
2.0 - 2.5	254.9	12.2	35 - 36	1455.1	16.1	76 - 77	1286.8	16.5
2.5 - 3.0	332.1	11.5	36 - 37	1450.9	16.1	77 - 78	1246.4	16.2
3.0 - 3.5	327.5	11.8	37 - 38	1484.3	16.5	78 - 79	1224.9	15.9
3.5 - 4.0	356.6	11.8	38 - 39	1475.3	16.5	79 - 80	1243.0	16.1
4.0 - 4.5	394.2	12.0	39 - 40	1481.3	16.7	80 - 81	1225.6	15.9
4.5 - 5.0	416.7	11.8	40 - 41	1462.3	16.6	81 - 82	1243.3	16.1
5.0 - 5.5	456.9	11.9	41 - 42	1477.6	16.7	82 - 83	1238.4	16.2
5.5 - 6.0	466.3	11.9	42 - 43	1466.3	16.6	83 - 84	1221.8	16.2
6.0 - 6.5	488.7	12.3	43 - 44	1461.4	16.7	84 - 85	1174.9	15.7
6.5 - 7.0	511.4	12.3	44 - 45	1468.1	16.9	85 - 86	1203.4	16.1
7.0 - 7.5	544.0	12.5	45 - 46	1444.9	16.8	86 - 87	1167.1	15.7
7.5 - 8.0	581.4	12.8	46 - 47	1445.7	16.8	87 - 88	1150.9	15.6
8.0 - 8.5	596.2	12.9	47 - 48	1424.9	16.6	88 - 89	1138.9	15.5
8.5 - 9.0	618.5	12.9	48 - 49	1449.8	17.0	89 - 90	1074.4	14.8
9.0 - 9.5	625.6	12.9	49 - 50	1464.9	17.2	90 - 91	1048.5	14.8
9.5 - 10.0	681.7	13.3	50 - 51	1481.4	17.4	91 - 92	972.5	14.1
10 - 11	736.1	9.8	51 - 52	1460.5	17.2	92 - 93	905.0	13.6
11 - 12	777.7	10.1	52 - 53	1448.1	17.0	93 - 94	793.6	12.6
12 - 13	823.9	10.3	53 - 54	1441.8	16.7	94 - 95	672.5	11.5
13 - 14	870.8	10.6	54 - 55	1461.3	16.7	95 - 96	528.5	10.1
14 - 15	922.2	11.0	55 - 56	1478.7	17.0	96 - 97	389.3	8.7
15 - 16	967.0	11.3	56 - 57	1429.0	16.8	97 - 98	261.3	7.1
16 - 17	991.5	11.5	57 - 58	1441.8	17.2	98 - 99	177.1	5.8
17 - 18	1070.0	12.2	58 - 59	1420.2	17.1	99 - 100	102.8	4.6
18 - 19	1102.5	12.5	59 - 60	1393.0	16.8	100 - 101	57.3	3.7
19 - 20	1130.3	12.8	60 - 61	1436.6	17.4	101 - 102	29.5	2.9
20 - 21	1158.6	12.9	61 - 62	1403.9	17.1	102 - 103	16	2.6
21 - 22	1186.4	13.1	62 - 63	1396.4	17.0	103 - 104	6.0	2.1
22 - 23	1253.6	13.7	63 - 64	1397.5	17.1	104 - 105	2.9	2.0
23 - 24	1263.6	13.8	64 - 65	1381.9	17.1	105 - 106	1.1	2.0
24 - 25	1343.7	14.3	65 - 66	1365.6	16.7	106 - 107	1.7	2.0
25 - 26	1374.0	14.6	66 - 67	1382.9	17.1	107 - 108	0.8	1.9
26 - 27	1404.0	15.0	67 - 68	1342.8	16.6	108 - 109	0.6	1.9
27 - 28	1397.6	15.4	68 - 69	1351.6	16.8	109 - 110	1.8	1.8
28 - 29	1415.5	15.8	69 - 70	1343.4	16.8	110 - 111	1.7	1.9
29 - 30	1399.0	15.4	70 - 71	1346.7	16.7	111 - 112	0.0	1.8
30 - 31	1423.1	15.4	71 - 72	1327.4	16.6	112 - 113	0.2	1.8

Table 6.10: 20° position

E_n (keV)	N_E ($\times 10^{-6}$)	σ ($\times 10^{-6}$)	E_n (keV)	N_E ($\times 10^{-6}$)	σ ($\times 10^{-6}$)	E_n (keV)	N_E ($\times 10^{-6}$)	σ ($\times 10^{-6}$)
0.3 - 0.5	114.5	3.2	31 - 32	1725.2	19.4	72 - 73	1611.4	20.9
0.5 - 1.0	166.3	4.7	32 - 33	1752.2	19.8	73 - 74	1589.1	20.9
1.0 - 1.5	260.0	7.3	33 - 34	1744.4	19.8	74 - 75	1539.0	20.4
1.5 - 2.0	261.8	17.1	34 - 35	1783.8	20.1	75 - 76	1560.8	20.6
2.0 - 2.5	332.3	15.8	35 - 36	1720.9	19.9	76 - 77	1535.3	20.4
2.5 - 3.0	426.9	14.9	36 - 37	1765.8	20.2	77 - 78	1522.7	20.3
3.0 - 3.5	425.0	15.3	37 - 38	1720.2	20.1	78 - 79	1517.4	20.2
3.5 - 4.0	469.4	15.4	38 - 39	1727.7	20.2	79 - 80	1517.9	20.3
4.0 - 4.5	533.5	15.7	39 - 40	1774.6	20.7	80 - 81	1479.5	19.9
4.5 - 5.0	534.0	15.3	40 - 41	1800.8	21.0	81 - 82	1464.6	19.8
5.0 - 5.5	588.8	15.5	41 - 42	1773.2	20.8	82 - 83	1439.9	19.7
5.5 - 6.0	615.0	15.6	42 - 43	1745.4	20.6	83 - 84	1395.5	19.5
6.0 - 6.5	642.6	16.0	43 - 44	1797.8	21.1	84 - 85	1299.6	18.6
6.5 - 7.0	682.0	16.0	44 - 45	1757.0	21.0	85 - 86	1233.3	18.3
7.0 - 7.5	687.4	16.2	45 - 46	1769.1	21.1	86 - 87	1100.1	17.0
7.5 - 8.0	726.8	16.5	46 - 47	1731.2	20.9	87 - 88	994.3	16.0
8.0 - 8.5	735.5	16.6	47 - 48	1720.4	20.7	88 - 89	808.6	14.4
8.5 - 9.0	809.0	16.9	48 - 49	1752.0	21.2	89 - 90	620.6	12.4
9.0 - 9.5	807.7	16.8	49 - 50	1777.1	21.5	90 - 91	447.9	10.7
9.5 - 10.0	861.9	17.1	50 - 51	1794.4	21.7	91 - 92	294.9	8.6
10 - 11	926.4	12.6	51 - 52	1789.0	21.6	92 - 93	192.1	7.2
11 - 12	980.7	13.0	52 - 53	1753.3	21.2	93 - 94	106.3	5.6
12 - 13	1033.9	13.3	53 - 54	1742.7	20.9	94 - 95	54.4	4.4
13 - 14	1115.6	13.8	54 - 55	1776.4	20.9	95 - 96	26.0	3.6
14 - 15	1110.6	13.8	55 - 56	1771.1	21.1	96 - 97	14.5	3.4
15 - 16	1203.2	14.5	56 - 57	1734.9	21.0	97 - 98	8.2	3.0
16 - 17	1219.7	14.7	57 - 58	1771.0	21.7	98 - 99	4.4	2.8
17 - 18	1315.2	15.5	58 - 59	1735.3	21.5	99 - 100	0.3	2.6
18 - 19	1338.8	15.8	59 - 60	1705.1	21.2	100 - 101	0.0	2.6
19 - 20	1359.4	16.0	60 - 61	1741.6	21.7	101 - 102	0.4	2.5
20 - 21	1426.1	16.4	61 - 62	1718.8	21.5	102 - 103	4.5	2.7
21 - 22	1476.4	16.7	62 - 63	1693.1	21.3	103 - 104	1.5	2.5
22 - 23	1523.2	17.2	63 - 64	1686.9	21.3	104 - 105	0.0	2.5
23 - 24	1517.4	17.2	64 - 65	1707.3	21.6	105 - 106	0.0	2.6
24 - 25	1604.1	17.8	65 - 66	1654.0	20.9	106 - 107	1.5	2.5
25 - 26	1665.5	18.3	66 - 67	1681.0	21.4	107 - 108	2.0	2.5
26 - 27	1655.6	18.5	67 - 68	1643.3	20.9	108 - 109	0.1	2.5
27 - 28	1662.9	19.1	68 - 69	1653.3	21.1	109 - 110	0.6	2.3
28 - 29	1705.8	19.7	69 - 70	1644.8	21.1	110 - 111	0.7	2.4
29 - 30	1658.6	19.1	70 - 71	1603.3	20.6	111 - 112	0.1	2.4
30 - 31	1699.5	19.1	71 - 72	1620.6	20.9	112 - 113	1.7	2.4

Table 6.11: 25° position

E_n (keV)	N_E ($\times 10^{-6}$)	σ ($\times 10^{-6}$)	E_n (keV)	N_E ($\times 10^{-6}$)	σ ($\times 10^{-6}$)	E_n (keV)	N_E ($\times 10^{-6}$)	σ ($\times 10^{-6}$)
0.3 - 0.5	120.3	3.4	31 - 32	1920.6	23.4	72 - 73	1727.2	24.6
0.5 - 1.0	163.4	4.6	32 - 33	1909.0	23.6	73 - 74	1727.9	24.8
1.0 - 1.5	267.1	7.5	33 - 34	1987.3	24.1	74 - 75	1673.4	24.3
1.5 - 2.0	289.8	21.4	34 - 35	1963.7	24.1	75 - 76	1661.8	24.2
2.0 - 2.5	381.8	19.8	35 - 36	1997.5	24.5	76 - 77	1609.8	23.8
2.5 - 3.0	486.4	18.6	36 - 37	1984.7	24.5	77 - 78	1517.4	23.0
3.0 - 3.5	497.3	19.1	37 - 38	1935.7	24.3	78 - 79	1377.1	21.7
3.5 - 4.0	516.9	19.2	38 - 39	1951.4	24.5	79 - 80	1273.0	20.8
4.0 - 4.5	605.7	19.6	39 - 40	2011.1	25.2	80 - 81	1066.3	18.9
4.5 - 5.0	643.1	19.3	40 - 41	2007.2	25.3	81 - 82	841.7	16.7
5.0 - 5.5	688.5	19.4	41 - 42	1987.8	25.1	82 - 83	652.7	14.7
5.5 - 6.0	702.8	19.4	42 - 43	1975.4	25.0	83 - 84	448.2	12.4
6.0 - 6.5	754.8	20.0	43 - 44	1969.6	25.2	84 - 85	272.9	9.9
6.5 - 7.0	785.9	20.0	44 - 45	1980.5	25.4	85 - 86	165.7	8.3
7.0 - 7.5	811.5	20.3	45 - 46	1973.1	25.4	86 - 87	86.8	6.6
7.5 - 8.0	864.6	20.7	46 - 47	2010.6	25.7	87 - 88	42.1	5.1
8.0 - 8.5	913.8	21.0	47 - 48	1988.5	25.5	88 - 89	24.1	4.5
8.5 - 9.0	936.0	21.0	48 - 49	1943.8	25.4	89 - 90	9.7	4.0
9.0 - 9.5	945.2	20.9	49 - 50	1953.4	25.7	90 - 91	2.9	3.9
9.5 - 10.0	986.3	21.2	50 - 51	2006.0	26.2	91 - 92	2.3	3.8
10 - 11	1086.1	15.7	51 - 52	1999.5	26.0	92 - 93	0.0	3.7
11 - 12	1147.9	16.2	52 - 53	1976.2	25.7	93 - 94	2.4	3.6
12 - 13	1196.8	16.5	53 - 54	1940.2	25.1	94 - 95	1.6	3.6
13 - 14	1262.2	16.9	54 - 55	1990.4	25.3	95 - 96	1.9	3.5
14 - 15	1315.6	17.3	55 - 56	2011.2	25.7	96 - 97	0.0	3.5
15 - 16	1384.9	17.9	56 - 57	1959.5	25.5	97 - 98	1.2	3.5
16 - 17	1402.6	18.1	57 - 58	1957.4	26.0	98 - 99	0.9	3.3
17 - 18	1500.2	19.0	58 - 59	1939.5	26.0	99 - 100	0.0	3.2
18 - 19	1524.5	19.4	59 - 60	1919.0	25.6	100 - 101	0.0	3.3
19 - 20	1594.7	20.0	60 - 61	1929.5	26.1	101 - 102	0.0	3.1
20 - 21	1608.3	20.0	61 - 62	1915.8	25.9	102 - 103	0.0	3.2
21 - 22	1669.5	20.4	62 - 63	1901.7	25.8	103 - 104	1.3	3.1
22 - 23	1716.8	21.0	63 - 64	1837.4	25.3	104 - 105	2.3	3.3
23 - 24	1724.4	21.0	64 - 65	1915.7	26.1	105 - 106	4.8	3.5
24 - 25	1735.6	21.2	65 - 66	1883.6	25.5	106 - 107	0.8	3.1
25 - 26	1816.8	21.8	66 - 67	1915.3	26.1	107 - 108	0.4	3.1
26 - 27	1900.5	22.7	67 - 68	1854.3	25.3	108 - 109	0.6	3.2
27 - 28	1856.0	23.1	68 - 69	1827.6	25.4	109 - 110	2.3	2.9
28 - 29	1864.9	23.6	69 - 70	1848.9	25.5	110 - 111	2.1	3.1
29 - 30	1839.2	23.0	70 - 71	1788.4	24.8	111 - 112	0.0	2.9
30 - 31	1881.9	23.0	71 - 72	1823.8	25.3	112 - 113	1.8	3.0

Table 6.12: 30° position

E_n (keV)	N_E ($\times 10^{-6}$)	σ ($\times 10^{-6}$)	E_n (keV)	N_E ($\times 10^{-6}$)	σ ($\times 10^{-6}$)	E_n (keV)	N_E ($\times 10^{-6}$)	σ ($\times 10^{-6}$)
0.3 - 0.5	153.3	4.3	31 - 32	2004.6	24.2	72 - 73	1022	18.7
0.5 - 1.0	178.7	5.0	32 - 33	2081.7	25.0	73 - 74	766.5	16.3
1.0 - 1.5	286.8	8.0	33 - 34	2081.5	25.0	74 - 75	543.1	13.8
1.5 - 2.0	341.9	23.7	34 - 35	2089.2	25.2	75 - 76	349.2	11.2
2.0 - 2.5	454.7	21.9	35 - 36	2050.7	25.1	76 - 77	209.9	9.2
2.5 - 3.0	572.4	20.6	36 - 37	2087.8	25.4	77 - 78	109.9	7.5
3.0 - 3.5	572.3	21.2	37 - 38	2088.1	25.6	78 - 79	51.8	6.0
3.5 - 4.0	606.5	21.2	38 - 39	2089.7	25.7	79 - 80	30.4	5.6
4.0 - 4.5	712.8	21.7	39 - 40	2132.4	26.3	80 - 81	6.0	5.0
4.5 - 5.0	744.5	21.2	40 - 41	2172.5	26.6	81 - 82	7.2	4.8
5.0 - 5.5	743.9	21.1	41 - 42	2139.7	26.4	82 - 83	3.3	4.5
5.5 - 6.0	814.5	21.4	42 - 43	2081.1	26.0	83 - 84	2.9	4.5
6.0 - 6.5	864.9	22.0	43 - 44	2139.4	26.6	84 - 85	0.5	4.7
6.5 - 7.0	878.7	21.8	44 - 45	2147.5	26.9	85 - 86	0.4	4.8
7.0 - 7.5	949.4	22.4	45 - 46	2107.6	26.6	86 - 87	0.5	4.7
7.5 - 8.0	975.4	22.6	46 - 47	2095.2	26.5	87 - 88	4.1	4.3
8.0 - 8.5	1008.6	22.8	47 - 48	2102.7	26.5	88 - 89	5.8	4.3
8.5 - 9.0	1029.0	22.7	48 - 49	2123.2	27.0	89 - 90	4.0	4.1
9.0 - 9.5	1098.9	23.0	49 - 50	2143.9	27.3	90 - 91	0.0	4.2
9.5 - 10.0	1143.2	23.3	50 - 51	2119.2	27.2	91 - 92	0.0	4.2
10 - 11	1206.2	17.0	51 - 52	2180.4	27.6	92 - 93	3.1	4.3
11 - 12	1312.9	17.7	52 - 53	2197.9	27.5	93 - 94	6.2	4.0
12 - 13	1356.0	17.9	53 - 54	2119.4	26.6	94 - 95	3.5	4.0
13 - 14	1415.2	18.3	54 - 55	2132.8	26.5	95 - 96	4.2	4.0
14 - 15	1450.0	18.6	55 - 56	2170.9	27.0	96 - 97	3.4	4.1
15 - 16	1543.7	19.2	56 - 57	2087.2	26.6	97 - 98	1.2	3.9
16 - 17	1566.9	19.5	57 - 58	2077.9	27.0	98 - 99	0.3	3.6
17 - 18	1634.8	20.2	58 - 59	2088.4	27.3	99 - 100	0.0	3.6
18 - 19	1685.7	20.8	59 - 60	2108.4	27.2	100 - 101	0.9	3.7
19 - 20	1717.8	21.1	60 - 61	2063.9	27.3	101 - 102	2.4	3.6
20 - 21	1744.7	21.2	61 - 62	2058.2	27.1	102 - 103	0.2	3.5
21 - 22	1745.7	21.3	62 - 63	2033.3	26.9	103 - 104	0.8	3.4
22 - 23	1803.8	21.9	63 - 64	1983.0	26.6	104 - 105	0.0	3.4
23 - 24	1884.5	22.4	64 - 65	1997.1	26.9	105 - 106	0.0	3.6
24 - 25	1944.4	22.9	65 - 66	1885.8	25.7	106 - 107	0.0	3.4
25 - 26	1999.0	23.3	66 - 67	1910.1	26.2	107 - 108	0.3	3.4
26 - 27	2006.9	23.7	67 - 68	1841.8	25.4	108 - 109	0.0	3.4
27 - 28	2045.6	24.6	68 - 69	1733.7	24.7	109 - 110	0.0	3.0
28 - 29	1992.6	24.8	69 - 70	1601.0	23.7	110 - 111	0.0	3.3
29 - 30	2026.6	24.6	70 - 71	1425.5	22.0	111 - 112	0.0	3.2
30 - 31	2015.4	24.1	71 - 72	1253.6	20.7	112 - 113	0.0	3.2

Table 6.13: 35° position

E_n (keV)	N_E ($\times 10^{-6}$)	σ ($\times 10^{-6}$)	E_n (keV)	N_E ($\times 10^{-6}$)	σ ($\times 10^{-6}$)	E_n (keV)	N_E ($\times 10^{-6}$)	σ ($\times 10^{-6}$)
0.3 - 0.5	114.1	3.2	31 - 32	2039.8	26.3	72 - 73	8.6	6.2
0.5 - 1.0	135.2	3.8	32 - 33	2119.6	27.1	73 - 74	2.5	6.5
1.0 - 1.5	251.1	7.0	33 - 34	2097.9	27.0	74 - 75	3.3	6.0
1.5 - 2.0	401.4	26.9	34 - 35	2122.0	27.3	75 - 76	4.6	5.7
2.0 - 2.5	455.4	24.7	35 - 36	2075.8	27.2	76 - 77	4.6	5.7
2.5 - 3.0	603.2	23.3	36 - 37	2137.6	27.6	77 - 78	5.3	5.9
3.0 - 3.5	617.3	23.9	37 - 38	2103.6	27.6	78 - 79	8.8	5.4
3.5 - 4.0	670.6	24.0	38 - 39	2085.3	27.6	79 - 80	2.0	5.5
4.0 - 4.5	720.7	24.3	39 - 40	2125.2	28.1	80 - 81	0.8	5.5
4.5 - 5.0	774.8	23.8	40 - 41	2163.5	28.5	81 - 82	4.0	5.3
5.0 - 5.5	827.2	23.9	41 - 42	2138.0	28.3	82 - 83	3.0	5.1
5.5 - 6.0	890.8	24.2	42 - 43	2095.3	27.9	83 - 84	3.8	5.1
6.0 - 6.5	917.9	24.8	43 - 44	2120.1	28.3	84 - 85	0.0	5.3
6.5 - 7.0	975.3	24.8	44 - 45	2149.2	28.8	85 - 86	0.0	5.5
7.0 - 7.5	983.1	25.0	45 - 46	2163.6	28.9	86 - 87	0.0	5.3
7.5 - 8.0	1062.3	25.6	46 - 47	2112.4	28.6	87 - 88	0.6	4.7
8.0 - 8.5	1047.4	25.5	47 - 48	2102.7	28.4	88 - 89	4.1	4.8
8.5 - 9.0	1098.9	25.5	48 - 49	2113.0	28.8	89 - 90	2.9	4.6
9.0 - 9.5	1125.9	25.5	49 - 50	2166.4	29.4	90 - 91	4.2	5.0
9.5 - 10.0	1173.4	25.8	50 - 51	2145.9	29.3	91 - 92	0.7	4.7
10 - 11	1267.8	18.9	51 - 52	2157.6	29.3	92 - 93	1.6	4.7
11 - 12	1364.9	19.7	52 - 53	2126.0	28.8	93 - 94	0.0	4.3
12 - 13	1433.6	20.0	53 - 54	2116.0	28.4	94 - 95	0.0	4.4
13 - 14	1460.6	20.2	54 - 55	2122.6	28.3	95 - 96	0.0	4.2
14 - 15	1483.2	20.5	55 - 56	2090.7	28.3	96 - 97	4.3	4.7
15 - 16	1597.1	21.2	56 - 57	2009.6	27.9	97 - 98	2.9	4.4
16 - 17	1625.3	21.5	57 - 58	2068.7	28.9	98 - 99	3.6	4.3
17 - 18	1663.5	22.1	58 - 59	1948.8	28.1	99 - 100	1.5	4.2
18 - 19	1749.4	22.9	59 - 60	1874.2	27.3	100 - 101	1.1	4.3
19 - 20	1748.5	23.1	60 - 61	1819.0	27.3	101 - 102	0.0	3.9
20 - 21	1769.8	23.1	61 - 62	1706.0	26.2	102 - 103	0.0	3.9
21 - 22	1813.4	23.4	62 - 63	1531.3	24.7	103 - 104	0.0	3.7
22 - 23	1886.4	24.2	63 - 64	1281.0	22.5	104 - 105	0.4	4.0
23 - 24	1912.5	24.3	64 - 65	1038.8	20.4	105 - 106	0.0	4.1
24 - 25	1925.3	24.5	65 - 66	781.7	17.6	106 - 107	2.7	4.0
25 - 26	2010.9	25.1	66 - 67	573.4	15.4	107 - 108	1.1	3.9
26 - 27	2012.0	25.6	67 - 68	373.0	12.7	108 - 109	1.4	4.0
27 - 28	2060.9	26.6	68 - 69	208.7	10.5	109 - 110	1.9	3.6
28 - 29	2011.3	26.8	69 - 70	103.4	8.3	110 - 111	0.1	3.8
29 - 30	2061.0	26.7	70 - 71	55.9	6.9	111 - 112	0 .0	3.7
30 - 31	2026.0	26.1	71 - 72	25.1	6.6	112 - 113	0.0	3.6

Table 6.14: 40° position

E_n (keV)	N_E ($\times 10^{-6}$)	σ ($\times 10^{-6}$)	E_n (keV)	N_E ($\times 10^{-6}$)	σ ($\times 10^{-6}$)	E_n (keV)	N_E ($\times 10^{-6}$)	σ ($\times 10^{-6}$)
0.3 - 0.5	63.8	1.8	31 - 32	2232.1	29.8	72 - 73	5.3	6.9
0.5 - 1.0	111.4	3.1	32 - 33	2227.1	30.0	73 - 74	0.0	7.0
1.0 - 1.5	202.7	5.7	33 - 34	2281.8	30.5	74 - 75	0.0	6.5
1.5 - 2.0	434.1	30.0	34 - 35	2228.1	30.2	75 - 76	6.3	6.4
2.0 - 2.5	562.8	27.7	35 - 36	2256.9	30.7	76 - 77	5.9	6.3
2.5 - 3.0	748.0	26.3	36 - 37	2241.1	30.6	77 - 78	3.4	6.4
3.0 - 3.5	787.7	27.2	37 - 38	2207.3	30.6	78 - 79	7.2	6.0
3.5 - 4.0	759.1	27.0	38 - 39	2235.2	30.9	79 - 80	0.6	5.8
4.0 - 4.5	884.5	27.6	39 - 40	2242.5	31.2	80 - 81	0.0	6.0
4.5 - 5.0	903.7	27.0	40 - 41	2224.3	31.2	81 - 82	0.0	5.6
5.0 - 5.5	968.2	27.2	41 - 42	2267.2	31.5	82 - 83	4.4	5.6
5.5 - 6.0	984.7	27.2	42 - 43	2186.9	30.9	83 - 84	3.3	5.7
6.0 - 6.5	1027.5	28.0	43 - 44	2181.2	31.0	84 - 85	0.0	5.8
6.5 - 7.0	1067.6	27.8	44 - 45	2157.5	31.2	85 - 86	0.0	5.8
7.0 - 7.5	1101.3	28.3	45 - 46	2105.8	30.7	86 - 87	0.0	5.7
7.5 - 8.0	1171.1	28.8	46 - 47	2038.6	30.2	87 - 88	2.0	5.3
8.0 - 8.5	1242.1	29.3	47 - 48	1936.6	29.3	88 - 89	0.4	5.2
8.5 - 9.0	1225.0	28.9	48 - 49	1869.4	29.2	89 - 90	4.4	5.1
9.0 - 9.5	1288.0	29.2	49 - 50	1683.7	27.8	90 - 91	2.6	5.5
9.5 - 10.0	1327.9	29.4	50 - 51	1463.9	26.0	91 - 92	0.0	5.2
10 - 11	1420.0	21.5	51 - 52	1199.0	23.4	92 - 93	2.2	5.3
11 - 12	1510.8	22.3	52 - 53	909.3	20.3	93 - 94	2.0	4.9
12 - 13	1574.5	22.6	53 - 54	600.2	16.7	94 - 95	4.1	5.1
13 - 14	1602.3	22.8	54 - 55	430.2	14.5	95 - 96	1.0	4.8
14 - 15	1635.9	23.2	55 - 56	262.4	12.5	96 - 97	0.0	5.0
15 - 16	1741.1	23.9	56 - 57	151.7	10.5	97 - 98	0.0	4.8
16 - 17	1778.2	24.4	57 - 58	80.7	9.3	98 - 99	1.0	4.6
17 - 18	1806.6	25.0	58 - 59	31.8	8.8	99 - 100	2.5	4.7
18 - 19	1891.1	25.8	59 - 60	15.8	8.1	100 - 101	1.2	4.8
19 - 20	1920.8	26.1	60 - 61	7.6	8.3	101 - 102	0.0	4.3
20 - 21	1932.9	26.1	61 - 62	6.2	7.7	102 - 103	0.0	4.3
21 - 22	2011.0	26.7	62 - 63	2.3	7.8	103 - 104	0.0	4.1
22 - 23	2041.0	27.2	63 - 64	1.7	7.3	104 - 105	0.2	4.3
23 - 24	2022.2	27.1	64 - 65	4.2	7.6	105 - 106	1.9	4.6
24 - 25	2080.6	27.6	65 - 66	0.0	7.3	106 - 107	0.5	4.4
25 - 26	2110.5	27.9	66 - 67	1.6	7.3	107 - 108	0.0	4.2
26 - 27	2193.7	28.9	67 - 68	6.8	6.9	108 - 109	0.0	4.4
27 - 28	2249.5	30.0	68 - 69	6.7	7.1	109 - 110	0.0	3.7
28 - 29	2211.9	30.4	69 - 70	0.0	6.6	110 - 111	0.0	4.1
29 - 30	2183.5	29.7	70 - 71	5.3	6.3	111 - 112	0.9	4.1
30 - 31	2184.5	29.2	71 - 72	5.6	6.5	112 - 113	2.3	4.1

Table 6.15: 45° position

E_n (keV)	N_E ($\times 10^{-6}$)	σ ($\times 10^{-6}$)	E_n (keV)	N_E ($\times 10^{-6}$)	σ ($\times 10^{-6}$)	E_n (keV)	N_E ($\times 10^{-6}$)	σ ($\times 10^{-6}$)
0.3 - 0.5	43	1.2	31 - 32	2109.4	30.3	72 - 73	0.0	7.3
0.5 - 1.0	71.7	2.0	32 - 33	2189.9	31.2	73 - 74	0.0	7.6
1.0 - 1.5	148.1	4.1	33 - 34	2114.3	30.7	74 - 75	0.0	7.1
1.5 - 2.0	327.6	32.3	34 - 35	2039.5	30.3	75 - 76	9.6	7.1
2.0 - 2.5	529.4	30.0	35 - 36	2078.3	30.8	76 - 77	3.7	6.8
2.5 - 3.0	704.0	28.3	36 - 37	2006.1	30.2	77 - 78	3.9	7.0
3.0 - 3.5	719.9	29.1	37 - 38	1909.9	29.8	78 - 79	9.1	6.6
3.5 - 4.0	814.4	29.4	38 - 39	1823.0	29.2	79 - 80	1.2	6.4
4.0 - 4.5	861.5	29.7	39 - 40	1685.2	28.3	80 - 81	0.0	6.5
4.5 - 5.0	911.0	29.1	40 - 41	1460.0	26.5	81 - 82	3.2	6.3
5.0 - 5.5	981.6	29.2	41 - 42	1220.7	24.3	82 - 83	2.8	6.1
5.5 - 6.0	1035.2	29.5	42 - 43	922.3	21.5	83 - 84	3.1	6.2
6.0 - 6.5	1095.7	30.4	43 - 44	675.0	19.0	84 - 85	0.0	6.4
6.5 - 7.0	1095.8	30.0	44 - 45	437.1	16.6	85 - 86	0.0	6.7
7.0 - 7.5	1119.4	30.4	45 - 46	284.4	14.3	86 - 87	0.0	6.4
7.5 - 8.0	1225.2	31.2	46 - 47	147.5	12.1	87 - 88	2.0	5.8
8.0 - 8.5	1206.9	31.1	47 - 48	78.8	10.7	88 - 89	2.9	5.8
8.5 - 9.0	1285.9	31.3	48 - 49	31.3	10.3	89 - 90	0.4	5.4
9.0 - 9.5	1319.1	31.3	49 - 50	20.4	9.8	90 - 91	0.1	5.8
9.5 - 10.0	1362.8	31.6	50 - 51	4.7	9.5	91 - 92	0.1	5.8
10 - 11	1448.2	23.0	51 - 52	11.7	9.3	92 - 93	2.3	5.8
11 - 12	1530.2	23.8	52 - 53	9.9	8.7	93 - 94	0.1	5.2
12 - 13	1572.2	24.0	53 - 54	8.2	8.4	94 - 95	0.8	5.4
13 - 14	1635.9	24.4	54 - 55	10.7	8.4	95 - 96	0.6	5.2
14 - 15	1631.3	24.5	55 - 56	0.4	8.6	96 - 97	0.0	5.3
15 - 16	1736.3	25.2	56 - 57	6.8	8.4	97 - 98	1.5	5.3
16 - 17	1706.1	25.3	57 - 58	9.2	8.4	98 - 99	1.9	5.0
17 - 18	1821.1	26.4	58 - 59	0.0	8.8	99 - 100	0.0	4.8
18 - 19	1852.1	27.0	59 - 60	2.0	8.5	100 - 101	0.0	5.1
19 - 20	1928.8	27.6	60 - 61	2.0	8.8	101 - 102	0.8	4.8
20 - 21	1969.7	27.7	61 - 62	2.8	8.3	102 - 103	2.2	4.9
21 - 22	1944.9	27.6	62 - 63	2.6	8.5	103 - 104	2.2	4.7
22 - 23	1975.1	28.2	63 - 64	1.9	7.9	104 - 105	0.5	4.7
23 - 24	2031.8	28.5	64 - 65	0.0	8.0	105 - 106	0.0	4.8
24 - 25	2104.3	29.1	65 - 66	0.9	7.9	106 - 107	0.0	4.7
25 - 26	2115.6	29.3	66 - 67	4.6	7.9	107 - 108	0.0	4.6
26 - 27	2128.7	29.9	67 - 68	6.8	7.5	108 - 109	0.0	4.7
27 - 28	2194.2	31.1	68 - 69	0.6	7.5	109 - 110	0.0	4.1
28 - 29	2133.9	31.4	69 - 70	3.1	7.4	110 - 111	0.3	4.6
29 - 30	2083.3	30.5	70 - 71	11.8	7.0	111 - 112	0.3	4.5
30 - 31	2113.2	30.2	71 - 72	4.4	7.1	112 - 113	1.5	4.4

Table 6.16: 50° position

E_n (keV)	N_E ($\times 10^{-6}$)	σ ($\times 10^{-6}$)	E_n (keV)	N_E ($\times 10^{-6}$)	σ ($\times 10^{-6}$)	E_n (keV)	N_E ($\times 10^{-6}$)	σ ($\times 10^{-6}$)
0.3 - 0.5	80.8	2.3	31 - 32	1137.9	19.8	72 - 73	0.1	7.0
0.5 - 1.0	78.7	2.2	32 - 33	884.1	18.3	73 - 74	0.0	7.8
1.0 - 1.5	106.0	3.0	33 - 34	728.2	17.0	74 - 75	1.8	6.9
1.5 - 2.0	308.5	31.2	34 - 35	515.0	15.3	75 - 76	4.0	6.9
2.0 - 2.5	417.8	28.5	35 - 36	316.2	13.8	76 - 77	1.1	6.4
2.5 - 3.0	677.2	26.8	36 - 37	195.7	12.2	77 - 78	1.8	6.8
3.0 - 3.5	711.6	27.5	37 - 38	108.0	11.6	78 - 79	4.4	6.0
3.5 - 4.0	780.8	27.6	38 - 39	60.1	11.1	79 - 80	4.8	6.5
4.0 - 4.5	860.7	27.8	39 - 40	26.6	10.5	80 - 81	0.0	6.5
4.5 - 5.0	896.1	27.1	40 - 41	16.5	10.3	81 - 82	0.6	6.0
5.0 - 5.5	979.5	27.1	41 - 42	11.3	10.0	82 - 83	4.5	6.0
5.5 - 6.0	1049.0	27.3	42 - 43	7.0	9.7	83 - 84	5.5	6.1
6.0 - 6.5	1060.4	27.9	43 - 44	14.9	9.8	84 - 85	0.0	6.3
6.5 - 7.0	1150.1	27.8	44 - 45	2.2	9.9	85 - 86	0.0	6.5
7.0 - 7.5	1139.2	28.0	45 - 46	9.0	9.6	86 - 87	0.0	6.4
7.5 - 8.0	1187.5	28.2	46 - 47	14.2	9.4	87 - 88	2.1	5.6
8.0 - 8.5	1226.2	28.4	47 - 48	14.2	9.1	88 - 89	3.6	5.5
8.5 - 9.0	1197.6	27.8	48 - 49	2.9	9.4	89 - 90	3.4	5.3
9.0 - 9.5	1290.2	28.0	49 - 50	12.7	9.4	90 - 91	0.3	5.7
9.5 - 10.0	1324.3	28.1	50 - 51	6.1	9.2	91 - 92	0.0	5.5
10 - 11	1408.3	20.4	51 - 52	6.8	8.9	92 - 93	0.3	5.6
11 - 12	1499.7	21.1	52 - 53	7.0	8.4	93 - 94	0.0	5.1
12 - 13	1540.2	21.1	53 - 54	13.4	8.2	94 - 95	0.0	5.1
13 - 14	1600.7	21.4	54 - 55	11.1	8.2	95 - 96	0.3	5.0
14 - 15	1624.6	21.6	55 - 56	3.9	8.5	96 - 97	0.2	5.4
15 - 16	1669.7	21.8	56 - 57	0.0	7.9	97 - 98	3.2	5.2
16 - 17	1670.5	22.0	57 - 58	14.6	8.4	98 - 99	1.9	4.8
17 - 18	1749.4	22.7	58 - 59	0.0	8.8	99 - 100	2.3	4.8
18 - 19	1827.8	23.5	59 - 60	3.0	8.2	100 - 101	0.6	5.0
19 - 20	1842.0	23.6	60 - 61	0.0	8.3	101 - 102	2.5	4.7
20 - 21	1818.9	23.3	61 - 62	0.0	7.8	102 - 103	0.2	4.6
21 - 22	1835.8	23.3	62 - 63	0.0	8.0	103 - 104	0.0	4.3
22 - 23	1860.3	23.8	63 - 64	6.4	7.6	104 - 105	0.1	4.6
23 - 24	1880.6	23.9	64 - 65	0.0	7.7	105 - 106	0.1	4.9
24 - 25	1870.3	23.9	65 - 66	4.7	7.7	106 - 107	0.0	4.6
25 - 26	1837.0	23.7	66 - 67	4.2	7.8	107 - 108	0.0	4.5
26 - 27	1791.9	23.9	67 - 68	4.8	7.5	108 - 109	1.1	4.8
27 - 28	1778.2	24.4	68 - 69	1.7	7.4	109 - 110	0.0	4.0
28 - 29	1600.5	23.8	69 - 70	8.8	7.0	110 - 111	0.0	4.4
29 - 30	1457.4	22.5	70 - 71	7.5	6.8	111 - 112	0.0	4.4
30 - 31	1298.6	20.8	71 - 72	5.8	7.0	112 - 113	0.3	4.2

Table 6.17: 55° position

E_n (keV)	N_E ($\times 10^{-6}$)	σ ($\times 10^{-6}$)	E_n (keV)	N_E ($\times 10^{-6}$)	σ ($\times 10^{-6}$)	E_n (keV)	N_E ($\times 10^{-6}$)	σ ($\times 10^{-6}$)
0.3 - 0.5	7.6	0.2	31 - 32	14.1	11.4	72 - 73	1.9	7.5
0.5 - 1.0	15.0	0.4	32 - 33	5.6	11.6	73 - 74	1.4	8.1
1.0 - 1.5	31.0	0.9	33 - 34	2.8	11.2	74 - 75	0.0	7.3
1.5 - 2.0	99.7	32.0	34 - 35	10.5	11.3	75 - 76	6.9	7.1
2.0 - 2.5	151.7	29.0	35 - 36	0.0	11.3	76 - 77	0.5	6.8
2.5 - 3.0	297.5	26.8	36 - 37	13.7	10.8	77 - 78	1.6	7.1
3.0 - 3.5	379.4	27.6	37 - 38	14.2	11.0	78 - 79	7.0	6.4
3.5 - 4.0	444.9	27.6	38 - 39	15.1	11.0	79 - 80	1.2	6.7
4.0 - 4.5	528.4	27.7	39 - 40	8.6	10.6	80 - 81	0.8	6.9
4.5 - 5.0	629.7	27.1	40 - 41	10.6	10.7	81 - 82	1.5	6.4
5.0 - 5.5	716.5	27.0	41 - 42	8.6	10.4	82 - 83	3.7	6.2
5.5 - 6.0	731.1	26.9	42 - 43	10.8	10.1	83 - 84	0.4	6.1
6.0 - 6.5	816.5	27.8	43 - 44	11.7	10.1	84 - 85	0.0	6.7
6.5 - 7.0	897.0	27.7	44 - 45	7.7	10.5	85 - 86	0.3	6.8
7.0 - 7.5	886.3	27.8	45 - 46	1.4	9.9	86 - 87	0.0	6.6
7.5 - 8.0	970.0	28.2	46 - 47	8.0	9.7	87 - 88	0.3	5.8
8.0 - 8.5	1000.3	28.2	47 - 48	8.3	9.4	88 - 89	1.9	5.7
8.5 - 9.0	1031.3	28.0	48 - 49	4.5	9.9	89 - 90	4.0	5.6
9.0 - 9.5	1070.7	27.9	49 - 50	4.3	9.7	90 - 91	1.3	6.0
9.5 - 10.0	1133.2	28.1	50 - 51	5.6	9.6	91 - 92	0.0	5.8
10 - 11	1119.5	20.0	51 - 52	13.7	9.4	92 - 93	2.0	5.9
11 - 12	1178.4	20.5	52 - 53	16.9	8.9	93 - 94	2.5	5.3
12 - 13	1239.4	20.5	53 - 54	6.0	8.4	94 - 95	0.5	5.4
13 - 14	1182.4	20.2	54 - 55	4.3	8.5	95 - 96	0.0	5.2
14 - 15	1143.7	20.1	55 - 56	0.0	8.8	96 - 97	0.0	5.5
15 - 16	1120.2	19.9	56 - 57	3.0	8.5	97 - 98	0.6	5.3
16 - 17	1032.9	19.5	57 - 58	9.9	8.7	98 - 99	0.8	5.0
17 - 18	958.9	19.3	58 - 59	0.0	9.1	99 - 100	0.2	5.0
18 - 19	870.1	19.0	59 - 60	3.6	8.5	100 - 101	0.3	5.2
19 - 20	766.7	18.4	60 - 61	0.0	8.8	101 - 102	1.0	4.8
20 - 21	665.5	17.4	61 - 62	1.8	8.3	102 - 103	1.9	4.9
21 - 22	539.9	16.3	62 - 63	0.0	8.6	103 - 104	0.0	4.6
22 - 23	425.6	15.8	63 - 64	7.3	8.2	104 - 105	0.6	4.8
23 - 24	310.2	14.7	64 - 65	1.0	8.1	105 - 106	0.0	5.1
24 - 25	225.2	13.9	65 - 66	0.0	7.9	106 - 107	0.6	4.8
25 - 26	165.3	13.3	66 - 67	0.6	8.0	107 - 108	1.1	4.8
26 - 27	73.7	13.0	67 - 68	3.1	7.7	108 - 109	0.0	4.9
27 - 28	52.7	12.8	68 - 69	0.0	7.8	109 - 110	0.0	4.1
28 - 29	20.2	13.1	69 - 70	3.3	7.3	110 - 111	0.0	4.6
29 - 30	0.6	12.6	70 - 71	7.2	6.9	111 - 112	0.0	4.5
30 - 31	18.1	11.6	71 - 72	4.2	7.4	112 - 113	2.8	4.5

Table 6.18: 60° position

E_n (keV)	N_E ($\times 10^{-6}$)	σ ($\times 10^{-6}$)	E_n (keV)	N_E ($\times 10^{-6}$)	σ ($\times 10^{-6}$)	E_n (keV)	N_E ($\times 10^{-6}$)	σ ($\times 10^{-6}$)
0.3 - 0.5	0.0	0.0	31 - 32	8.7	12.0	72 - 73	0.0	7.6
0.5 - 1.0	5.3	0.1	32 - 33	3.1	12.3	73 - 74	0.0	8.5
1.0 - 1.5	14.1	0.4	33 - 34	6.4	11.9	74 - 75	0.0	7.6
1.5 - 2.0	36.9	34.0	34 - 35	0.0	11.8	75 - 76	0.8	7.5
2.0 - 2.5	35.7	30.6	35 - 36	0.0	12.0	76 - 77	1.8	7.1
2.5 - 3.0	81.4	28.0	36 - 37	12.1	11.3	77 - 78	3.2	7.6
3.0 - 3.5	96.6	28.5	37 - 38	7.2	11.7	78 - 79	7.8	6.7
3.5 - 4.0	101.5	28.2	38 - 39	6.2	11.6	79 - 80	2.9	7.2
4.0 - 4.5	144.3	28.0	39 - 40	0.1	11.2	80 - 81	0.0	7.1
4.5 - 5.0	172.5	26.9	40 - 41	5.2	11.3	81 - 82	4.1	6.7
5.0 - 5.5	244.4	26.6	41 - 42	4.1	11.0	82 - 83	3.9	6.6
5.5 - 6.0	240.1	26.2	42 - 43	7.4	10.6	83 - 84	4.4	6.6
6.0 - 6.5	267.0	26.8	43 - 44	11.5	10.7	84 - 85	1.1	7.1
6.5 - 7.0	276.3	26.1	44 - 45	5.0	11.0	85 - 86	0.0	7.2
7.0 - 7.5	244.6	26.0	45 - 46	4.6	10.5	86 - 87	0.1	7.2
7.5 - 8.0	276.7	25.9	46 - 47	7.9	10.3	87 - 88	3.2	6.2
8.0 - 8.5	299.5	25.8	47 - 48	14.2	10.1	88 - 89	6.6	6.1
8.5 - 9.0	277.9	25.1	48 - 49	2.3	10.5	89 - 90	4.0	5.8
9.0 - 9.5	268.0	24.5	49 - 50	0.0	10.2	90 - 91	2.2	6.4
9.5 - 10.0	264.3	24.1	50 - 51	1.8	10.1	91 - 92	0.0	6.2
10 - 11	239.1	16.9	51 - 52	10.9	9.9	92 - 93	3.9	6.2
11 - 12	213.3	16.9	52 - 53	6.6	9.3	93 - 94	1.7	5.5
12 - 13	181.1	16.2	53 - 54	7.2	8.8	94 - 95	0.0	5.5
13 - 14	126.3	15.6	54 - 55	4.4	9.0	95 - 96	0.0	5.5
14 - 15	70.0	15.3	55 - 56	0.0	9.2	96 - 97	0.4	6.0
15 - 16	57.5	14.7	56 - 57	2.2	8.8	97 - 98	5.6	5.8
16 - 17	25.4	14.5	57 - 58	6.1	9.2	98 - 99	0.8	5.3
17 - 18	24.3	14.5	58 - 59	0.0	9.5	99 - 100	0.2	5.3
18 - 19	11.9	14.5	59 - 60	1.6	8.9	100 - 101	1.7	5.6
19 - 20	0.0	14.3	60 - 61	0.0	9.2	101 - 102	7.0	5.3
20 - 21	12.8	13.8	61 - 62	0.3	8.7	102 - 103	0.1	5.1
21 - 22	15.4	13.3	62 - 63	0.0	8.9	103 - 104	0.6	4.8
22 - 23	2.6	13.5	63 - 64	0.0	8.3	104 - 105	0.0	4.9
23 - 24	7.8	13.2	64 - 65	2.1	8.5	105 - 106	0.0	5.3
24 - 25	7.3	12.8	65 - 66	0.0	8.3	106 - 107	0.7	5.1
25 - 26	11.2	12.8	66 - 67	1.2	8.4	107 - 108	0.6	4.9
26 - 27	2.7	13.1	67 - 68	3.1	8.3	108 - 109	0.0	5.1
27 - 28	14.5	13.2	68 - 69	0.9	8.3	109 - 110	1.0	4.4
28 - 29	5.1	13.6	69 - 70	1.5	7.6	110 - 111	1.5	5.0
29 - 30	0.0	13.2	70 - 71	7.8	7.3	111 - 112	2.1	5.0
30 - 31	3.1	12.2	71 - 72	2.8	7.8	112 - 113	0.0	4.6

List of included articles

[I1] C. Lederer, the n_TOF Collaboration, *$^{197}Au(n,\gamma)$ cross section in the unresolved resonance region*, Phys. Rev. C 83 (2011) 034608.

[I2] C. Lederer, F. Käppeler, R. Nolte, M. Mosconi, M. Heil, R. Reifarth, S. Schmidt, I. Dillmann, U. Giesen, A. Mengoni, A. Wallner, *Definition of a standard neutron field with the $^{7}Li(p,n)^{7}Be$ reaction*, submitted to Phys. Rev. C (30 January 2012).

Further articles co-authored by C. Lederer

- E. Chiaveri and the n_TOF Collaboration, J. Kor. Phys. Soc. 59 (2011) 1620.
- N. Colonna, F. Belloni, E. Berthoumieux, M. Calviani, C. Domingo-Pardo, C. Guerrero, D. Karadimos, C. Lederer, C. Massimi, C. Paradela, R. Plag, J. Praena, R. Sarmento, Energy Environ. Sci. 3 (2010) 1910.
- N. Colonna, the n_TOF Collaboration, Nucl. Instr. Meth. B 24 (2011) 3251-3259.
- C. Domingo-Pardo, the n_TOF Collaboration, J. of Physics (Conference Series) 202 (2010) 012026.
- G. Giubrone, J.L. Tain, C. Lederer, the n_TOF Collaboration, J. Kor. Phys. Soc. 59 (2011) 2106.
- C. Guerrero, the n_TOF Collaboration, J. Kor. Phys. Soc. 59 (2011) 1624.
- F. Gunsing, the n_TOF Collaboration, AIP Conference Proceedings 1336 (2011) 547.
- C. Lederer, N. Colonna, I. Dillmann, C. Domingo-Pardo, U. Giesen, F. Gunsing, M. Heil, F. Käppeler, C. Massimi, A. Mengoni, M. Mosconi, R. Nolte, R. Reifarth, S. Schmidt, A. Wallner, J. of Physics (Conference Series) 337 (2012) 012045.
- C. Lederer, I. Dillmann, U. Giesen, F. Käppeler, A. Mengoni, M. Mosconi, R. Nolte and A. Wallner, Proceedings of the Final scientific EFNUDAT workshop, CERN, Geneva (2010).
- C. Lederer, the n_TOF Collaboration, PoS (NIC-XI) 048 (2010).
- C. Massimi, the n_TOF Collaboration, Phys. Rev. C 81 (2010) 0446161.
- C. Massimi, the n_TOF Collaboration, PoS (NIC-XI) 194 (2010).
- E. Mendoza, the n_TOF Collaboration, J. Kor. Phys. Soc. 59 (2011) 1813.

- R. Sarmento, the n_TOF Collaboration, Phys. Rev. C 84 (2011) 044618.
- D. Tarrio, the n_TOF Collaboration, Phys. Rev. C 83 (2011) 044620.
- A. Wallner, K. Buczak, T. Belgya, M. Bichler, L. Coquard, I. Dillmann, O. Forstner, R. Golser, F. Käppeler, C. Lederer, A. Mengoni, A. Priller, R. Reifarth, P. Steier, L. Szentmiklosi and W. Kutschera, J. of Physics (Conference Series) 202 (2010) 0120201.
- A. Wallner, Buczak, C. Lederer, H. Vonach, T. Fästermann, G. Korschinek, M. Poutivtsev, G. Rugel, A. Klix, K. Seidel, A. Plompen, V. Semkova, J. Kor. Phys. Soc. 59 (2011) 1378.
- A. Wallner, I. Dillmann, T. Fästermann, F. Käppeler, A. Klix, G. Korschinek, C. Lederer, G. Rugel, P. Steier, Proceedings of the workshop EFNUDAT Fast Neutrons - scientific workshop on neutron measurements, theory & applications, Geel, Belgium (2010).

References

[1] S. Merrill, Astrophys. J. 116 (1952) 21.

[2] E. Burbidge, G. Burbidge, W. Fowler, F. Hoyle, Rev. Mod. Phys. 29 (1957) 547.

[3] E. Anders, M. Grevesse, Geochim. Cosmochim. Acta 53 (1989) 197.

[4] K. Lodders, Astrophys. J. 591 (2003) 1220.

[5] C. Iliadis, Nuclear Physics of Stars, Wiley-VCH, Germany, 2007.

[6] C. E. Rolfs, W. S. Rodney, Cauldrons in the Cosmos, The University of Chicago Press, USA, 1988.

[7] M. Busso, R. Gallino, G. Wasserburg, Ann. Rev. Astron. Astrophys. 37 (1999) 239.

[8] F. Hoyle, Astrophys. J. Suppl. 1 (1954) 121.

[9] C. W. Cook, W. A. Fowler, C. C. Lauritsen, T. Lauritsen, Phys. Rev. 107 (1957) 508.

[10] F. Käppeler, A. Mengoni, Nuc. Phys. A 777 (2006) 291.

[11] D. D. Clayton, W. A. Fowler, T. Hull, B. Zimmermann, Ann. Phys. 12 (1961) 331.

[12] P. A. Seeger, W. Fowler, D. D. Clayton, Astrophys. J. Suppl. 11 (1965) 121.

[13] F. Käppeler, H. Beer, K. Wisshak, Rep. Prog. Phys. 52 (1989) 945.

[14] D. Clayton, M. Rassbach, Astrophys. J. 148 (1967) 69.

[15] F. Käppeler, Prog. Part. Nuc. Phys. 43 (1999) 419.

[16] S. E. Woosely, A. Heger, T. A. Weaver, Rev. Mod. Phys. 74 (2002) 1015.

[17] Z. Y. Bao, H. Beer, F. Käppeler, F. Voss, K. Wisshak, At. Data Nucl. Data Tab. 76 (2000) 70.

[18] S. E. Woosley, J. R. Wilson, G. J. Mathews, R. D. Hoffman, B. S. Meyer, Astrophys. J. 433 (1994) 229.

[19] K. Takahashi, J. Witti, H. T. Janka, Astron. Astrophys. 286 (1994) 857.

[20] F. Gunsing, Tech. Rep., CEA/Saclay, DSM/DAPNIA/SPhN, 2005.

[21] J. A. Harvey, Experimental Neutron Resonance Spectroscopy, Academic Press Inc., USA, 1970.

[22] F. H. Fröhner, Tech. Rep., Forschungszentrum Karlsruhe, Germany, 2000.

[23] E. P. Wigner, Proc. Gatlinbury Conf. Neutron Time-of-Flight Methods, Oak Ridge Natl. Lab. Rept., O.R.N.L. 2309, 1957.

[24] D. M. Brink, Ph.D. thesis, Oxford University, 1955.

[25] C. E. Porter, R. G. Thomas, Phys. Rev. 101 (1956) 483.

[26] A. M. Lane, R. G. Thomas, Rev. Mod. Phys. 30 (1958) 257.

[27] C. Angulo *et al.*, Nuc. Phys. A 656 (1999) 3.

[28] T. Rauscher, F. K. Thielemann, At. Data Nucl. Data Tab. 75 (2000) 1.

[29] K. Takahashi, K. Yokoi, At. Data Nucl. Data Tab. 36 (1987) 375.

[30] Neutron time of flight facility n_TOF, `www.cern.ch/ntof`.

[31] Los Alamos Neutron Science Center, `http://lansce.lanl.gov/`.

[32] GELINA neutron time of flight facility, `http://irmm.jrc.ec.europa.eu/about_IRMM/laboratories/Pages/gelina_neutron_time_of_flight_facility.aspx`.

[33] The Oak Ridge Electron Linear Accelerator Pulsed Neutron Source, `http://www.phy.ornl.gov/nuclear/orela/`.

[34] W. Ratynski, F. Käppeler, Phys. Rev. C 37 (1988) 595.

[35] F. Käppeler, A. Naqvi, M. Al-Ohali, Phys Rev. C 35 (1987) 936.

[36] M. Heil, S. Dababneh, A. Juseviciute, F. Käppeler, R. Plag, R. Reifarth, S. O'Brien, Phys Rev. C 71 (2005) 025803.

[37] U. Abbondanno, the n_TOF Collaboration, Technical report CERN-SL-2002-053 ECT, CERN and Geneva, 2003.

[38] F. Gunsing, the n_TOF Collaboration, Nuc. Instr. Meth. Phys. Res. B 361 (2007) 925.

[39] C. Guerrero, the n_TOF Collaboration, Nuc. Instr. Meth. Phys. Res. A 608 (2009) 424.

[40] R. Plag *et al.*, Nuc. Instr. Meth. Phys. Res. A 496 (2003) 425.

[41] J. Tain, the n_TOF Collaboration, CERN-INTC-2008-035, INTC-P-249, CERN, 2008.

[42] ^{6}Li$(n,\alpha)^{3}$H cross section, `http://www-nds.iaea.org/standards/`.

[43] ^{235}U(n,f) cross section, `http://www-nds.iaea.org/standards/`.

[44] C. Borcea *et al.*, Nuc. Instr. Meth. Phys. Res. A 513 (2003) 524.

[45] S. Andriamonje *et al.*, J. Kor. Phys. Soc. 59 (2010) 1597.

[46] C. Guerrero, private communication, 2011.

[47] J. Pancin, the n_TOF Collaboration, Nuc. Instr. Meth. Phys. Res. A 102 (2004) 524.

[48] D. Greiffenberg *et al.*, Nuc. Instr. Meth. Phys. Res. A 607 (2009) 38.

[49] C. Lederer, N. Colonna, Internal n_TOF note, 2009.

[50] F. Belloni, private communication, 2011.

[51] G. Lorusso, the n_TOF Collaboration, Nuc. Instr. Meth. Phys. Res. A 532 (2004) 454.

[52] N. Colonna, talk at the n_TOF annual meeting 2010, Seville, 2010.

[53] N. Larson, Updated users guide for SAMMY: Multi-level R-matrix fits to neutron data using Bayes equations, ORNL/TM-9179/R7, Oak-Ridge National Laboratory, 2003.

[54] R. Macklin, R. Gibbons, Phys. Rev. 159 (1967) 1007.

[55] J. Wilson *et al.*, Nuc. Instr. Meth. Phys. Res. A 511 (2003) 388.

[56] U. Abbondanno, the n_TOF Collaboration, Nuc. Instr. Meth. Phys. Res. A 521 (2004) 454.

[57] C. Massimi, A. Borella, S. Kopecky, C. Lampoudis, P. Schillebeeckx, M. Moxon, G. Vannini, J. Kor. Phys. Soc. 59 (2011) 1689.

[58] F. Fröhner, SESH computer code, Tech. Rep. GA-8380, Gulf General Atomic, 1968.

[59] A. Wallner, Nuc. Instr. Meth. Phys. Res. B 268 (2010) 1277.

[60] J. L. Tain, the n_TOF Collaboration, INTC/P-208, CERN, 2006.

[61] C. Sneden, A. McWilliam, G. Preston, J. Cowan, D. Burris, B. Armosky, Astrophys. J. 467 (1996) 819.

[62] C. Sneden, J. Cowan, I. Ivans, G. Fuller, S. Burles, T. Beers, J. Lawler, Astrophys. J. 533 (2000) L139.

[63] C. Sneden *et al.*, Astrophys. J. 591 (2003) 936.

[64] T. Rauscher, A. Heger, R. Hoffman, S. Woosley, Astrophys. J 576 (2002) 323.

[65] H. Nassar, M. Paul, I. Ahmad, D. Berkovits, M. Bettan, P. Collon, S. Dababneh, Phys. Rev. Letters 94 (2005) 092504.

[66] Z. Y. Bao, F. Käppeler, At. Data Nucl. Data Tables 36 (1987) 411.

[67] I. Dillmann, M. Heil, F. Käppeler, R. Plag, T. Rauscher, , F.-K. Thielemann, AIP Conf. Proc. 819 (2005) 123.

[68] I. Dillmann, R. Plag, F. Käppeler, T. Rauscher, Proceeding of the workshop "EFNUDAT Fast Neutrons - scientific workshop on neutron measurements, theory & applications" held on April 28-30 2009 at Geel, Belgium (2009) 55.

[69] H. Beer, R. R. Spencer, Nuclear Physics, Section A 240 (1975) 29.

[70] A. M. Alpizar-Vicente *et al.*, Phys. Rev. C 77 (2008) 015806.

[71] I. Dillmann *et al.*, Nuc. Instr. Meth. Phys. Res. B 268 (2010) 1283.

[72] A. Tomyo *et al.*, Astrophys. J. 623 (2005) L153.

[73] T. Rauscher, K. H. Guber, Phys Rev. C 66 (2002) 028802.

[74] T. Rauscher, K. H. Guber, Phys Rev. C 71 (2005) 059903(E).

[75] R. Colle, B. E. Zimmermann, Appl. Rad. and Iso. 47 (1996) 677.

[76] S. Walter, Ph.D. thesis, University of Karlsruhe, 2008.

[77] M. Pignatari *et al.*, Astrophys. J. 710 (2010) 1557.

[78] I. L. Barnes, S. B. Garfinkel, W. B. Mann, Appl. Rad. and Iso. 22 (1971) 777.

[79] H. Michael, A. Neubert, H. Nickel, Appl. Rad. and Iso. 25 (1974) 183.

[80] A. Harder, S. Michaelsen, A. Jungclaus, A. Williams, H. Borner, M. Trautmannsheimer, Zeits. f. Physik A 343 (1992) 7.

[81] C. Lederer, C. Massimi, V. Vlachoudis, INTC-P-283, CERN, 2010.

[82] A. Couture, private communication, 2010.

[83] G. F. Knoll, Radiation Detection and Measurement, John Wiley & Sons, USA, 2nd edition edn., 1989.

[84] L. Venturini, B. Pecequilo, Appl. Rad. and Iso. 48 (1997) 493.

[85] J. F. Briesmeister, MCNP - A General Monte Carlo N- Particle Transport Code, LA-13709-M, Los Alamos National Laboratory, 2000.

[86] N. Colonna, private communication, 2010.

[87] S. Agostinelli *et al.* (Geant4 Collaboration), Nuc. Instr. Meth. Phys. Res. A 506 (2003) 250.

[88] G. Giubrone, private communication, 2011.

[89] C. Massimi, private communication, 2011.

[90] C. Coceva, 'Neutron energy standards' in 'Nuclear data standards for nuclear measurements', vol. NEA-OECD Report, NEANDC-311'U', INDC (SEC)-101, 1992.

[91] A. Tsinganis, private communication, 2012.

[92] R. R. Spencer, private communication to EXFOR, 1973.

[93] H. P. Axmann, D. A. J. Endacott, J. E. Jolly, M. C. Moxon, Nickel Isotope Resonance Parameters, Progress Report 18, a.E.R.E. Harwell Reports, 1972.

[94] L. Litvinskiy *et al.*, Vop. At.Nauki i Tekhn.,Ser.Yadernye Konstanty 1990 (1990) 27.

[95] R. W. Hockenbury, Z. M. Bartolome, J. R. Tatarczuk, W. R. Moyer, R. C. Block, Phys. Rev. 178 (1969) 1746.

[96] M. Chadwick *et al.*, Nuc. Data Sheets 112 (2011) 28872996.

[97] K. Shibata *et al.*, J. Nucl. Sci. Technol. 48 (2011) 1.

[98] A. Koning, R. Forrest, M. Kellett, R. Mills, H. Henriksson, Y. Rugama, JEFF Report 21, OECD/NEA and Paris, 2006.

[99] G. Sims, D. Juhnke, J. of Inorg. Nuc. Chem. 32 (1970) 2839.

[100] H. Ishikawa, Nuc. Instr. Meth. Phys. Res. 109 (1973) 493.

[101] S. Mughabghab, Atlas of Neutron Resonances, Elsevier, 2006.

[102] J. Farrell, E. Bilpuch, H. Newson, Ann. Phys. 37 (1966) 367.

[103] Experimental Nuclear Reaction Data (EXFOR), http://www-nds.iaea.org/exfor/exfor.htm.

[104] J. Garg, J. Rainwater, W. Havens, Phys. Rev. C 3 (1971) 2447.

[105] N. Kievel, private communication, 2011.

[106] Frankfurt Neutron Source - FRANZ http://exp-astro.physik.uni-frankfurt.de/franz/.

[107] E. Chiaveri, the n_TOF Collaboration, CERN-INTC-2012-029, INTC-O-015, CERN, 2012.

[108] A. Carlson *et al.*, Nuc. Data Sheets 110 (2009) 3215.

[109] R. Macklin, J. Halperin, R. Winters, Phys. Rev. C 11 (1975) 1270.

[110] R. L. Macklin, Nuc. Sci. Eng 79 (1981) 265.

[111] F. Käppeler, R. Gallino, S. Bisterzo, W. Aoki, Rev. Mod. Phys. 83 (2011) 157.

[112] C. Massimi, C. Domingo-Pardo, the n_TOF Collaboration, Phys. Rev. C 81 (2010) 044616.

[113] G. Aerts, the n_TOF Collaboration, Phys. Rev. C 73 (2006) 054610.

[114] A. Borella *et al.*, Nuc. Sci. Eng. 152 (2006) 1.

[115] D. B. Syme, Nuc. Instr. Meth. Phys. Res. 198 (1982) 357.

[116] J. Apostolakis, CERN program library long writeup and W5013, Tech. Rep., CERN and GEANT library, 1993.

[117] A. Borella, G. Aerts, F. Gunsing, M. Moxon, P. Schillebeeckx, R. Wynants, Nuc. Instr. Meth. Phys. Res. A 577 (2007) 626.

[118] N. Yamamuro, M. Igashira, T. Sekiya, H. Shirayanagi, J. Nucl. Sci. Technol. 20 (1983) 797.

[119] J. Czirr, M. Stelts, Nuc. Sci. Eng. 52 (1973) 299.

[120] R. Gwin, E. Silver, R. Ingle, H. Weaver, Nuc. Sci. Eng. 59 (1976) 79.

[121] V. Kononov, B. Yurlov, V. Manturov, E. Poletaev, V. Timokhov, Yad. Fiz. 26 (1977) 947.

[122] S. Zhu, S. Jiang, Y. Chen, D. Luo, Chin. J. Nucl. Phys. 6 (1984) 23.

[123] L. Kazakov *et al.*, Technical report INDC(CCP)-248/G, Institute for Physics and Power Engineering and Oblozinsky, 1985.

[124] `http://www-nds.iaea.org/ndspub/endf/prepro/`.

[125] C. Lampoudis, S. Kopecky, C. Massimi, M. Moxon, P. Schillebeeckx, Standard CM, IAEA, Vienna, `http://www-nds.iaea.org/standards/CM2010/`, 2010.

[126] G. Feinberg *et al.*, submitted to Phys. Rev. C .

[127] R. Gallino *et al.*, Astrophys. J. 497 (1998) 388.

[128] C. Vockenhuber *et al.*, Phys. Rev. C 75 (2007) 015804.

[129] M. Heil, F. Käppeler, E. Uberseder, R. Gallino, M. Pignatari, Phys. Rev. C 77 (2008) 015808.

[130] V. Pronyaev, A. Mengoni, A. Carlson, International Neutron Cross-Section Standards: Measurements and Evaluation Techniques. Summary Report Consultant's Meeting 13-15 October 2008, Tech. Rep., IAEA Vienna, 2008.

[131] H. Beer, F. Käppeler, Phys. Rev. C 21 (1980) 534.

[132] S. Röttger *et al.*, AIP Conf. Proc. 1175 (2009) 375.

[133] H. Brede *et al.*, Nuc. Instr. Meth. Phys. Res. 169 (1980) 349.

[134] R. Reifarth, M. Heil, F. Käppeler, R. Plag, Nuc. Instr. Meth. Phys. Res. A 608 (2009) 139.

[135] S. Schmidt, Master's thesis, Goethe Universität Frankfurt, 2011.

[136] S. Badikov *et al.*, Tech. Rep., IAEA Vienna, 2007.

[137] P. Schillebeeckx, private communication, 2011.

[138] A. D. Carlson *et al*, J. Kor. Phys. Soc. 59 (2011) 1390.

[139] R. Reifarth *et al.*, Phys Rev. C 66 (2002) 064603.

[140] H. Muthig, Ph.D. thesis, Technical University of Munich, 1984.

[141] M. Trautmannsheimer, Ph.D. thesis, Technical University of Munich, 1992.

Acknowledgments

I would like to thank my supervisors Robin Golser and Anton Wallner for giving me the opportunity to do my PhD thesis at this institute. I am very grateful to Toni for his considerate supervision, despite of his relocation to Australia, and for giving me the freedom to work on different research topics of my interest.
Without a doubt Franz Käppeler was one of the most important persons during my PhD. I am deeply indebted to him for his invaluable support concerning data analysis, writing papers and proposals, scientific background and preparing talks.
I also want to thank Frank Gunsing, Nicola Colonna, Cristian Massimi and Alberto Mengoni for their help with analyzing the n_TOF data, providing important input to papers and always answering the many questions I had.
Furthermore, I am very grateful to Cesar Domingo-Pardo for helping with the Au analysis. The analysis program he provided was a great support for learning to use ROOT.
I am very grateful to the people at CERN: Eric Berthoumieux, Enrico Chiaveri, Carlos Guerrero, Andrea Tsinganis, Vasilis Vlachoudis and Christina Weiß for working so hard to keep n_TOF running smoothly. Special thanks to Carlos and Eric for explaining so much and helping with the data analysis.
Thanks to Giuseppe Giubrone and Jose Luis Tain for providing important information accelerating my work, and to Francesca Belloni, Pino Tagliente (aka Romeo) and Marco Calviani for helping with my first steps at n_TOF and with ROOT.
I am very grateful to Frank, Franz, Nicola, Phil, Robin and Toni for reading through my thesis and providing important suggestions.
Many thanks to Herbert Danninger and Christian Gierl for pressing the ^{62}Ni powder without any complications.
Thanks to Alfred, Helga, Jenny, Martin, Oliver, Peter, Robin, Toni and the workshop members Ewald, Gabi, Johann and Wolfgang for their help at various things.
I would like to thank the Austrian Science Fund, who provided financial support through the projects P20434 and I428. Thanks to the n_TOF Collaboration, the European Commission within the Sixth Framework Program through I3-EFNUDAT (EURATOM contract no. 036434) and the University of Vienna for covering part of my travel costs.
Thanks to all my colleagues at n_TOF who I had a great time with during shifts, meetings and exciting soccer table tournaments, also I would like to thank my office colleagues Martin, Karin, Jenny, Edith, Leonard, Oliver, Philipp and Stefan for their nice company.

Vielen Dank an den Vorstand der $\phi\alpha\kappa$ Barbara, Daniela, Fabienne, Gabi und Silvia und all meinen anderen Freunden. Danke meinen Mitbewohnern während all meiner

Jahre in Wien, besonders Jasmin, ohne deren Aufmerksamkeit ich heute nicht hier sein würde.
Ich bin meinen Eltern zutiefst dankbar, die mich während meiner gesamten Laufbahn immer unterstützt haben. Ich danke auch meinen Schwestern Nina und Eva-Maria, die immer für mich da waren.

Curriculum Vitae of Claudia Lederer

Present Affiliation:
VERA-laboratory
University of Vienna - Faculty of Physics
Währingerstrasse 17, 1090 Vienna

Permanent Address:
Liechtensteinstrasse 134
1090 Vienna
Austria

Personal

Date of birth:	7 May 1984
Place of birth:	Salzburg, Austria
Nationality:	Austria
Email:	claudia.lederer@univie.ac.at

Education

1990-1994:	Elementary school in Seekirchen am Wallersee, Austria
1994-2002:	High school, Christian-Doppler Gymnasium, Salzburg, Austria
21 June 2002:	Graduation (Matura *with distinction*)
2002-2006:	Bachelor study of Astronomy, University of Vienna
10 April 2006:	Bachelor degree in Astronomy (Bakk. rer. nat.) *with distinction*
2002-2008:	Diploma study in Physics, University of Vienna
2007-2008:	Master thesis at the VERA laboratory, Faculty of Physics, University of Vienna: *Cross section measurements of neutron induced production of ^{53}Mn and ^{55}Fe relevant for the fusion project ITER*
1 September 2008:	Master degree in Physics (Mag. rer. nat.) *with distinction*
2-6 June 2008:	Participation at the *Neutron Resonance Analysis Summer School* held at EC-JRC-IRMM in Geel, Belgium
since fall 2008:	Doctoral study at the VERA laboratory, Faculty of Physics, University of Vienna: *Neutron capture measurements on ^{62}Ni, ^{63}Ni and ^{197}Au and their relevance for stellar nucleosynthesis*
12-17 July 2010:	Participation at the *Wilhelm and Else Heraeus summer-school on Nuclear Astrophysics in the Cosmos* held at GSI Darmstadt and University of Heidelberg, Germany
18-27 September 2011:	Participation and presentation of a talk at *The Sixth European Summer School on on Experimental Nuclear Astrophysics* held at Santa Tecla, Italy

Working Experience

since autumn 2010:	Teaching Assistent at University of Vienna (*Nuclear Physics*)

Publications

2010

A. Wallner, I. Dillmann, T. Fästermann, F. Käppeler, A. Klix, G. Korschinek, C. Lederer, G. Rugel, P. Steier. *AMS measurement of long-lived radionuclides produced in fusion and fission environments*. Proceedings of the workshop EFNUDAT Fast Neutrons - scientific workshop on neutron measurements, theory & applications, April 28-30, 2009, Geel, Belgium, EUR Technical and Scientific Research series, Report EUR 23883 EN, Belgium, 171 (2010).[1]

A. Wallner, K. Buczak, T. Belgya, M. Bichler, L. Coquard, I. Dillmann, O. Forstner, R. Golser, F. Käppeler, W. Kutschera, C. Lederer, A. Mengoni, A. Priller, R. Reifarth, P. Steier, L. Szentmiklosi. *Precise measurement of the neutron capture reaction* $^{54}Fe(n,\gamma)^{55}Fe$ *via AMS*. Journal of Physics: Conference Series **202**, 012020-1 (2010).

N. Colonna, F. Belloni, E. Berthoumieux, M. Calviani, C. Domingo-Pardo, C. Guerrero, D. Karadimos, C. Lederer, C. Massimi, C. Paradela, R. Plag, J. Praena and R. Sarmento. *Advanced nuclear energy systems and the need of accurate nuclear data: the n_TOF project at CERN* . Energy Environ. Sci. **3**, 1910 (2010).

C. Lederer, I. Dillmann, U. Giesen, F. Käppeler, A. Mengoni, M. Mosconi, R. Nolte, A. Wallner, *Definition of a standard neutron field with the* $^{7}Li(p,n)^{7}Be$ *reaction*, Proceedings of the Final scientific EFNUDAT workshop, CERN, Geneva.[1]

C. Lederer, and the n_TOF collaboration. *New measurement of the astrophysically important reaction* $^{62}Ni(n,\gamma)$ *at n_TOF*. PoS (NIC-XI) 048 (2010).

2011

C. Lederer, and the n_TOF collaboration. $^{197}Au(n,\gamma)$ *cross section in the unresolved resonance region*. Physical Review C**83**, 034608 (2011).

A. Wallner, K. Buczak, C. Lederer, H. Vonach, T. Faestermann, G. Korschinek, M. Poutivtsev, G. Rugel, A. Klix, K. Seidel, A. Plompen and V. Semkova . *Production of Long-lived Radionuclides* ^{10}Be, ^{14}C, ^{53}Mn, ^{55}Fe, ^{59}Ni *and* ^{202g}Pb *in a Fusion Environment*, Journal of the Korean Physical Society, **59**, 1378 (2011).

G. Giubrone, JL. Tain, C. Lederer, and the n_TOF collaboration. *The Role of Fe and Ni for s-process Nucleosynthesis and Innovative Nuclear Technologies*, Journal of the Korean Physical Society, **59**, 2106 (2011).

2012

C. Lederer, N. Colonna, I. Dillmann, C. Domingo-Pardo, U. Giesen, F. Gunsing, M. Heil, F. Käppeler, C. Massimi, A. Mengoni, M. Mosconi, R. Nolte, R. Reifarth, S. Schmidt, A. Wallner, and the n_TOF collaboration. $^{197}Au(n,\gamma)$ *- towards a new standard for energies relevant to stellar nucleosynthesis*. Journal of Physics: Conference Series **337**, 012045 (2012).

[1] not peer-reviewed

further n_TOF papers

C. Massimi, C. Domingo-Pardo, G. Vannini, and the n_TOF collaboration. *^{197}Au(n,γ) cross section in the resonance region*. Physical Review C**81**, 044616-1 (2010).

C. Domingo-Pardo, and the n_TOF collaboration. *Forthcoming (n,γ) measurements on the Fe and Ni isotopes at CERN n_TOF*. Journal of Physics: Conference Series **202**, 012026 (2010).

C. Massimi, and the n_TOF collaboration. *Measurement of the $^{24,25,26}Mg(n,\gamma)$ reaction cross-section at n_TOF*. PoS (NIC XI) 194 (2010).

D. Tarrio, and the n_TOF collaboration. *Neutron-induced fission cross section of ^{nat}Pb and ^{209}Bi from threshold to 1 GeV: An improved parametrization*. Physical Review C**83**, 044620 (2011).

F. Gunsing, and the n_TOF collaboration. *The Neutron Time-Of-Flight Facility n_TOF at CERN: Phase II*, AIP Conference Proceedings **1336**, 547 (2011).

E. Mendoza, and the n_TOF collaboration. *Improved Neutron Capture Cross Section Measurements with the n_TOF Total Absorption Calorimeter*, Journal of the Korean Physical Society, **59**, 1813 (2011).

E. Chiaveri, and the n_TOF collaboration. *Past, Present and Future of the n_TOF Facility at CERN*, Journal of the Korean Physical Society, **59**, 1620 (2011).

C. Guerrero, and the n_TOF collaboration. *Characterization of the New n_TOF Neutron Beam: Fluence, Profile and Resolution*, Journal of the Korean Physical Society, **59**, 1624 (2011).

R. Sarmento, and the n_TOF collaboration. *Measurement of the $^{236}U(n,f)$ cross section from 170 meV to 2 MeV at the CERN n_TOF facility*. Physical Review C**84**, 044618 (2011).

N. Colonna, and the n_TOF collaboration. *Neutron measurements for advanced nuclear systems: The n_TOF project at CERN*. Nucl. Instr. Meth. B **24**, 3251-3257 (2011).

submitted

C. Lederer, F. Käppeler, R. Nolte, M. Mosconi, M. Heil, R. Reifarth, S. Schmidt, I. Dillmann, U. Giesen, A. Mengoni and A. Wallner. *Definition of a standard neutron field with the $^{7}Li(p,n)^{7}Be$ reaction*. submitted to Phys. Rev. C (2012).

Invited talks

CEA-Saclay, Gif-sur-Yvette, France, 17 June 2011: *Nuclear astrophysics measurements at n_TOF at CERN.*

Conference contributions

Joint Annual ÖPG-SPG-ÖGAA Meeting, 6-10 September 2009, Innsbruck, Austria:
Production of ^{53}Mn in a nuclear fusion environment presented as talk.
Study of nuclear reactions relevant for the astrophysical s-process with n_TOF at CERN. presented as poster.

DPG spring meeting, 8-12 March 2010 Hannover, Germany:
^{53}Mn - a long-lived activation product in a nuclear fusion environment. presented as talk.

11th symposium on Nuclei in the Cosmos, Heidelberg, 19-23 July 2010, Germany:
New measurement of the astrophysically important reaction ^{62}Ni(n,γ) at n_TOF. presented as talk.
Definition of a standard neutron field with the ^{7}Li(p,n)^{7}Be reaction. presented as poster.

Annual ÖPG Meeting, 6-9 September 2010, Salzburg, Austria:
New measurement of the ^{62}Ni(n,γ) cross-section with n_TOF at CERN relevant for the astrophysical s-process. presented as talk.

Final Scientific EFNUDAT workshop, 30 August - 2 September 2010, CERN, Geneva, Switzerland:
Definition of a standard neutron field with the ^{7}Li(p,n)^{7}Be reaction. presented as talk.

Nuclear Physics in Astrophysics V, 2 - 8 April 2011, Eilat, Israel:
^{197}Au(n, γ) - towards a new standard for energies relevant to stellar nucleosynthesis. presented as talk.

2nd workshop on Exotic Radionuclides from Accelerator Waste for Science and Technology, 29 August - 2 September 2011, Paul Scherrer Institute, Villigen, Switzerland:
Measurement of the ^{62,63}Ni(n, γ) cross section at n_TOF/CERN. presented as talk.